THE DESIGN AND DEVELOPMENT OF A GEOSTATIONARY SYNTHETIC THINNED APERTURE RADIOMETER

by

Boon Hwang Lim

A dissertation submitted in partial fulfillment
of the requirements for the degree of
Doctor of Philosophy
(Electrical Engineering and Atmospheric, Oceanic and Space Science)
in The University of Michigan
2009

Doctoral Committee:

Professor Christopher S. Ruf, Chair
Professor Anthony W. England
Professor William R. Kuhn
Assistant Research Scientist Roger Dean De Roo
Professor Francisco Torres, Polytechnic University of Catalonia

For my parents
Who for reasons unbeknownst to me
Love me unconditionally

Acknowledgements

First and foremost, I am eternally indebted to my parents – a teacher and an engineer – who instilled within me at a very early age a desire for learning and problem solving. My accomplishments are a direct result of your faith and support all these years, especially while I toiled far away from home.

Second, my sincere gratitude to my academic mentors, of which there have been many. My advisor, Dr. Christopher Ruf, directed my graduate research ensuring that I emerged from the process well-rounded, capable of contributing on both the engineering and scientific levels. The members of my thesis committee, Drs. Tony England, Bill Kuhn, Roger De Roo and Francesc Torres, provided invaluable advice on my research and the thesis itself. Dr. Brian Gilchrist, who first planted the seed that I personally could further the boundaries of science, and lastly Dr. Alan Tanner, who rewrote my definition of engineering and research excellence. These are the giants whose shoulders I have stood upon. I will treasure all the tools and notions that each of you have imparted to me.

Third, I have been blessed to be part of several groups during my tenure at the University. The Electrical Engineering and Computer Science Department provided the foundation which I built upon at The Department of Atmospheric, Oceanic and Space Sciences. Professionally, the Space Physics Research Laboratory afforded me first hand experience in designing and building instruments. The Microwave Geophysics Group and the Remote Sensing Group provided me with the opportunity to work on a variety of

projects that opened my eyes to the field of remote sensing. Working with other outstanding institutions (Jet Propulsion Laboratory, Goddard Space Flight Center, Naval Research Laboratories, Marshall Space Flight Center and the University of Central Florida) exposed me to the dynamic and collaborative nature of the research.

Finally, the years at the University have been punctuated by the coming and going of friends, each graduation season marking the end of an era – I have said more than my fair share of goodbyes. However, friendship is truly what makes life worth living, and my friends I thank you all for that we have shared and hope the future gives us the opportunity to make more lasting memories.

This work was supported in part by NASA Headquarters under the NASA Earth and Space Science Fellowship Program – Grant NNG05GP47H.

Table of Contents

List of Figures

List of Tables

Abstract

The Precipitation and All-Weather Temperature and Humidity (PATH) mission outlined in the National Research Council decadal survey for launch in 2016-2020 recommends a microwave array spectrometer as the instrument payload. A design for the Geostationary Synthetic Thinned Aperture Radiometer (GeoSTAR) is presented that fulfils all but one of the mission requirements – integration time – and options are available to meet this requirement. A technological roadmap exists for the development of the key hardware components to minimize size and power requirements, especially with respect to the receiver and digital correlator design.

The fabrication of the instrument demonstrator, GeoSTAR-D, contributed significantly to the hardware development (receivers, antennas, correlators) and provided a test-bed to verify the theoretical understanding of a two-dimensional Synthetic Thinned Aperture Radiometry (STAR). Measurements in the anechoic chamber provided a boresight phase calibration and verified that the antenna patterns closely matched the theoretical model. Field deployment of the instrument with an engineered Earth disk target allowed for generation of GEO like measurements and calibration validation. A theoretical based image retrieval algorithm was implemented and combined with various models to account for the sky aliases and minimize the target discontinuities. Images generated after sky alias removal and Gibbs mitigation had residual errors of less than 2%.

A high resolution Earth disk model is generated from existing publically available datasets, appropriate geophysical parameter models and a full radiative transfer model. The model allows for the generation of un-physically realizable scenes to determine the impact of individual geophysical parameters on the observed brightness temperature. The realistic brightness temperature images are then evaluated with a GeoSTAR-like instrument simulator to investigate the effectiveness of apodization, spatial frequency information content and various processing algorithms. At the temperature sounding channels, sufficient contrast is available even at the largest baselines. The recommended retrieval algorithm performs well even when based on imperfect input models.

CHAPTER 1

MICROWAVE RADIOMETRY FROM GEOSTATIONARY ORBIT

1.1 INTRODUCTION

The advantages of microwave radiometry from space borne platforms are well known and numerous. Microwave remote sensing allows us to observe and quantify key environmental and climatological parameters such as soil moisture [1], sea surface salinity [2], ocean wind speed [3] and direction [4, 5], to name a few. The primary benefit is that measurements can be performed over areas where in-situ measurements are simply not possible or cost effective. Two issues affecting the usability of these measurements are the spatial and temporal resolution.

Spatial resolution dictates the pixel size of the image that scientists will be able to interpret, each pixel representing a cell of independent information. These pixels represent aggregate conditions present in a particular area and are only valuable if we are able to discern changes in the desired parameter. Finer resolution is required for localized phenomena, such as precipitation.

Temporal resolution is essentially the refresh rate of the individual pixels, or the image as a whole. A single low Earth orbiting (LEO) satellite typically has a revisit time of several days and differs according to the exact orbit. In-situ measurements refresh rates vary widely - weather stations provide almost instantaneous data (seconds to minutes) - whereas atmospheric profilers such as radiosondes are nominally available

only every 12 hours. To monitor dynamically developing weather phenomena, a rapid revisit time is required.

The relationship between resolution and the relevant meteorological features that can be observed is summarized in Table 1.1.

Table 1.1: Temporal and Spatial Scales of Meteorological Features [6]

Temporal Scale [h]	Spatial Scale [km]	Atmospheric Phenomenon
0-0.1	0.1-1	Tornadoes
0.1-1	1-5	Thunderstorms
6-12	10-50	Fronts, Squall Lines
12-24	10-100	Hurricanes
24-48	200-500	Synoptic cyclones
>24	1000-10000	Planetary waves, atmospheric tides, mean zonal temperature

The National Oceanic and Atmospheric Administration (NOAA) operate two types of satellite systems – the Polar-orbiting Operational Environmental Satellite (POES) and the Geostationary Operational Environment Satellite (GOES) – named for the type of orbit each satellite occupies. GOES orbits at an altitude of 35,786 km, known as the Geostationary Earth Orbit (GEO), compared to 700-800 km for POES, and are unique as they orbit at the same rotational rate as the Earth. The GEO allows for continuous observation of almost an entire hemisphere of the Earth disk.

POES platforms are equipped with both infrared (IR) and passive microwave (MW) sensors, the latter which allow for vertical soundings of temperature and humidity even in cloudy conditions. The refresh rate of the data is on the order of many hours even for a pair of satellites, which does not sufficiently capture the evolution of precipitation events. Additional satellites do improve the refresh rate, however it is to be noted that the individual measurements swaths still have to be stitched together to form a

composite dataset with inherent temporal displacement. Figure 1.1 shows an image generated from a single swath of the Advanced Microwave Sounding Unit (AMSU).

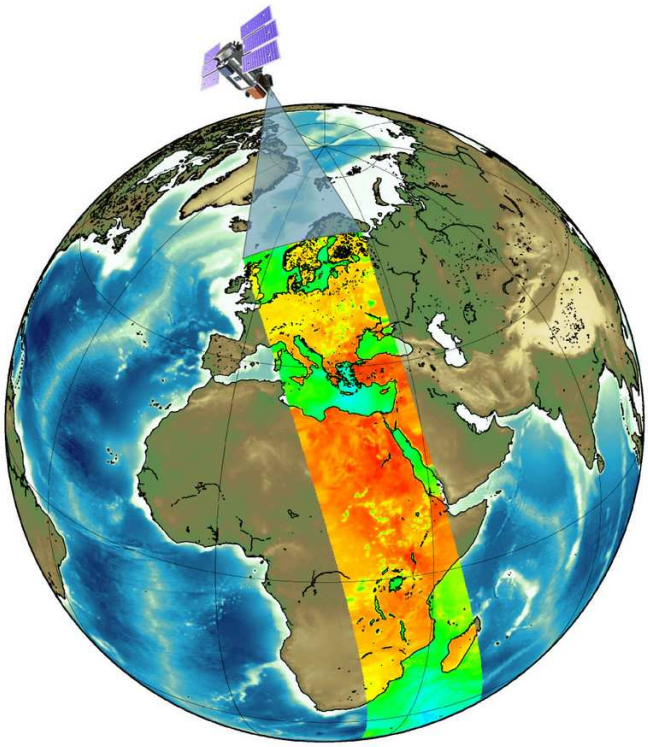

Figure 1.1: Composite Image of AMSU Orbit Swath Generation
Courtesy of the Satellite Atmospheric Science Group
At the Luleå Technical University, http://www.sat.ltu.se/

Introduced in 1994, GOES (I-M spacecraft) platforms are equipped with sensors in the IR wavelengths for soundings [7]. Without a MW sensor, GOES soundings are only available in cloud free areas and in the upper troposphere above cloud tops, resulting in gaps in the data fields. The addition of a MW instrument would improve the temporal resolution by filling in these gaps and have significant impact on numerical weather prediction (NWP) models. To that extent, a platform that could monitor global temperature profiles and precipitation with POES spatial scales and GOES type field of view and rapid refresh rates is ideal. The inclusion of a MW sensor on a GOES platform is supported by many in the community, demonstrated by the letter of support published

in the National Weather Digest in December 2005 [8]. The instrument also tops NOAA's list of "pre-planned product improvements" (P^3I) as listed in the GOES-R program requirements document [9]. The benefits from the development and eventual deployment of the instrument are evident to both the community and the administration.

In 2007, the National Research Council (NRC) released the decadal survey regarding Earth science and applications from space [10]. The Precipitation and All-Weather Temperature and Humidity (PATH) mission is recommended for launch in the 2016-2020 time frame. Figure 1.2 summarizes the measurements made and the utility to the scientific community.

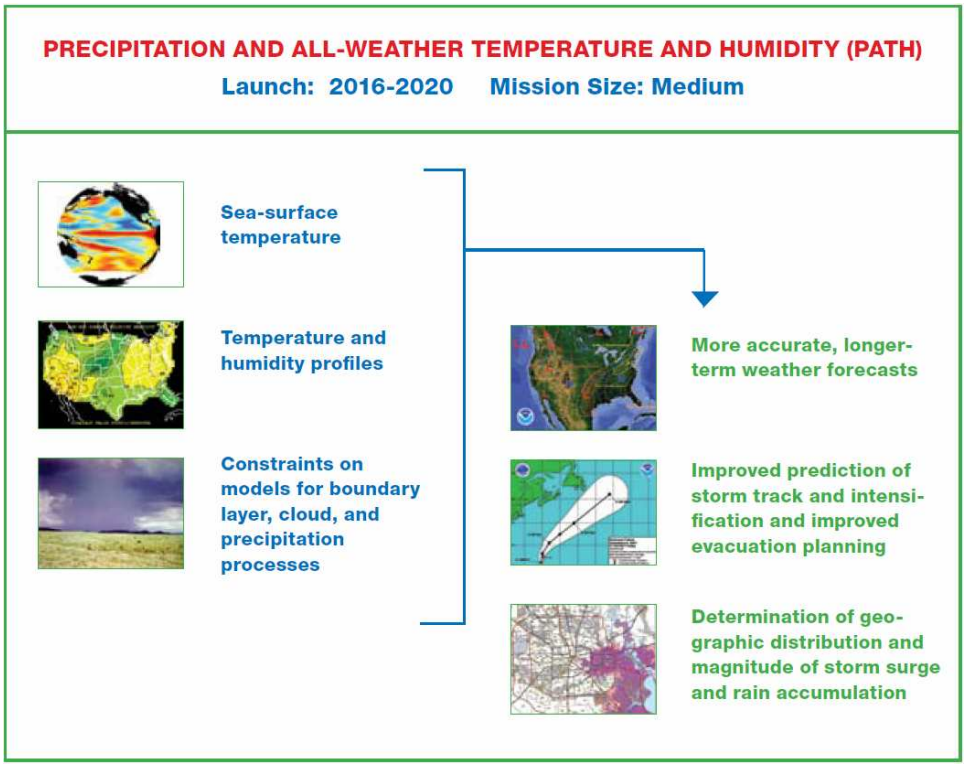

Figure 1.2: PATH Mission Measurements and Implications [10]

The lack of a MW sensor on GOES platforms has been primarily due to technological barriers associated with the antenna and the momentum compensation. Due to the orbit altitude, 5 times larger than POES, mounting an antenna of sufficient

size and weight to provide the desired spatial resolution is challenging, even with today's technology. Two distinct solutions to the problem have been proposed for next generation GOES platforms - a scanning real aperture [11] and an interferometric synthetic aperture [12]. In the specifications generated by the NRC for the PATH mission, the instrument technology recommended is a microwave array spectrometer.

The development of the geosynchronous interferometric synthetic aperture radiometer is the subject of this thesis. The more technologically mature real aperture solution is only discussed briefly in section 1.5. The following sections (1.2 – 1.4) trace the signal path from generation to theory of measurement as it would pertain to the real aperture solution.

1.2 THERMAL EMISSION

Radiometric measurements are passive measurements that rely solely on the inherent thermal radiation and absorption of the constituents to be measured. All objects that have a kinetic temperature larger then absolute zero (0 K) vibrate or spin at the microwave frequencies, which generate electromagnetic radiation that is referred to as thermal emission. The spectrum of the thermal emission depends on the molecular and atomic structure of the constituent. A useful concept for the following discussions is that of a black body – defined as a hypothetical material that absorbs all incident radiation while reflecting none.

The spectrum and magnitude of emission of a theoretical black body is described by Planck's Law [13]

$$B_f = \frac{2hf^3}{c^2}\left(\frac{1}{e^{hf/kT}-1}\right) \tag{1.1}$$

Where

B_f	=	Black body Spectral Brightness [W m^{-2} sr^{-1} Hz^{-1}]
h	=	Planck's constant (= 6.63×10^{-34}) [J s]
f	=	Frequency [Hz]
k	=	Boltzmann's constant (= 1.38×10^{-23}) [J K^{-1}]
T	=	Absolute temperature [K]
c	=	Speed of light (= 3×10^{8}) [m s^{-1}]

The radiation from an ideal black body at a given frequency (or wavelength) is only dependent on its temperature.

Figure 1.3 shows the black body spectral brightness plotted in logarithmic scales for two temperatures of interest - 300 K, approximately room temperature and 6000 K, approximately the temperature of the sun. These curves are unique and do not overlap.

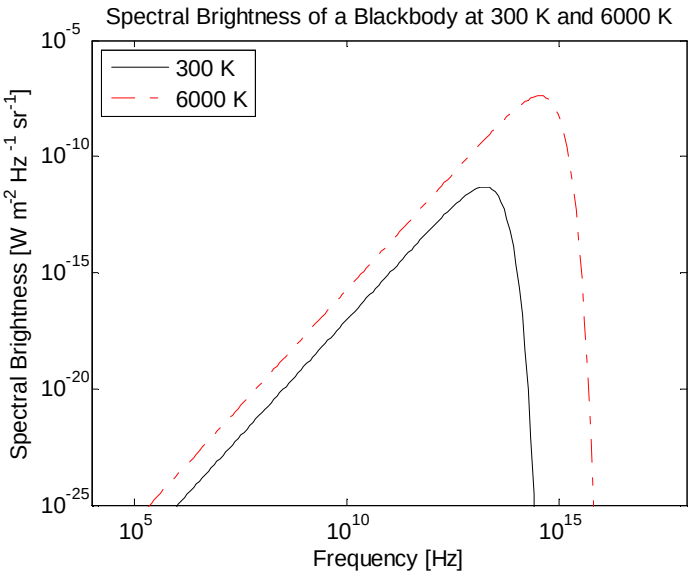

Figure 1.3: Spectral Brightness of a Blackbody at 300 K and 6000 K

The Rayleigh-Jeans Law, an approximation valid when $hf/kT << 1$, is used to simplify (1.1). Two expressions are given – the spectral brightness in terms of the frequency or the wavelength

$$B_f = \frac{2f^2k}{c^2}T, \quad B_\lambda = \frac{2ck}{\lambda^5}T \tag{1.2}$$

It can be seen that when the Rayleigh-Jeans Law is valid, the spectral brightness at a particular frequency or wavelength, is linearly dependent on temperature. At 300 K, the Rayleigh-Jeans approximation is valid up to 117 GHz with less than 1% error. Even at 300 GHz, the deviation from Planck's Law is only 3% [14]. The expression in (1.2) is total radiation for a completely unpolarized source. If measurements are made in either the vertical or horizontal polarization, the magnitude is halved

$$B_{f,P} = \frac{f^2 k}{c^2} T, \quad B_{\lambda,P} = \frac{ck}{\lambda^5} T \tag{1.3}$$

where the subscript P indicates a polarized measurement.

Suppose we are to measure this emission using an antenna. The nominal case is that of an antenna placed in a black body enclosure held at a known temperature [14, 15]. The total measured power is no longer a function of the antenna pattern. Instead, (1.3) reduces to the following simplified expression

$$P = kT\Delta f \tag{1.4}$$

Where
- P = Power [W]
- Δf = Bandwidth [Hz]

(1.4) is only dependent on the physical temperature and bandwidth measured.

This is analogous to the relationship between the thermal noise power and temperature of a resistor placed in the same enclosure at equilibrium, as measured by Johnson [16] and derived by Nyquist [17]. Equation (1.4), which gives a direct linear relationship between the radiated power and the temperature of an object, is the basis of microwave radiometric measurements.

Hence, if we are able to measure the radiation emitted from an object, we can gain insight into its temperature. However, most objects in the real world do not approximate

black bodies, and tend to reflect and scatter radiation in addition to partially absorbing it, as opposed to an ideal black body that only absorbs. The blackbody equivalent radiometric temperature, defined as the temperature of the object if it emitted radiation as an ideal black body, is often referred to as the brightness temperature (T_B) and is related to the physical temperature by a quantity called emissivity, ε

$$T_B = \varepsilon T \tag{1.5}$$

Emissivity is valued between 0 and 1, as T_B can be at a maximum the physical temperature. Microwave radiometers are calibrated to report the quantity T_B.

1.3 MICROWAVE RADIOMETERS

Natural emission is often very small in magnitude and specialized equipment is required to detect the signal. A radiometer is an instrument capable of performing these measurements. Most are familiar with the operation of the ubiquitous radio, a device that is able to receive broadcast radio waves and convert the signal into music. A radiometer performs a similar function, receiving instead the emission from natural objects and converting the signal into a T_B that scientists can interpret. Figure 1.4 shows the basic components of a radiometer system. After the signal has been captured by the antenna, amplifiers are required as the signal levels to be measured are very small. It is very common for there to be more than two amplification stages as shown. The filters select the particular frequency range to be measured, dependent on the geophysical parameter that is to be investigated.

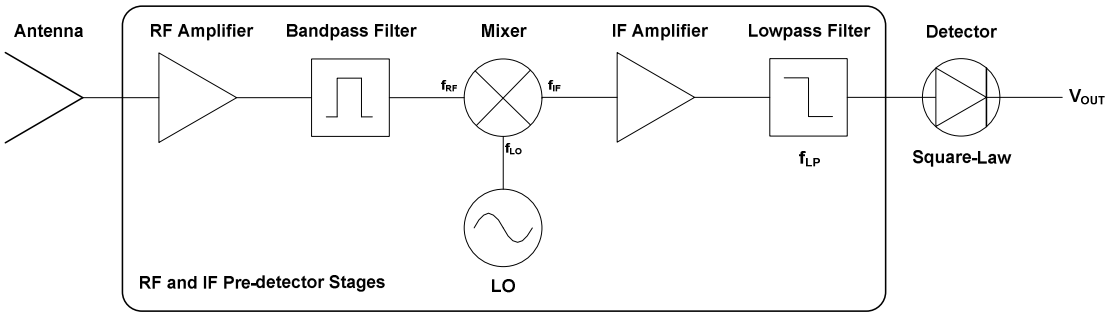

Figure 1.4: Typical Total Power Radiometer System

The system shown uses a square law detector that converts the output from the pre-detector stages into a voltage that is a measure of the power received. From (1.4), we know that the output power level is proportional to the temperature, which leads to the following expression

$$V_{OUT} \propto T_{sys}, \quad T_{sys} = T_A + T_R \tag{1.6}$$

Where

V_{OUT}	=	Output of the detector [V]
T_{sys}	=	System Brightness Temperature [K]
T_A	=	Antenna Brightness Temperature [K]
T_R	=	Receiver Brightness Temperature [K]

The total system brightness temperature (T_{sys}) is composed of contributions from the measurement system (T_R) and the antenna (T_A).

The sensitivity of the total power radiometer is obtained when we equate the noise in the detector measurement to the equivalent change in signal power [18, 19]. Radiometer sensitivity is also known as the noise equivalent delta temperature (NEΔT) and can be calculated using

$$\Delta T = \frac{T_{sys}}{\sqrt{\tau \Delta f}} = \frac{T_A + T_R}{\sqrt{\tau \Delta f}} \tag{1.7}$$

Where

ΔT	=	NEΔT [K]
τ	=	Integration Time [s]
Δf	=	Pre-detector Bandwidth [Hz]

This relationship has been shown to be valid for linear detectors if the deflection levels are small [19]. This essentially gives us a signal to noise ratio (SNR) of 1, though often a higher SNR is used to unambiguously resolve a signal. This parameter is one of the key performance indicators of a radiometer.

Equation (1.7) is introduced as a building block for further discussion. This relationship does not hold for an interferometric radiometer. A discussion of the sensitivity for interferometers and its impact on synthesized images can be found in Chapter 2.

1.4 RADIOMETRIC ATMOSPHERIC SOUNDINGS

Radiometric measurements rely on the inherent thermal radiation of the constituent to be measured as explained previously. In reality, the emission measured is also a function of the abundance or concentration of the constituent. Ideally, the response of the constituent would be orders of magnitude higher than that of the other components in the measurement pixel so that it may be easily resolved. In practice, this is rarely the case and solving simultaneously for multiple constituents is often necessary. Selecting the proper frequency of observation is integral to the success of the instrument. The following outlines the rationale for atmospheric soundings.

The relationship between absorption and emissivity is known as Kirchhoff's Law of Thermal Radiation and states that at thermal equilibrium, the emissivity of a body equals its absorptivity. Within the microwave region, absorption (and consequently emission) in the atmosphere can be broadly categorized as primarily due to two different constituents – gaseous oxygen and gaseous/liquid water.

Due to the well mixed nature of gaseous oxygen, whose fractional concentration is independent of altitude in the lower and middle atmosphere, it is possible to indirectly measure the atmospheric temperature from the response due to oxygen. For water vapor and liquid measurements, the vertical structure and concentration varies significantly, so generally only integrated quantities can be accurately retrieved. Figure 1.5 shows the variation in total atmospheric attenuation with frequency for a U.S. standard atmosphere [14] due to oxygen only compared to that with both oxygen and water vapor. From this, measurements of atmospheric temperature can be made at the lower wing of the 60 GHz oxygen line and water vapor at 183 GHz. Note that the 118 GHz oxygen line might also be used. However the response at 60 GHz is larger and so is better able to sense the emission at very high altitudes where the oxygen concentration is lowest.

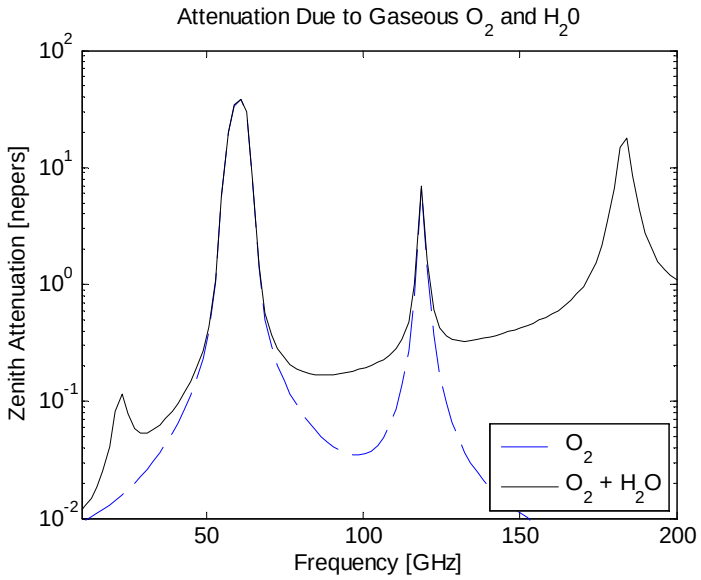

Figure 1.5: Atmospheric Attenuation Due to Gaseous Oxygen and Water Vapor

Current low earth orbiting satellite instruments that perform 60 and 183 GHz profiler measurements are the Advanced Microwave Sounding Unit (AMSU) [20] and Special Sensor Microwave/Temperature (SSM-T) [21]. The existing retrieval algorithms

provide excellent heritage and can be used as a starting point for the GOES versions reducing the development work required.

A major difference between measurements with GOES and POES is the extent of Earth incidence angles (EIAs) that are measured. The EIA is defined as the angle from vertical at the Earth surface location to the satellite and the extent is the maximum EIA. Typical satellite radiometers do not perform measurements beyond a 60^0 EIA, where the atmospheric path is approximately twice that of nadir. For example, both AMSU and SSMT are cross-track scanners with a maximum EIA of 57.6^0 and 49.5^0 respectively. A GOES sounder will measure all incidence angles from 0^0 to 90^0 at the Earth limb. In general, a larger EIA increases the peak height of the temperature weighting function and also its width [22].

The usability of the large incident angle measurements must be determined as it has significant impact on the instrument design. The impact on the instrument design will be discussed in Chapter 2 and an evaluation of the retrieval performance at large EIA will be given in Chapter 4.

1.5 SCANNING REAL APERTURE DESIGN

An instrument capable of performing measurements from GEO is the Geosynchronous Microwave (GEM) Sounder [11]. Utilizing a traditional real aperture antenna, the size requirements were reduced by simply using combinations of higher frequencies (shorter wavelengths) that have similar radiometric characteristics (e.g. utilizing the 118 or 424 GHz oxygen absorption lines as opposed to the 60 GHz one).

In order to generate an image, the antenna is physically scanned across the earth disc. Simulations of the performance of a GEM-type instrument have been performed [23]. Currently, the baseline instrument utilizes a micro scanned filled aperture antenna which minimizes the momentum impact by using a small rapidly tilting/translating subreflector in a Cassegrain configuration. Details about the current design options for the instrument are available [24]. Figure 1.6 shows a possible configuration of the instrument mounted on a GOES platform. Key components have been annotated.

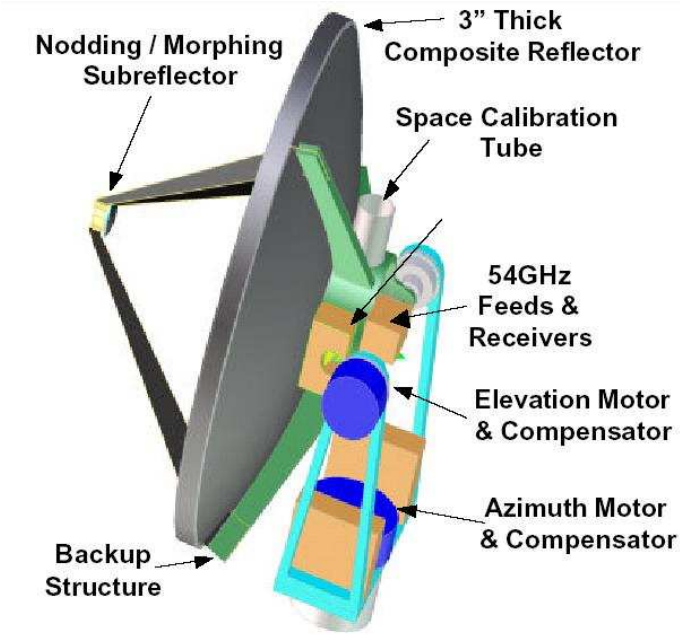

Figure 1.6: Annotated Mechanical Drawing of the Proposed GEM Sounder [25]

The major advantages of a real aperture type sounder - the instrument simplicity, lower cost and heritage - make it particularly attractive for selection at present. The major drawbacks to the system are: 1) the use of non-standard sub-millimeter emission lines rather than the traditional 60 and 183 GHz lines used in LEO, with less well understood performance; and 2) the impact of the mechanical scanning on the spacecraft itself, the other spacecraft instruments, mechanical reliability and the instrument lifetime.

1.6 INTERFEROMETRIC SYNTHETIC APERTURE HERITAGE

An alternative to the filled aperture, interferometric arrays have been utilized in radio-astronomy for several decades [15, 26]. From the early Michelson interferometer to current instruments such as the Very Large Array (VLA) in New Mexico, the technology is ever maturing and evolving [27, 28]. The use of Synthetic Thinned Aperture Radiometry (STAR) specifically for earth science was first proposed by Ruf *et al.* [29] at the University of Massachusetts Amherst (UMASS) and implemented in the form of the Electronically Scanned Thinned Array Radiometer (ESTAR) [30]. This L-Band five element one-dimensional (1-D) push-broom instrument demonstrated the promise of this type of imager at 1.4 GHz [31], and provided the first calibrated images performed by a STAR.

Figure 1.7 shows the original ESTAR configuration with the eight elemental 'spacings', derived from the five elements, called out explicitly.

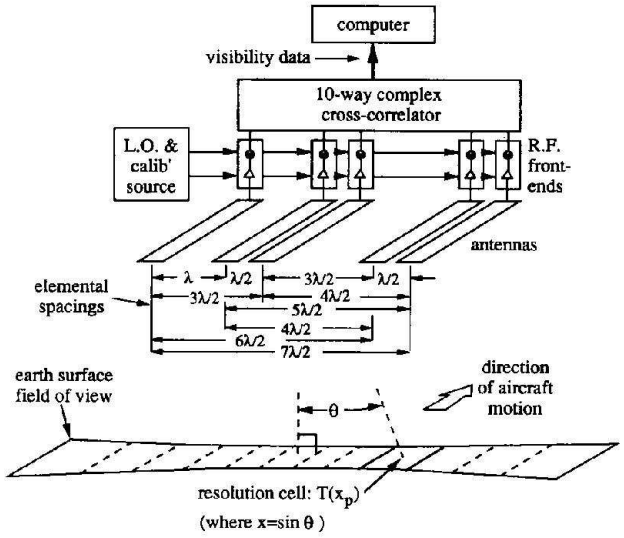

Figure 1.7: Original ESTAR Block Diagram [32]

Since then, other 1-D airborne instruments have followed suit including the Lightweight Rainfall Radiometer (LRR) [33] and the proposed Hurricane Imaging Radiometer (HIRAD) [34] currently under development. Figure 1.8 shows an image generated from LRR over the northern coast of California. The inset shows a video camera image that has been approximately co-located spatially. Clouds can be seen in the image towards the south. The MW imager allows for imaging through these clouds as clearly demonstrated. Both of these instruments are push-broom imagers taking advantage of the flight path of the aircraft to generate the image. This differs from cross-track scanning radiometers as all the pixels in a single image swath are generated simultaneously.

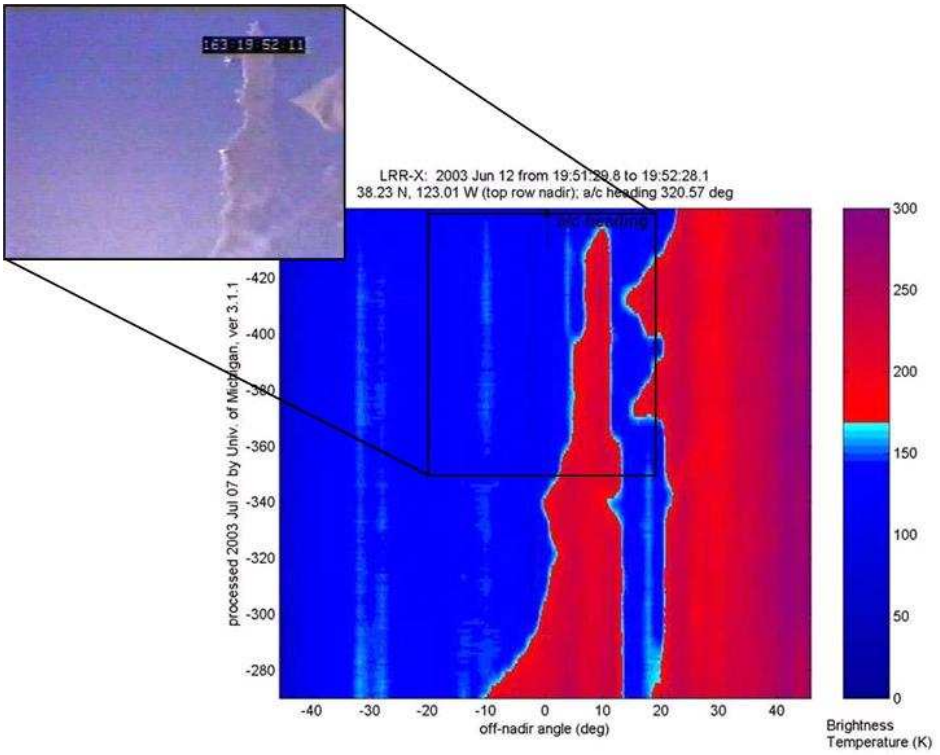

Figure 1.8: LRR Brightness Image with Overlay from Video Camera Image
Note that the Brightness Image is Available Even in the Presence of Clouds

The European Space Agency's (ESA) planned launch of the Soil Moisture and Ocean Salinity (SMOS) mission in early 2009 will be the first polarimetric two-dimensional (2-D) STAR radiometer in space. The primary instrument on the satellite will be the Microwave Imaging Radiometer with Aperture Synthesis (MIRAS). The development of the instrument has contributed greatly to the understanding of the technology [35], particularly in the areas of calibration and image synthesis. In addition, two different 2-D airborne instruments were developed to aid in the instrument design and calibration strategies: the Helsinki University of Technology Synthetic Aperture Radiometer (HUT-2D) [36] and the Polytechnic University of Catalonia's (UPC) Airborne MIRAS (AMIRAS) demonstrator [37].

Figure 1.9 is a rendition of the fully deployed satellite in orbit. SMOS will have 69 antenna elements and a 35 km spatial resolution at the center of the field of view. The arms pictured are approximately 4.5 m in length fully deployed.

Figure 1.9: SMOS Antenna Array Deployed in Orbit [38]

The growing confidence in the technology and methods of Synthetic Thinned Aperture Radiometry is evident.

1.7 GEOSTATIONARY SYNTHETIC THINNED APERTURE RADIOMETER

A candidate design for an interferometric synthetic aperture instrument that provides the required resolution and noise stability for soundings from GOES is the Geostationary Synthetic Thinned Aperture Radiometer (GeoSTAR) [39]. GeoSTAR will operate in two different frequency bands: 50 GHz and 180 GHz for temperature soundings and precipitation measurements, respectively. These frequencies are on the wings of the oxygen and water vapor bands. The STAR configuration allows for resolution at nadir on the order of 50 km at 50 GHz and 25 km at 180 GHz. To achieve the required resolution, the array requires a significant number of receiver elements. At 50 GHz, approximately 100 receiver elements per arm are required for a total of 300 receiver elements. For the 180 GHz array, double the number of elements is required for a total of 600 receiver elements.

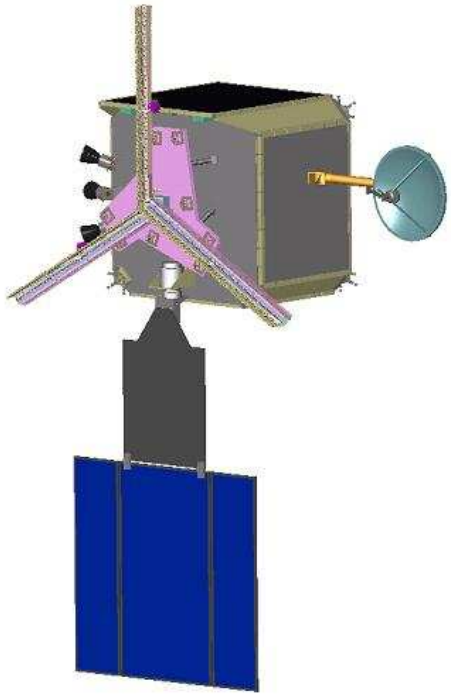

Figure 1.10: Rendition of an Early GeoSTAR Configuration as Integrated with the GOES Platform Courtesy of Ball Aerospace

Figure 1.10 shows an early configuration concept for GeoSTAR on a GOES spacecraft. The antenna configuration and layout are currently undergoing tradeoff analyses [40]. In particular, accommodation of the central elements is being investigated with particular emphasis on extra redundancy for the elements that measure the largest magnitude signals at the shortest inter-element spacings.

With the large number of antenna elements, the number of correlations required increases significantly. For both arrays, more than 200,000 correlations need to be calculated. Power and mass requirements cannot presently be met with the current technology. Given the pace of development, a roadmap exists for these requirements to be met for integration on future GOES platforms. Chapter 2 outlines the specifics of the GeoSTAR design and the theoretical basis for several of the design parameters.

To assess other issues, notably calibration and image synthesis, a demonstrator system was funded under the NASA Instrument Incubator Program (IIP). The reduced scope laboratory instrument has provided very promising initial results [41] and shepherds the technology through its risk reduction paces. Chapter 3 and 4 discuss some of the experiments performed with the demonstrator system and the results as they pertain to instrument performance, retrieval methods and atmospheric soundings.

1.8 THESIS STRUCTURE

The theoretical background of interferometric radiometry is discussed in Chapter 2 as an aid to understanding of the design trade spaces available to meet the requirements of GeoSTAR. The development of the demonstrator instrument will be discussed in detail, as well as the initial contributions made during development.

The calibration methodology and first measurements made with the instrument in an anechoic chamber are presented in Chapter 3. Traditional calibration with two known loads is discussed and a comparison between results of measurements made using the correlators and the totalizers is presented. The results from the chamber measurements indicate that the errors observed can be related closely to the physical pointing errors and are within the proposed error budget.

Chapter 4 presents the results of a full system test of GOES like imaging using the demonstrator. An Earth disk shaped calibration target is placed in the near-field of the instrument and the imaging capabilities are verified. Differential imaging techniques are evaluated and the instrument stability is determined.

A high resolution full disk Earth model has been developed and is described in Chapter 5. The model provides the first accurate representation of the high spatial frequency magnitudes to be expected from GEO images in the microwave spectrum. The model utilizes existing high quality datasets and geophysical models in concert with a radiative transfer model to determine the true angular distribution of the top of atmosphere brightness temperatures expected for the 50 GHz channels.

Chapter 6 outlines a reduced instrument simulator that is generated to evaluate the images generated by the full disk model. In addition to the inherent information content available to be measured, the instrument simulator is also used to evaluate different retrieval methods, especially those that mitigate the known effects of the Gibbs phenomena.

Chapter 7 summarizes the contributions of my work and makes suggestions for future research topics.

CHAPTER 2

GEOSTAR INSTRUMENT DESIGN AND DEVELOPMENT

2.1 INTERFEROMETRIC RADIOMETRY THEORY

A basic spatial interferometer system consists of two receivers that view the same scene through two antennas. The signals received by these two different receiving systems are cross-correlated to produce the visibility function, a measure of a spatial Fourier component of the brightness image given the particular physical spacing between antennas, or baseline. Figure 2.1 shows the typical configuration of a two element array as configured for space-borne application as proposed by Ruf *et al.* [29].

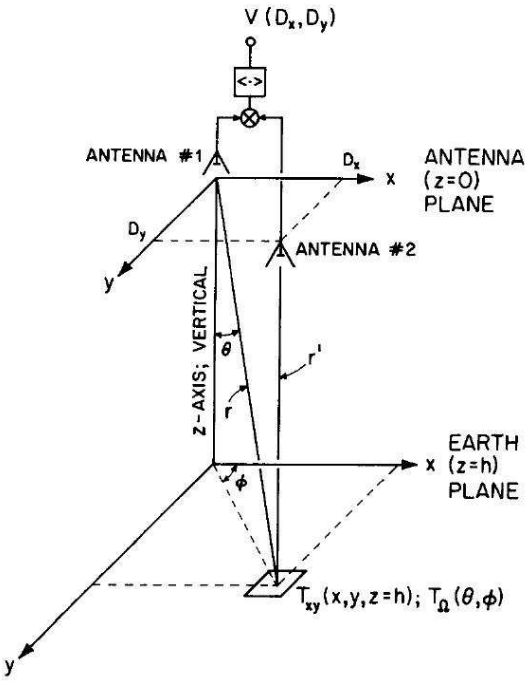

Figure 2.1: Two-Dimensional Earth Viewing Interferometer [29]

A single pair of antennas will produce only a single baseline, the current example having physical spacing (D_x,D_y). Multiple baseline measurements are required before the visibilities can be transformed back into the original scene. Baseline measurements are in the antenna plane, where z = 0. The angles defined in Figure 2.1 are borrowed from the spherical coordinate system, where θ is the polar or 'zenith' angle (though in this case we are downward looking) and ϕ is the azimuthal angle.

2.1.1 FROM BRIGHTNESS TEMPERATURES TO VISIBILITIES

The relationship between the T_B image and the Visibility function is explicitly defined by [42]

$$V_{ij}^{pq}(u_{ij},v_{ij}) = \iint_{\xi^2+\eta^2\le 1} \frac{T_B(\xi,\eta) - T_P\delta^{pq}}{\sqrt{\Omega_i\Omega_j}\sqrt{1-\xi^2-\eta^2}} . F_{ni}^{p}(\xi,\eta)F_{nj}^{q*}(\xi,\eta).\tilde{r}_{ij}(-\frac{u_{ij}\xi + v_{ij}\eta}{f_0}).e^{-j2\pi(u_{ij}\xi+v_{ij}\eta)}d\xi d\eta \quad (2.1)$$

Where

(u_{ij},v_{ij})	=	Spatial Frequency $\left(\frac{x_j - x_i}{\lambda},\frac{y_j - y_i}{\lambda}\right)$
(ξ,η)	=	Directional Cosines $(\sin\theta\cos\phi,\sin\theta\sin\phi)$
$T_B(\xi,\eta)$	=	Scene Brightness Temperature [K]
T_P	=	Receiver Physical Temperature [K]
δ^{pq}	=	$\delta^{pq}=1$ when p=q, else $\delta^{pq}=0$
Ω	=	Antenna Solid Angle [sr]
$F_n(\xi,\eta)$	=	Normalized Antenna Co-polar Voltage Patterns
f_0	=	Center Frequency [Hz]
$r_{ij}(-\frac{u_{ij}\xi + v_{ij}\eta}{f_0})$	=	Fringe Wash Function
i, j	=	integer valued indices for each of the two receivers being correlated

Equation (2.1) is only valid for the cross-correlation terms, i.e. where $i \neq j$. The formulation differs from those in the past due to the inclusion of the effects of receiver correlation as found by Corbella *et al.* [28]. The resulting visibility is a function of the

receiver pair used and the polarization of the receivers, denoted by the superscripts *p* and *q*.

The full expression (2.1) can be reduced significantly by making several reasonable assumptions. If we assume that the antennas are identical in performance, and that the spatial de-correlation effects are negligible ($\tilde{r}_{ij} \approx 1$) equation (2.1) reduces to

$$V_{ij}(u_{ij}, v_{ij}) = \iint_{\xi^2+\eta^2 \le 1} \frac{T_B(\xi,\eta) - T_P}{\Omega\sqrt{1-\xi^2-\eta^2}} . \left|F_n(\xi,\eta)\right|^2 . e^{-j2\pi(u_{ij}\xi + v_{ij}\eta)} d\xi d\eta \qquad (2.2)$$

It is convenient here to introduce the concept of the modified brightness temperature (T_{MB}) as defined by [43]

$$T_{MB}(\xi,\eta) = \frac{T_B(\xi,\eta) - T_P}{\Omega\sqrt{1-\xi^2-\eta^2}} . \left|F_n(\xi,\eta)\right|^2 \qquad (2.3)$$

By substituting (2.3) into (1.3) we arrive at a more familiar form of the visibility

$$V_{ij}(u_{ij}, v_{ij}) = \iint_{\xi^2+\eta^2 \le 1} T_{MB}(\xi,\eta) . e^{-j2\pi(u_{ij}\xi + v_{ij}\eta)} d\xi d\eta \qquad (2.4)$$

It is evident in (2.4) that visibility is related to the brightness temperature map by the Fourier transform (and vice versa), a form similar to that originally derived by Bracewell and Roberts [44], though performed by them in one dimension.

2.1.2 ANTENNA ARRAY CONFIGURATION

In order to sample the visibility domain, many different physical spacings between antennas are required. Early instruments used a single pair of antennas and mechanically moved them in order to sample the visibility domain. This method, though time consuming, is still practiced during the development of instruments, to verify the measurement concept and subsystem performance. A more practical configuration is to have an array of antennas that provide the different physical spacings simultaneously.

For the one dimensional (1-D) case, the distribution of the antenna elements allows for significant 'thinning' of the array – where a smaller number of antenna elements can be used to generate a significantly larger number of unique baselines [45, 46].

Figure 2.2 shows an optimal configuration for 5 antenna elements. If we define the smallest wavelength spacing between any antenna elements as d_λ, then the maximum distance between any two antenna elements is $9\,d_\lambda$. In this optimal configuration, all the spacings from 1 to 9 are available pairing different antennas. The array has been 'thinned' from 10 elements to 5, while still being capable of measuring all the baselines up to 9. In addition, a redundant measurement of the 3 d_λ baseline can also be made.

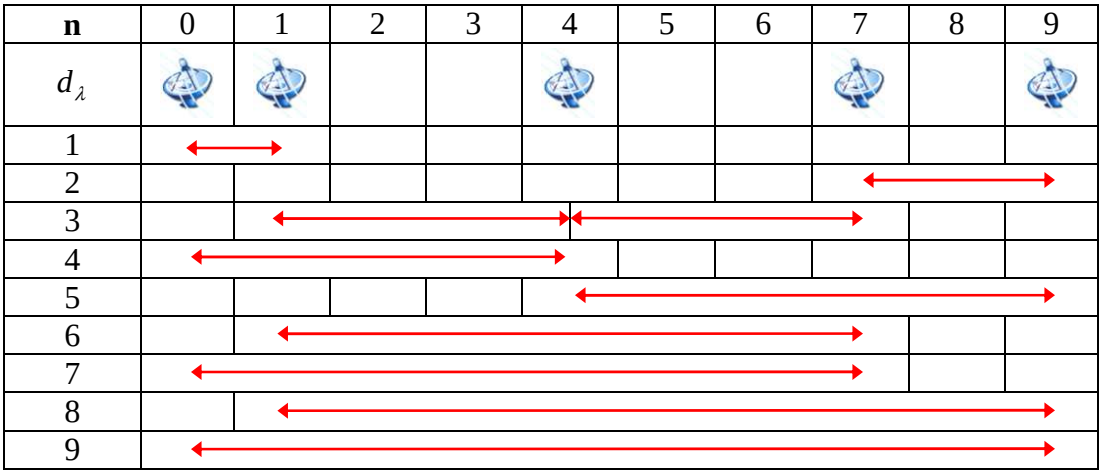

Figure 2.2: Optimal Configuration for a 1-D 5 Element Antenna Array

Various configurations have been recommended for two-dimensional (2-D) aperture arrays. With the introduction of the second dimension, the sampling in the visibility domain is also characterized by a sampling scheme, most commonly either rectangular or hexagonal. Borrowing from the terminology of radio astronomy, the physical shape of the array is often named after the geometric shape or the character of the alphabet that is similar to the array when viewed from above in a planar fashion. For

rectangular sampling in the visibility domain, three configurations are common, the cross ('+'), the 'T' and the 'U' [27]. For hexagonal sampling, the 'Y' and the triangle arrays are popular.

The hexagonal sampling scheme has a distinct advantage compared to the rectangular in that it achieves the same spatial resolution with fewer elements. When phased array elements are arranged in a triangular pattern (where the hexagonal shape is inherent), Sharp [47] found that the number of elements required was 13.4% less than the rectangular case assuming a circular band-limited waveform. A simple way of visualizing this concept in the visibility domain is shown in Figure 2.3 where the axes represent the spatial frequency in terms of wavelength.

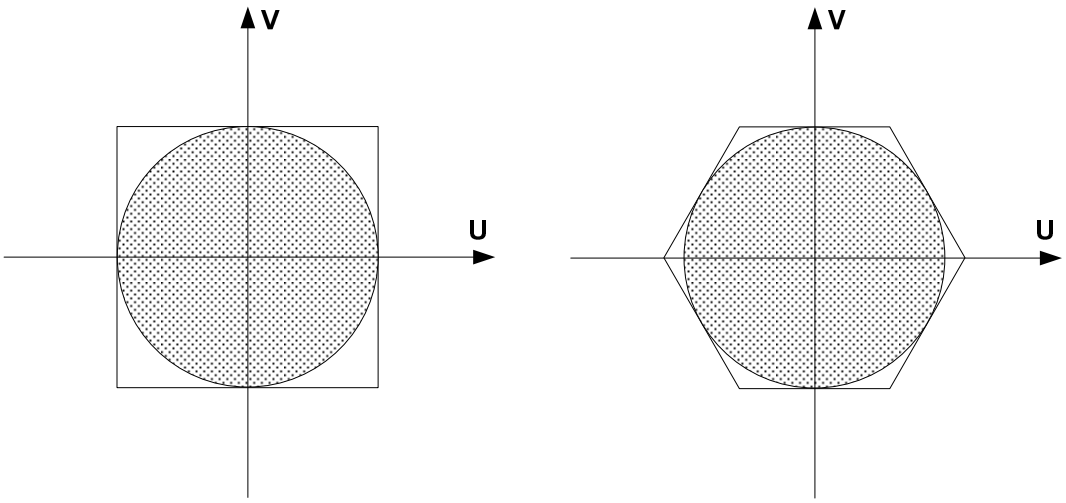

Figure 2.3: A Circular Band Region Embedded in a Square (left) and a Hexagon (right) [48]

Comparing the two images, the area required to encompass the circle is more efficiently performed by the hexagon (right), resulting in less wastage in the corners of the square (left). This efficient scheme is apparent in nature in the honeycombs of bees. The area required by a hexagon to encompass a circle of equivalent radius is 0.866 that of a square resulting in the 13.4% savings.

The other difference between the sampling schemes is in the generation of redundant visibility samples. Rectangular schemes tend to generate more redundant visibilities given the same number of elements. While redundant visibilities are especially important at the center of the domain (low frequency content contains the majority of image power), redundancies at the larger baselines are often unused. As some baseline redundancies are valuable, this cannot be construed as a wholly negative aspect of the rectangular scheme.

A hexagonal scheme is favored in most applications primarily due to the more efficient sampling in the visibility domain. In a traditional 'Y' array, the array is defined by a single number, the number of elements (N_{EL}) a single arm contains excluding the central element. The total number of antenna elements within a 'Y' array is given by

$$N_T = 3N_{EL} + 1 \tag{2.5}$$

Where

N_T = Total Number Antenna Elements [#]
N_{EL} = Number of Elements in an Arm [#]

where the '+1' represents the central element. The number of complex visibilities (N_C) that can be measured is a function of the combination of pairs of antennas between and within the three arms, as given by

$$N_C = 3N_{EL}^2 + 3N_{EL} \tag{2.6}$$

Where

N_V = Total Number of Unique Complex Visibilities [#]
N_{EL} = Number of Elements in an Arm [#]

The Fourier transform of real signals are known to be Hermitian, which means that each visibility has a conjugate in the other half-space, i.e. $V(-u,-v) = V^*(u,v)$. With this relationship, and adding in the power (self-correlation or DC), measurement we arrive at the final expression for total number of visibilities (N)

$$N = 2\left(3N_{EL}^2 + 3N_{EL}\right) + 1 \tag{2.7}$$

This number represents the total number of complex samples in the visibility domain (including the Hermitian conjugates) or the total number of real and imaginary visibility components measured, inclusive of the DC component [43].

The number of elements in the arms directly relates to the number of visibilities measured and the coverage in the visibility domain. From Figure 2.3, increasing the number of elements increases the area covered by the hexagon, and the maximum radius of the circle that may be inscribed.

2.1.3 IMAGE PIXEL RESOLUTION

The extent of coverage in the visibility domain is directly related to the pixel resolution. The distance from the origin defines the maximum spatial frequency measured which is related to the maximum physical spacing of the antennas. For a 1-D linear array, the relationship can be found approximately using the array factor and finding the angular extent between the nulls [29]. Define d_λ explicitly to be the smallest distance between any two elements in units of wavelength $\left(d_\lambda = D/\lambda\right)$ and $d_{\lambda,\max}$ as the maximum spacing in units of wavelength. For typical arrays, where it is optimum to have the elements spaced in units of d_λ (see Figure 2.2), it is common to express $d_{\lambda,\max} = nd_\lambda$, where n is the largest integer separation. In the example shown in Figure 2.2, $n = 9$. The resolution of the linear array is then approximated by the following relationship

$$\Delta\theta \approx 2\sin^{-1}\left(\frac{1}{2d_{\lambda,\max}+d_{\lambda}}\right) = 2\sin^{-1}\left(\frac{1}{(2n+1)d_{\lambda}}\right) \tag{2.8}$$

Where

$\Delta\theta$ = Angular Resolution [rad]

For n >> 10, (2.8) can be simplified to

$$\Delta\theta \approx \frac{1}{d_{\lambda,\max}} = \frac{1}{nd_{\lambda}} \tag{2.9}$$

The derivation for the 2-D case is similar and the result for the rectangular array is well approximated by (2.9) if the sampling is regular and the largest separation is equal in both dimensions of the array. For the hexagonally sampled case, it is necessary to account for the differences in the geometry to the sampling. Bara *et al.* [49] investigated this and found a similar expression that could be used based only on the maximum separation in the spatial frequency domain [50]

$$\Delta\theta_{Hex} \approx \frac{\pi/2}{\Delta U_{\max}} = \frac{\pi/2}{2\sqrt{3}N_{EL}d_{\lambda}} = \frac{\pi}{4\sqrt{3}}\left(\frac{1}{d_{\lambda,arm}}\right) \tag{2.10}$$

Where

$\Delta\theta_{Hex}$ = Hexagonal Sampling Angular Resolution [rad]

$\Delta U_{\max}$ = Maximum Distance Between Spatial Frequency Points in Wavelengths

$d_{\lambda,arm}$ = $N_{EL}d_{\lambda}$

This expression was established by numerical simulation for SMOS, and not derived analytically. Note that in this case, the largest separation is defined in terms of a Y-array arm length, $d_{\lambda,arm}$. Figure 2.4 shows the relationship between the maximum spatial frequency sampling distance and that determined by sampling only within a single arm. $\Delta U_{\max}$ is $4\cos 30^0 = 2\sqrt{3}$ larger than the sampling within a single arm, $N_{EL}d_{\lambda}$.

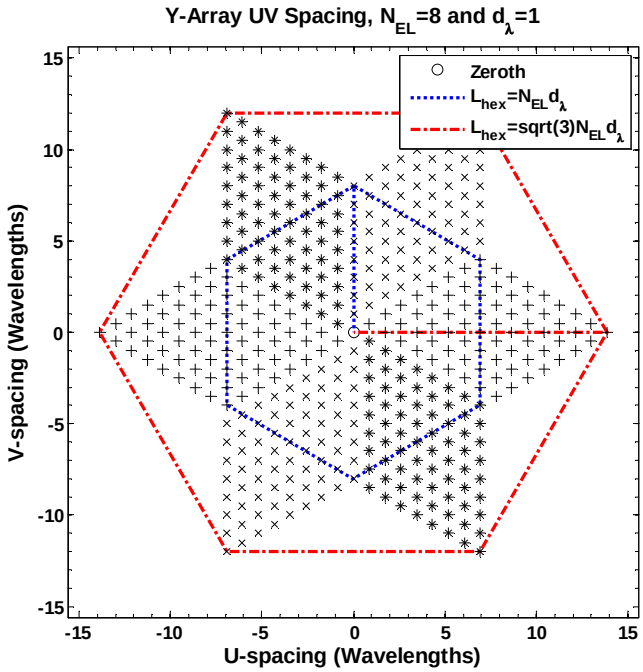

Figure 2.4: Spatial Frequency Sampling Area as Defined by a Regular Hexagon and the Associated Hexagon Side Lengths

2.1.4 FIELD OF VIEW

A note of nomenclature: the field of view (FOV) here is defined as the reconstructed image field of view from nadir. In a traditional total power radiometer with a very narrow beam antenna pattern, the FOV is effectively defined by the maximum physical scanning angle of the antenna, with each measurement representing a different pixel in the image. This differs significantly in a synthetic aperture radiometer. The antenna array performs the measurements in the visibility domain, effectively sampling the spatial frequency components instantaneously in the half-space viewed by the array (the +z direction in Figure 2.1). When sampling in the visibility domain, much like in the time domain, there is a sampling criterion that must be met to prevent aliasing.

The Nyquist-Shannon Sampling Theorem [51, 52] states that the sampling rate must be twice the highest frequency component to be measured. With spatial frequencies, the visibility sampling rate determines the highest spatial frequency that can

be recovered. Failure to achieve the sampling criterion will result in aliasing in the visibilities – where the measurements become functions of many sources and unresolvable. To satisfy Nyquist, the visibilities must be sampled every $\lambda/2$, which results in $d_\lambda = 1/2$.

If the wavelength spacing between the antennas is larger than $\lambda/2$, aliasing occurs in the form of a second antenna main beam that appears in the fringes [53]. For radio astronomy application, the FOV is approximated by

$$\theta_{FOV} = \sin^{-1}\left(\frac{1}{2d_\lambda}\right) \tag{2.11}$$

Where

θ_{FOV} = Maximum Off-Nadir Field of View [rad]

which gives the maximum angular extent between the main beam and the fringe [15].

This extent is applicable when the source extent is limited, and the background T_Bs are known, small and constant. However, in the case of an extended source, aliases are significant and difficult to remove at the edges of the FOV. The unambiguous field of view (UFOV) is defined as the region within which there are is no aliasing present. The limits of this region can be calculated using the following

$$\theta_{UFOV} = \sin^{-1}\left(\frac{1}{d_\lambda} - 1\right), \text{ for } 0.5 \le d_\lambda \le 1 \tag{2.12}$$

Where

θ_{UFOV} = Off-Nadir Unambiguous Field of View Extent [rad]

and (2.12) is valid to $d_\lambda = 1$. Past this limit, aliases are always present in the reconstructed image. The difference between (2.11) and (2.12) is best illustrated by Figure 1.4, where the impact of the aliases and the limit of each image can be easily seen in the one dimensional case.

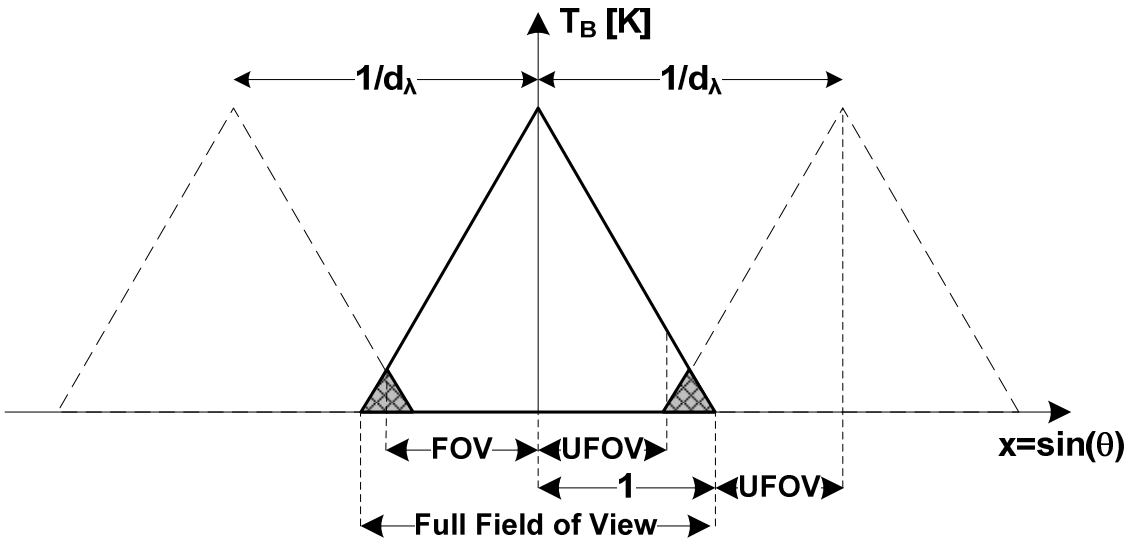

Figure 2.5: Diagram Illustrating the Difference Between the Radio Astronomy FOV and the UFOV

For the hexagonal sampling case, aliases occur periodically every $\frac{2}{\sqrt{3}}\frac{1}{d_\lambda}$ along three axes separated by 120^0 [41, 43] in the image domain (represented in direction cosines). For the UFOV, where there are no aliases in the image, the maximum spacing is given by

$$d_{\lambda,UFOV\ Max} = \frac{2}{\sqrt{3}} \tag{2.13}$$

Note that for the hexagonal sampling, the Nyquist limit is $1/\sqrt{3} = 0.58$ and not 0.5. Past this limit, there is no UFOV and aliases are present during any measurement, similar to the 1-D formulation. Figure 2.6 shows the aliases generated in the image domain given various minimum antenna spacing, d_λ. The edges of the aliased images are represented by the dashed circles. In the direction cosine coordinates, a unit circle at the origin represents the full half space FOV. Figure 2.6a shows the Nyquist case where within the unit circle there are no aliases present. Figure 2.6b, where $d_\lambda = 0.89$ (the SMOS antenna

spacing), is between Nyquist and the limit for the UFOV given by (2.13). The UFOV is shown as the hexagonal region in the center surrounded by the dashed lines. Figure 2.6c represents the limit of the UFOV where sampling in the unit circle will have no aliases. Figure 2.6d shows that past the UFOV limit, the alias centers appear within the unit circle. The different regions will have aliases based on the overlap.

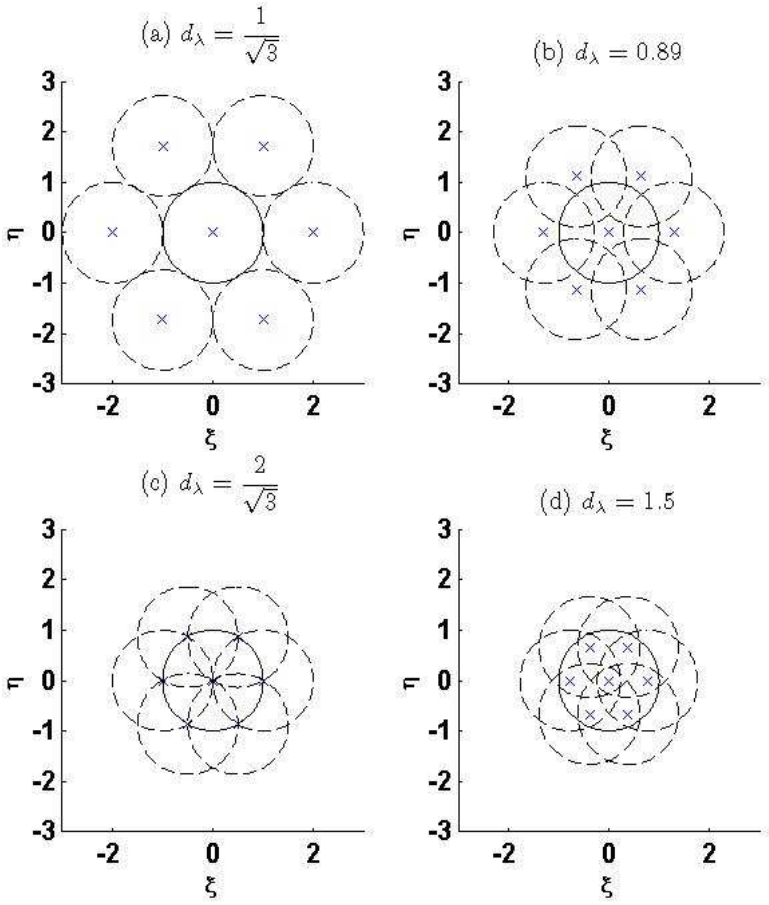

Figure 2.6: Hexagonal Sampling Showing the 6 Closest Aliases Given Various Values of D_λ (a) Nyquist Spacing (b) SMOS Spacing with Reduced UFOV (c) Maximum Spacing where UFOV Reduces to Zero (d) Aliases Within the Unit Circle, No UFOV

For the GeoSTAR instrument, where the Earth disk fills only a 17.2^0 beam, and considering the fact that the cold sky background is constant and small (~2.7 K), image aliases of the cold sky region can be tolerated. Figure 2.7 demonstrates this with images of an actual Earth disk as viewed from GEO with spacing close to the limit where the

disks would overlap. In this case, with a constant known background, the FOV is defined by the areas of the central Earth disk that do not overlap with any of the Earth disk aliases. This formulation is closer to the radio astronomy case, with an extended source.

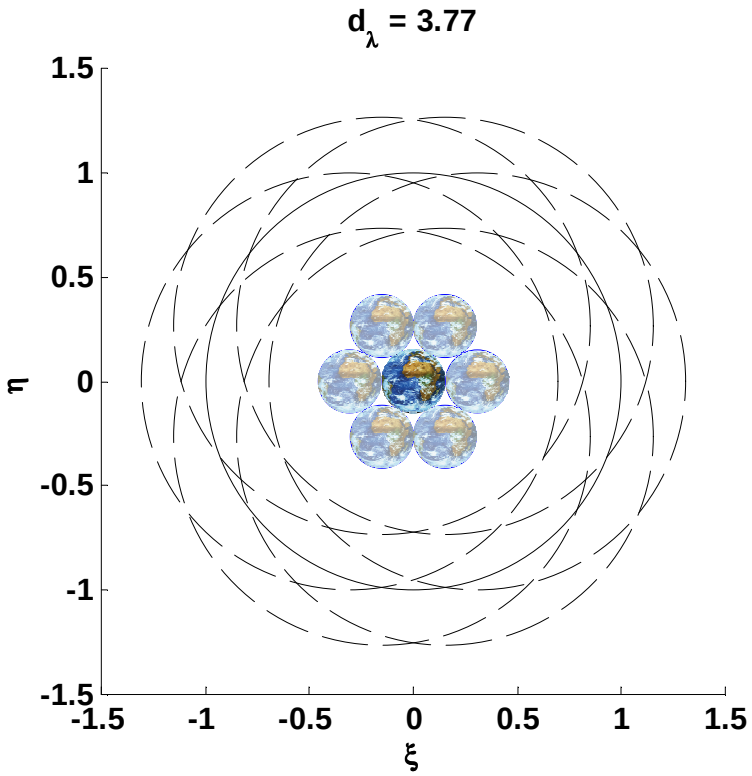

Figure 2.7: Hexagonal Sampling Image Aliases Showing the Limit of the Earth Disk

Past the UFOV limit, the FOV - assuming that the background levels are small and known and given a fixed Earth disk extent - can be represented by

$$\theta_{FOV\_Hex} = \sin^{-1}\left(\frac{1}{\sqrt{3}d_{\lambda}}\right), \text{ when } \theta_{FOV\_Hex} \geq \theta_{FOV\_Earth} \tag{2.14}$$

$$\theta_{FOV\_Hex} = 2\sin^{-1}\left(\frac{1}{\sqrt{3}d_{\lambda}}\right) - \theta_{FOV\_Earth}, \text{ when } \theta_{FOV\_Hex} < \theta_{FOV\_Earth} \tag{2.15}$$

Where

θ_{FOV_Hex} = Off-Nadir Field of View Extent Hexagonal Sampling [rad]

θ_{FOV_Earth} = Off-Nadir Earth Disk Extent [rad]

Equation (2.14) represents the nominal case represented by Figure 2.7 where the multiple Earth disk image aliases do not overlap with the original. If there are overlaps from the

Earth disk, then the field of view is reduced even further by discarding the overlapping areas. The FOV can then be calculated using (2.15).

2.1.5 RECONSTRUCTED IMAGE ERRORS

The errors in visibilities can be related to the T_B image error using the unitary property of the Fourier transform, otherwise known as Parseval's Theorem. The root sum square (RSS) of the elements in the visibility domain equals the root mean square (RMS) of the pixels in the image domain [41]. If we are able to properly characterize the errors in the visibility measurements, we can then estimate the total RMS error in the image.

Contributors to the error in the visibility, and eventually the retrieved pixel, can be broadly divided into three components – antenna gain errors, visibility gain errors and visibility additive errors – as follows

$$\Delta T(\xi,\eta) = \sqrt{\Delta T(\xi,\eta)_{\Delta Ant}{}^2 + \Delta T(\xi,\eta)_{\Delta V}{}^2} \tag{2.16}$$

Where

$\Delta T(\xi,\eta)$	=	Retrieved Pixel Error [K]
$\Delta T(\xi,\eta)_{\Delta Ant}$	=	Pixel Error Due to Antenna Errors [K]
$\Delta T(\xi,\eta)_{\Delta V}$	=	Pixel Error Due to Visibility Errors [K]

Gain errors are typically expressed as a fraction of the total gain and additive errors are expressed in units of Kelvins [K]. The expression for the error in a single pixel $\Delta T(\xi,\eta)_{\Delta V}$ due to visibility errors is then given by [41]

$$\Delta T(\xi,\eta)_{\Delta V} \approx \left(\frac{1}{A_U}\right)\left(\frac{\Omega\sqrt{1-\xi^2-\eta^2}}{\left|F_n(\xi,\eta)\right|^2}\right)\sum_{k=1}^{N}\sqrt{\Delta V_{\mathrm{Re}}(u_k,v_k)^2 + \Delta V_{\mathrm{Im}}(u_k,v_k)^2} \tag{2.17}$$

Where

A_U	=	Field of View Area
N	=	Number of Complex Visibilities Including Hermitian Conjugates (2.7)

The external factor A_U accounts for the field of view area due to the sampling which is a constant with a given array. Even when the antennas are considered identical, a weighting is apparent from the pixel position in the visibility space. The antenna pattern generally peaks at the center and rolls-off from nadir. As such the pixel error is smaller in the center of the image space and increases away from the center. In most cases, it is sufficient to use a constant to represent the effect of the antenna pattern.

The error term, $\sqrt{\Delta V_{\mathrm{Re}}(u_k, v_k)^2 + \Delta V_{\mathrm{Im}}(u_k, v_k)^2}$, represents the errors in the real and imaginary components of the visibility, respectively, which are a combination of both the gain and additive errors. This will be discussed in the next section. The key property of expression (2.17) is that the error in every visibility measurement contributes to the error in each image pixel.

For the antenna gain errors, the pixel errors are highly dependent on the magnitude of the measured visibilities, as can be seen in

$$\Delta T(\xi, \eta)_{\Delta Ant} \approx \eta_{k,Ant} \sum_{k=1}^{N} \sqrt{V_{\mathrm{Re}}(u_k, v_k)^2 + V_{\mathrm{Im}}(u_k, v_k)^2} \tag{2.18}$$

Where

$\eta_{k,Ant}$ = Antenna Gain Error $\left(\Delta G_{k,Ant} / G_{k,Ant}\right)$

A larger visibility magnitude contributes more to the image pixel error. In general, the magnitude of the visibilities is highest in the center of the visibility domain and decreases very quickly as a function of the distance from the center.

The DC component in visibility space has the largest magnitude, often orders of magnitude larger than the other components, and as such requires the most stringent gain stability requirements. As this specification is difficult to achieve for the entire array, the total power measurement is often performed with the same physical antenna but with

special gain-stabilized receivers. In the case of SMOS, this measurement is performed by three separate noise injection radiometers (NIR) that are not part of the interferometric array [54].

2.1.6 VISIBILITY SENSITIVITY

The sensitivity of a traditional total power radiometer is outlined in Section 1.3. An excellent discussion of the sensitivity of various other receiver configurations is given by Tiuri [18, 55]. For a correlating radiometer, the expression for sensitivity must be modified, primarily because the signals being correlated are a function of two physically different receiver systems. The full expression was derived by Ruf *et al.* [29] and represents the general scene dependent case with no underlying assumptions

$$\begin{aligned}\Delta V_{\mathrm{Re}\_a}(u,v) &= \frac{1}{\sqrt{2B\tau}}\left[\left(T_{Ai}+T_{Ri}\right)\left(T_{Aj}+T_{Rj}\right)+V_{\mathrm{Re}}^2(u,v)-V_{\mathrm{Im}}^2(u,v)\right]^{1/2} \\ \Delta V_{\mathrm{Im}\_a}(u,v) &= \frac{1}{\sqrt{2B\tau}}\left[\left(T_{Ai}+T_{Ri}\right)\left(T_{Aj}+T_{Rj}\right)+V_{\mathrm{Im}}^2(u,v)-V_{\mathrm{Re}}^2(u,v)\right]^{1/2}\end{aligned} \tag{2.19}$$

Where

$\Delta V_{\mathrm{Re}\_a}(u,v)$	=	Sensitivity in the Real Component of Visibility (Additive) [K]
$\Delta V_{\mathrm{Im}\_a}(u,v)$	=	Sensitivity in the Imaginary Component of Visibility (Additive) [K]
$V_{\mathrm{Re}}^2(u,v)$	=	Real Visibility Components Squared [K^2]
$V_{\mathrm{Im}}^2(u,v)$	=	Imaginary Visibility Components Squared [K^2]
T_{Ri}, T_{Rj}	=	Receiver Noise Temperature, Subscript Denotes Different Receivers [K]
T_{Ai}, T_{Aj}	=	Scene Brightness Temperature as Measured by the Different Antennas [K]
B	=	Pre-detector Bandwidth [Hz]

The results are given for a complex correlator in which the visibility is measured in terms of the real and imaginary components (in-phase and quadrature) and represent the additive portion of the visibility uncertainty.

For most typical images, the visibility components are often orders of magnitude smaller than the receiver or antenna brightness, except for the central-most visibilities. If

we also assume that the receivers and antennas are close to identical, we can rewrite (2.19) as

$$\Delta V_{\mathrm{Re}\_a}(u,v) = \Delta V_{\mathrm{Im}\_a}(u,v) \approx \frac{T_A + T_R}{\sqrt{2B\tau}} \tag{2.20}$$

Expression (2.20) differs from the total power radiometer case by a factor of $1/\sqrt{2}$ as the correlations are performed with two independent sources of receiver noise, one in each branch of the correlating receiver pair. With the advent of digital sampling, the effects of quantization must also be taken into account. The truncation and rounding of values to coarse quantization levels generates additional frequency components that modify the signal, essentially adding quantization noise [27] . The quantization efficiency is defined to account for the information lost as shown

$$\eta_Q = \frac{SNR_{quantized}}{SNR_{unquantized}} \tag{2.21}$$

Common values of quantization efficiency are shown in Table 2.1 where β is the over-sampling factor. At the lowest quantization (2-level, 1-bit), the efficiency is $2/\pi$.

Table 2.1: Quantization Efficiency [27]

Quantization Levels	$\eta_Q(\beta = 1)$	$\eta_Q(\beta = 2)$
2	0.64	0.74
3	0.81	0.89
4	0.88	0.94
∞	1	1

Taking into account the quantization efficiency modifies (2.20) to

$$\Delta V_{\mathrm{Re}\_a}(u,v) = \Delta V_{\mathrm{Im}\_a}(u,v) \approx \frac{1}{\eta_Q}\frac{T_A + T_R}{\sqrt{2B\tau}} \tag{2.22}$$

So far the expressions have been derived assuming that there are no gain variations in the system. While frequent calibration can be performed to characterize the bulk drifts in the system, gain errors are inherent in any practical system. The gain error can be expressed by

$$\Delta V_g(u,v) \approx \frac{1}{\eta_Q} \eta_{Sys} \left(T_{Sys} \right) \tag{2.23}$$

Where

η_{Sys} = System Gain Error $\left(\frac{\Delta G_{Sys}}{G_{Sys}} \right)$

T_{Sys} = System Brightness Temperature $\left(T_{Sys} = T_A + T_R \right)$ [K]

Assuming that the errors are due to different processes and considered statistically independent, the gain error term (2.23) can be added in a root-sum-square sense to (2.22) resulting in

$$\Delta V_{\mathrm{Re}}(u,v) = \Delta V_{\mathrm{Im}}(u,v) \approx \frac{T_{Sys}}{\eta_Q} \sqrt{\frac{1}{2B\tau} + \eta_{Sys}^2} \tag{2.24}$$

which is the full expression for the visibility error including both the additive and gain error terms. In order to arrive at the final measure of the image errors, the visibility errors must still be combined with the antenna weighting (2.17).

2.2 GeoSTAR Requirements

The GeoSTAR design was briefly discussed in Section 1.6 and will be presented here in detail based on the theoretical background presented in Section 2.1. GeoSTAR is intended to be the functional equivalent of AMSU in GEO, having approximately the same spatial resolution but increased coverage and much improved temporal resolution.

It is then prudent to examine the AMSU performance characteristics so that we may derive comparable GeoSTAR requirements.

2.2.1 AMSU

The Advanced Microwave Sounding Unit (AMSU) consists of two sub-instruments, AMSU-A and AMSU-B [56]. AMSU-A is a temperature sounder (T-sounding) while AMSU-B is the humidity sounder (q-sounding). AMSU-A has 15 channels between 23.8 GHz and 89.0 GHz with the majority of channels at ~50 GHz for temperature sounding.

The instrument spot beamwidth is 3.3^0, which translates into a ~50 km footprint at nadir. This footprint increases off-nadir according to the geometry due to the EIA. Figure 2.8 depicts the relative footprint size with scan position. The central 15 pixels all have approximately 50 km resolution.

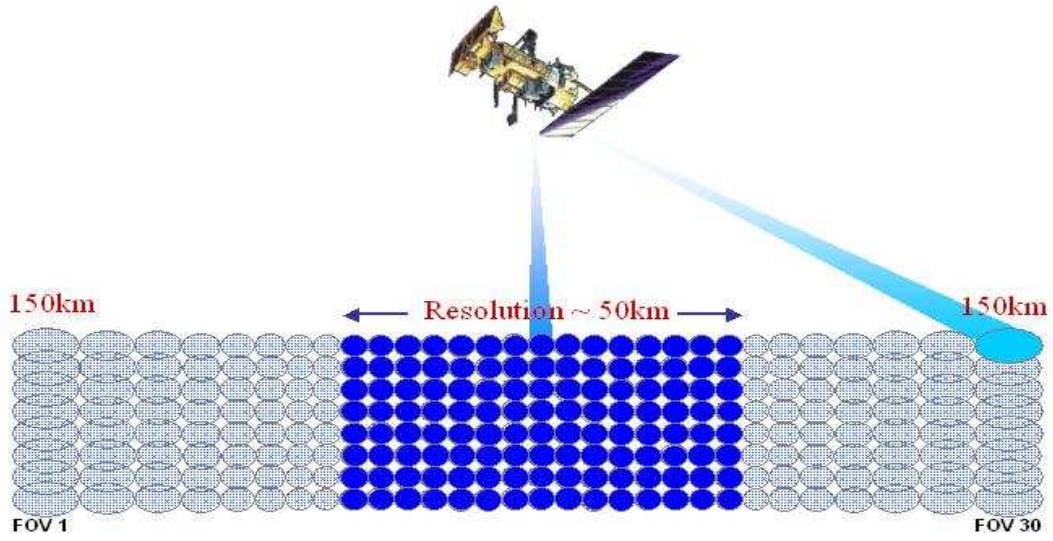

Figure 2.8: AMSU-A Scanning Geometry and Resolution
Courtesy of the Cooperative Institute for Meteorological Satellite Studies
At the University of Wisconsin-Madison, http://cimss.ssec.wisc.edu/

Table 2.2 lists the AMSU-A channels and their relevant parameters. The other channels are used to correct for a variety of parameters to aid in the temperature profile retrieval. The sensitivity of the channels vary, but the tropospheric temperature channels have NEΔT values of 0.25 K.

Table 2.2: AMSU-A Channel Specifications

Channel Number	Frequency [GHz]	Nadir Polarization	Number of Sidebands	NEΔT [K]	Function
1	23.8	Vertical	1	0.30	Water Vapor Burden
2	31.4	Vertical	1	0.30	Water Vapor Burden
3	50.3	Vertical	1	0.40	Water Vapor Burden
4	52.8	Vertical	1	0.25	Water Vapor Burden
5	53.596±0.115	Horizontal	2	0.25	Tropospheric Temperature
6	54.4	Horizontal	1	0.25	Tropospheric Temperature
7	54.94	Vertical	1	0.25	Tropospheric Temperature
8	55.5	Horizontal	1	0.25	Tropospheric Temperature
9	57.290	Horizontal	1	0.25	Stratospheric Temperature
10	57.290±0.217	Horizontal	2	0.40	Stratospheric Temperature
11	57.290±0.3222 ±0.048	Horizontal	4	0.40	Stratospheric Temperature
12	57.290±0.3222 ±0.022	Horizontal	4	0.60	Stratospheric Temperature
13	57.290±0.3222 ±0.010	Horizontal	4	0.80	Stratospheric Temperature
14	57.290±0.3222 ±0.0045	Horizontal	4	1.20	Stratospheric Temperature
15	89.0	Vertical	1	0.50	Stratospheric Temperature

AMSU-B has 5 channels from 89.0 GHz to 183.3 GHz with the majority spaced around the 183 GHz water vapor line. Table 2.3 lists the AMSU-B channels and the relevant parameters. Three channels are on the 183 GHz water vapor line with varying bandwidths. An appropriate value that can be used for the maximum sensitivity is an NEΔT of 1 K. This instrument has a narrower beamwidth of 1.1^0, resulting in a nadir resolution of 16.3 km. A total of 90 scan positions are measured to form a single swath as opposed to 30 for AMSU-A.

Table 2.3: AMSU-B Channel Specifications

Channel Number	Frequency [GHz]	Nadir Polarization	Number of Sidebands	NEΔT [K]	Function
16	89.0±0.9	Vertical	2	0.37	Window Channel
17	150.0±0.9	Vertical	2	0.84	Humidity Profiling
18	183.31±1.00	Vertical	2	1.06	Humidity Profiling
19	183.31±3.00	Vertical	2	0.70	Humidity Profiling
20	183.31±7.00	Vertical	2	0.60	Humidity Profiling

2.2.2 GeoSTAR Minimum Requirements

The GeoSTAR requirements are based on the AMSU specifications as described in the previous section. As GeoSTAR utilizes a synthetic aperture, having many very different frequency bands is not as simple as it is with a traditional total power radiometer. For a traditional scanning system, all that is required is a radiometer receiver back end with a single antenna that is compatible with the reflector. For an interferometric array, the antennas and receivers are tuned for a single frequency band. If the frequencies are significantly different, an entirely new antenna array must be constructed. To this end, only two primary frequency bands are selected, the 50 GHz

oxygen line wing and the 183 GHz water vapor line, compared to the numerous bands available to AMSU. While this is a reduction in scope of the microwave instrument compared to AMSU, recall that GeoSTAR will operate in concert with a host of other instruments on the GOES platform [7, 57] that will provide for the missing data.

Table 2.4 outlines the minimum requirements as it will relate to the interferometric array design. For the temporal resolution, the upper bound is given by the NWP models that only generate new output fields every 3 hours. If faster refresh rates are available, investigation of more dynamic atmospheric processes are possible. An image refresh rate of every half-hour is targeted.

Table 2.4: GeoSTAR Minimum Requirements Based on AMSU

Parameter	'T'-Array	'q'-Array
Frequency Band [GHz]	50	183
Number of Channels	4	3
Nadir Spatial Resolution [km]	50	25
Image Pixel Error [K]	<1	<1
Temporal Resolution [h]	<1.5	<1.5

The number of channels available effectively determines the vertical resolution of the profiles. For a synthetic array the single channel dwell time is effectively multiplied by the number of channels to arrive at the temporal resolution. If an instrument generates images every half-hour, then all channels must be measured within that time frame. For a 4 channel system, that is effectively 7.5 minutes per channel, including the calibration duty cycle. A balance between the scientific requirements and the hardware performance must be made. The requirements list the lowest number required for scientific use, if additional channels are available given the expected hardware capabilities, higher quality products can be generated.

2.3 GEOSTAR DESIGN

Several top level design parameters have already been determined during the preceding sections, notably the selection of a Y-array configuration and the two frequency bands of the measurements. From the requirements in Table 2.4, the array parameters are derived from the theory outlined in section 2.1. Table 2.5 summarizes the results for a GOES instrument optimized for an Earth disk FOV. The length of the longest arm will be 2.29 m (radius of the synthetic array) and a total of ~900 antenna-receiver pairs will be required. In addition, ~300 thousand correlations are necessary during a single measurement realization.

Table 2.5: GeoSTAR Array Parameters for the Temperature ('T') and Humidity ('q') Arrays

Parameter	Design Eq.	Ref.	'T'-Array	'q'-Array
d_λ	$\theta_{FOV\_Hex} = \sin^{-1}\left(\frac{1}{\sqrt{3}d_\lambda}\right)$	(2.15)	3.85	3.85
d [cm]	$d = \lambda d_\lambda$	-	2.29	0.63
$\Delta\theta_{Hex}$ [rad]	Arc Angle	-	1.4e-3	7.0e-4
N_{EL}	$\Delta\theta_{Hex} \approx \frac{\pi}{4\sqrt{3}}\left(\frac{1}{N_{EL}d_\lambda}\right)$	(2.10)	~100	~200
d_{Max} [m]	$d_{Max} = N_{EL}d$	-	2.29	1.26
N_T	$N_T = 3N_{EL} + 1$	(2.5)	301	601
N	$N = 2\left(3N_{EL}^2 + 3N_{EL}\right) + 1$	(2.7)	60601	241201

Achieving the spacecraft power requirements for both the receiver units and the correlators is a challenging task, but beyond the scope of this discussion. This design merely demonstrates that it is possible to configure the array to perform the required measurements.

In addition to the array design, the image retrieval parameters must also be determined. If we assume that the three different components of the error (Section 2.1.5)

are independent, an equal split of the maximum 1 K error allocates 0.58 K ($1/\sqrt{3}$) for each error component. Evaluating the image error requires many assumptions regarding the future system performance in terms of the receiver hardware. The system bandwidth is determined by the particular frequency channel. At 183 GHz we will use a bandwidth of 1 GHz. Table 2.6 summarizes the assumptions.

Table 2.6: GeoSTAR Image Error Assumptions

Parameter	'T'-Array	'q'-Array	Note
T_R [K]	300	500	Receiver Temp.
T_A [K]	100	120	Antenna Temp.
B [MHz]	200	1000	Bandwidth
$\eta_Q(\beta=1)$	0.64	0.64	Quantization Efficiency
A_K	2	2	$\left(\frac{1}{A_U}\right)\left(\frac{\Omega\sqrt{1-\xi_k^{\,2}-\eta_k^{\,2}}}{\lvert F_n(\xi_k,\eta_k)\rvert^2}\right)$
Visibility Mean [K]	$1e^{-2}$	$1e^{-2}$	$\sqrt{V_{\mathrm{Re}}(u_k,v_k)^2+V_{\mathrm{Im}}(u_k,v_k)^2}$

In addition to the hardware assumptions two imaging parameters are assumed. The antenna gain error, which is a function of the visibility magnitude, is found by estimating the mean value of the visibilities measured and set at 10^{-2}. This value can be refined in Chapter 6, once more realistic distributions of visibilities have been determined. The antenna pattern weighting which varies with distance from the visibility center, is assumed to be a constant at 2. This value is consistent with the demonstrator parabolic Potter horn at 50 GHz to be discussed in Section 2.4.2 [58, 59].

The GeoSTAR image retrieval parameters are presented in Table 2.7 for the three parameters of interest – the antenna gain error $\eta_{k,Ant}$, the visibility gain error η_{Sys} and the integration time τ.

Table 2.7: GeoSTAR Image Retrieval Parameters Temperature ('T') and Humidity ('q') Arrays

Parameter	Design Eq.	Ref.	'T'-Array	'q'-Array
$\eta_{k,Ant}$ [%]	$\Delta T(\xi,\eta)_{\Delta Ant} \approx \eta_{k,Ant} \sum_{k=1}^{N} \sqrt{V_{\mathrm{Re}}(u_k,v_k)^2 + V_{\mathrm{Im}}(u_k,v_k)^2}$	(2.18)	1.7	0.8
$\Delta V_{\mathrm{Re/Im}}(u,v)$ [K]	$\Delta T(\xi,\eta)_{\Delta V} \approx 2\sum_{k=1}^{N} \sqrt{2.\Delta V_{\mathrm{Re/Im}}(u_k,v_k)^2}$	(2.17)	8.3e^{-4}	4.2e^{-4}
η_{Sys} [%]	$\Delta V_g(u,v) \approx \frac{1}{\eta_Q}\eta_{Sys}(T_{Sys})$	(2.23)	1.3e^{-4}	4.3e^{-5}
τ [min]	$\Delta V_a(u,v) \approx \frac{1}{\eta_Q}\frac{T_{Sys}}{\sqrt{2B\tau}}$	(2.22)	24	46

The antenna gain error yields results of 1-2% which is achievable with proper antenna structural engineering and calibration. In addition, flexing and bending of the array are more significant problems at the end of the array arms, where there is typically less support. Furthermore, since the error is a function of the visibility magnitude which is smallest for the element farthest away from the center, this design specification can be easily met.

The visibility gain error is a much more difficult specification to meet given the current assumptions. A 1 parts-per-million (ppm) uncertainty is very difficult to meet, even with a well calibrated Dicke receiver. Achieving this specification with the current assumptions requires a better receiver design or quantization scheme. Recall that the gain error is also a function of the antenna, which we have estimated using the antenna constant (A_K).

The integration time with these nominal values does not meet the minimum requirements that were presented in Table 2.4, by almost a factor of 2. Clearly the current nominal values for the expected design must be improved and the assumptions refined. There are significant challenges that must be met before GeoSTAR can meet the design requirements.

2.4 GeoSTAR Demonstrator Hardware

The GeoSTAR demonstrator (GeoSTAR-D) was developed jointly at the University of Michigan and the Jet Propulsion Laboratories [39] under the NASA Instrument Incubator Program (IIP) to address the challenges faced by the full space borne instrument. The reduced array will consists of a total of 24 antenna elements, operate at 50 GHz and will demonstrate the measurement concept, calibration and image reconstruction methods, as well as provide crucial experience in dealing with the hardware. The success of the demonstrator will raise the technology readiness level (TRL) of various components of the instrument significantly.

Figure 2.9 shows the original system block diagram with a single receiver called out. The following sub-sections highlight the key components and notable results of the development prior to the full integration of the demonstrator. Not pictured in Figure 2.9 is the Dicke radiometer used for total power measurement.

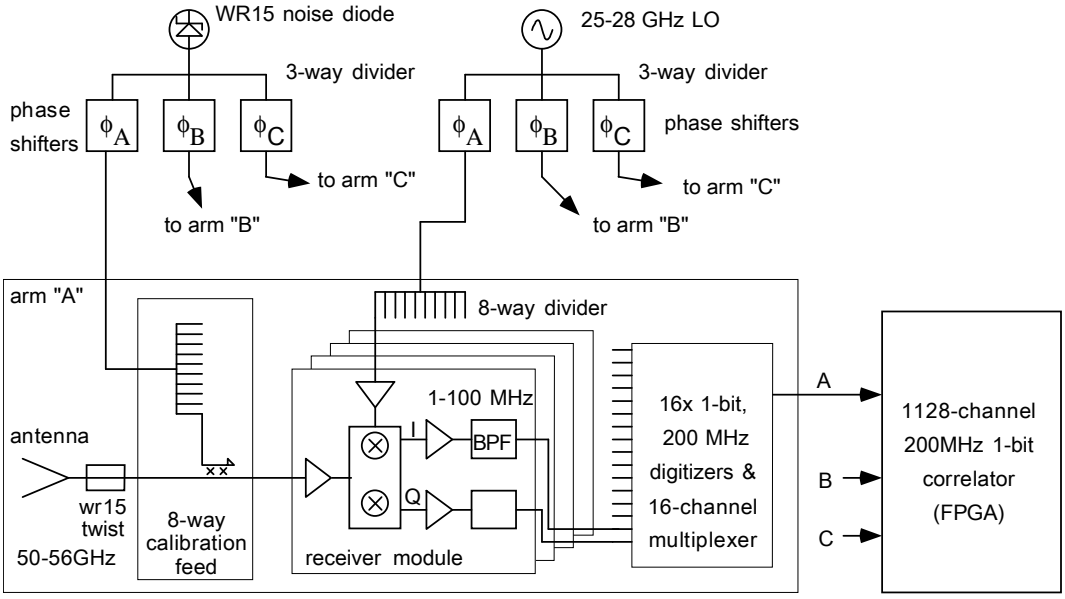

Figure 2.9: System Block Diagram of GeoSTAR-D Showing a Single Receiver Courtesy of Alan Tanner at JPL

2.4.1 ANTENNA ARRAY

The baseline antenna array selected was the Y-array configuration yielding hexagonal sampling in the visibility domain. During the hardware integration, it was found that the physical dimensions of the receivers and antennas made it difficult to accommodate the central element in the array. Tanner proposed that an offset Y-array configuration be adopted, where the central element is removed. Figure 2.10 shows the antenna array layout with the corresponding visibility sampling.

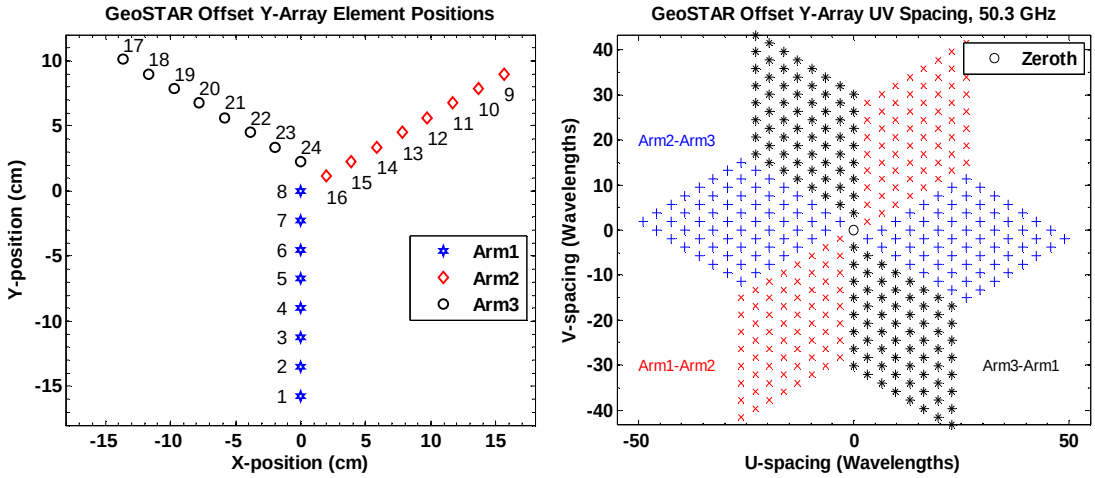

Figure 2.10: GeoSTAR Offset 'Y' Antenna Configuration and the Corresponding UV Sampling

The offset Y-array modifies several of the theoretical formulations, notably reducing the total number of visibilities measured and the pixel resolution, Table 2.8.

Table 2.8: Offset Y-Array Design Equations

Parameter	Y-Array	Ref.	Offset Y-Array	Ref.
N	$2\left(3N_{EL}^2+3N_{EL}\right)+1$	(2.7)	$2\left(3N_{EL}^2\right)+1$	(2.25)
$\Delta\theta_{Hex}$	$\frac{\pi}{4\sqrt{3}}\left(\frac{1}{d_\lambda N_{EL}}\right)$	(2.10)	$\frac{\pi}{4\sqrt{3}}\left(\frac{1}{d_\lambda\left(N_{EL}-1/3\right)}\right)$	(2.26)

As the number of elements in each arm increases, both parameters tend to original formulation. Note that for the demonstrator, where $N_{EL}=8$ and is small, this reduction

has a noticeable impact. The physical spacing between elements is 2.25 cm, which results in a wavelength element spacing $d_\lambda = 3.77$ at 50.3 GHz. At the higher frequencies (55.5 GHz), the FOV is reduced from the slightly from ~17.6^0 to ~15.9^0. The physical spacing also determines the maximum aperture diameter of the antennas. A larger aperture is desirable as it increases the gain of the antennas and the received energy from the Earth disk.

2.4.2 ANTENNA DESIGN

The optimum antenna design for GeoSTAR use would have a uniform gain over the Earth disk and be zero elsewhere to suppress the aliased signals. A more realistic design would have high beam efficiency over the extent of the Earth disk with low side lobe levels. Given the physical limitations of the array configuration, two candidate designs fulfill these requirements - a parabolic Potter horn and a straight-taper horn. Both designs have a high Earth disk beam efficiency of over ~40% and low far side lobe levels of -30 dB. The Gaussian shape of the antenna pattern ensures large suppression away from the main beam.

An additional requirement of the antenna design is to minimize the coupling between the antenna elements, such that the antenna patterns area not modified by the structures surrounding them. This requirement is of particular importance for the space borne instrument as it will allow for the theoretical model of the antennas to be used in place of costly full array measurements, in addition to maximizing the available aperture area. The demonstrator will be invaluable in determining the effectiveness of using the theoretical model, as antenna range measurements are significantly simpler with a smaller array. If the errors between the theoretical model and the antenna range measurements

are within the tolerances (Approximately 1%, see Table 2.7), a careful full array measurement becomes redundant, and only a functional test is necessary. This reduces costs significantly.

An evaluation of the two antenna designs was performed at JPL by placing antennas adjacent to antenna under test and determining the perturbations in the antenna pattern [60]. The results of the analysis for the case where the antennas placed on both sides of the antenna under test indicate that the Potter horn performs best with typical errors on the order of 0.1% at vertical polarization. The errors for horizontal polarization are slightly larger, 0.3%. For the straight taper horn, the errors were an order of magnitude larger (~2%).

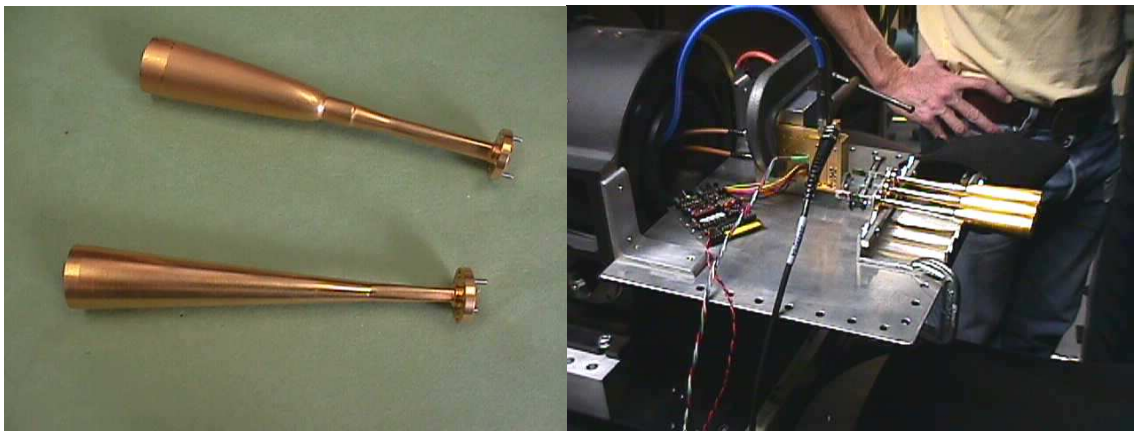

Figure 2.11: Left – Parabolic Potter Horn (Top), Straight Taper Horn (Bottom) Right –Antenna Test Setup with Two Terminated Antennas 2.25 cm to Either Side
Courtesy of Alan Tanner at JPL

Figure 2.11 shows the experimental setup with the parabolic Potter horns. The test jig ensures repeatability in the seating of the neighboring antennas. The results indicate that the parabolic Potter horn design is much less sensitive to scattering effects from adjacent elements, and as such represents the baseline antenna design for both the prototype and the final space borne instrument.

2.4.3 RECEIVERS

The monolithic microwave integrated circuit (MMIC) receivers modules were designed at JPL by Kangaslathi et al [61]. Across the 50 to 56 GHz frequency range the noise figure (NF) of the modules vary between 3.4 dB to 4.2 dB. The receivers perform double-sideband second harmonic down conversion to two IF signals in phase-quadrature with an output bandwidth of 100 MHz. The gain of the receiver module is approximately 90 dB. The total receiver power consumption is approximately 360 mW which must be reduced considerably for the spaceborne version.

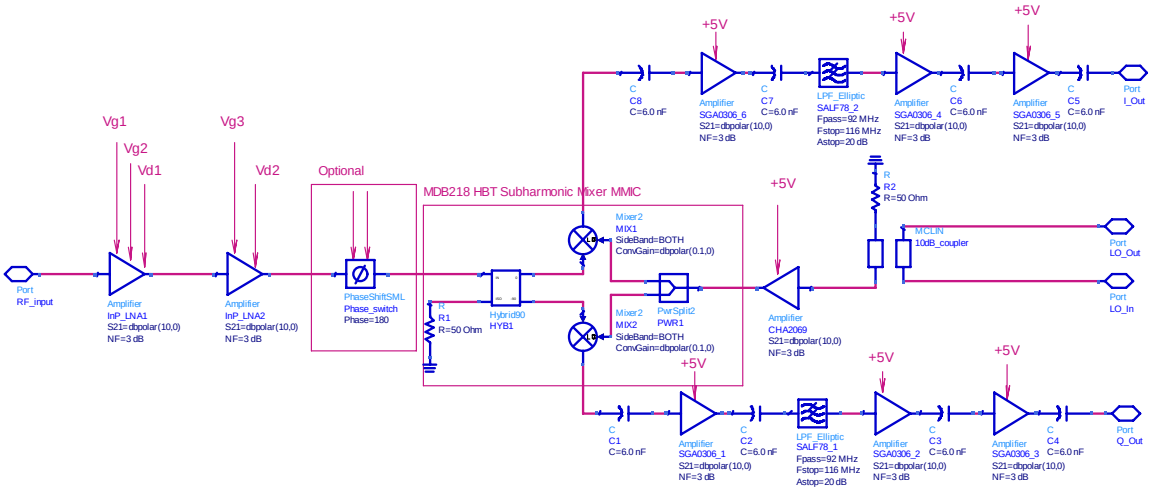

Figure 2.12: Block Diagram of the MMIC Receiver Prototype
Courtesy of Pekka Kangaslathi at JPL

During development, it was determined that the isolation between the receivers was insufficient for the closest elements in the array. To suppress these levels, ferrite isolators are added to the two innermost elements in each arm, reducing the coupling of the closest 6 elements in the center of the array. The rest of the array operates without the isolators as the coupling is minimal, and isolators would increase the noise figure of the system unnecessarily.

2.4.4 LOCAL OSCILLATOR (LO) SYSTEM

The local oscillator signal from 25 to 28 GHz is split three ways into a phase switch and buffer amplifier module (see Figure 2.9). The phase switch periodically changes the phase to four positions, 0, 45, 90 and 135 degrees, which results in phases of 0, 90, 180 and 270 at the second harmonic RF [59]. A coupled detector with feedback controls the LO amplifier gain ensuring constant LO power. The phase shifting scheme allows for the estimation of the correlator biases and the quadrature balance by shifting the results through different quadrants. This measurement scheme performs remarkably well, eliminating the digitizer null offsets, and laboratory measurements match the expected theoretical NEΔV levels to integration times of more than 2 hours.

2.4.5 NOISE DIODE DISTRIBUTION SYSTEM

A common noise diode (ND) is injected into all 24 receivers as a calibration reference to track the system gain, phase and receiver noise drifts. The noise diode signal is distributed utilizing a similar phase shifting network as the LO and was originally implemented to perform the quadrature balance of each correlator. This proved to be redundant with the efficiency of the LO phase shifting system [41]. The injected noise diode signal magnitude at each receiver is approximately 5 K.

2.4.6 DIGITAL BACK-END

The digital back-end system is implemented in a field programmable gate array (FPGA). The output from each receiver is an in-phase and quadrature signal with bandwidth 100 MHz. The digital back-end was originally designed to sample at 200 MHz to recover the full double sideband bandwidth. However, timing problems in the

correlator system required a relaxation of this specification. The current sampling rate is 110 MHz, so we do not fully utilize the available bandwidth.

Four 1-bit correlations are performed simultaneously per receiver pair, resulting in II, IQ, QI and QQ measurements. In addition to the correlations, several other measurements are performed to evaluate their usefulness. The original signal is sampled with full 8-bit resolution, before being reduced to 2-bits and summed to form totalizers. The totalizers can be used as an additional means of total power measurement.

The nominal integration time of the system is 10 ms with a 90 % duty cycle for signal timing and settling. The system allows for maximum flexibility, each measurement period can be configurable in terms of the center frequency and target (antenna or noise diode) through the means of an initialization file.

2.4.7 HARDWARE DESIGN SUMMARY

The hardware design of the demonstrator follows that of the eventual space borne instrument on a reduced scale, allowing for evaluation of the various concepts, especially those pertaining to instrument calibration and image retrieval. Table 2.9 summarizes the various components of the design from the initial signal reception to the digital measurement system.

Table 2.9: GeoSTAR Demonstrator Hardware Design Summary

Parameter	Value	Notes
Array topology	Offset Y-Array	No central element
D	2.25 cm	Spacing unit between elements
θ_{FOV_Hex} (2.15)	17.6^0 to 15.9^0	Frequency dependent
N_{EL}	8	Total of 24 elements
N (2.25)	385	Total number of visibilities
$\Delta\theta_{Hex}$ (2.26)	0.90^0	Image resolution
Antenna design	Parabolic Potter horn	Low mutual coupling
Receiver architecture	MMIC	Low power
Receiver output	In-phase and quadrature	Double sideband mixer
Receiver NF	3.4 to 4.2 dB	~315 to 475 K
LO distribution	3-way with phase shift	Used for calibration
ND distribution	3-way with phase shift	Phase shift redundant
ND magnitude	5 K	Calibration signal
Correlations	1-bit	4 per receiver pair
Sampling frequency	110 MHz	110 MHz bandwidth
Fundamental Integration period	9 ms	90% duty cycle ~10 ms

Figure 2.13 shows an image of GeoSTAR-D during integration, prior to the addition of the enclosure for thermal control.

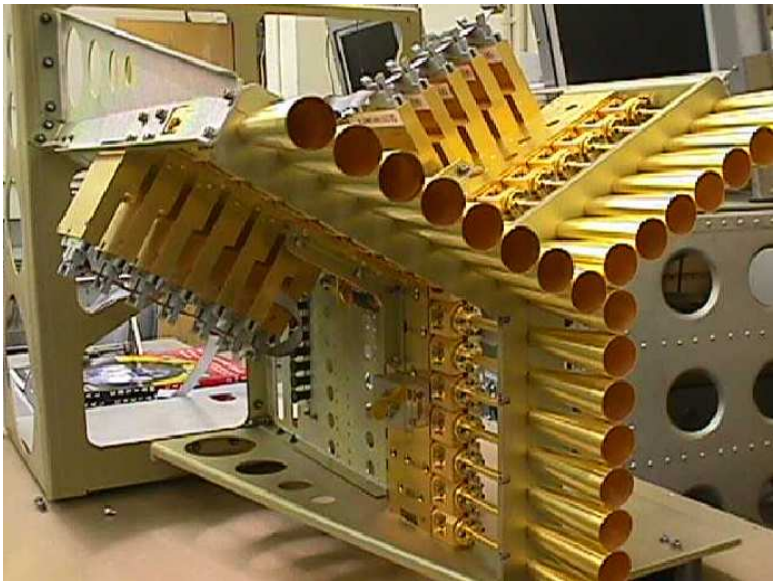

Figure 2.13: GeoSTAR Demonstrator Early Integration Image
Courtesy of Steve Dinardo at JPL

The antenna array appears in the foreground of the image, with the offset Y-array configuration. Note how closely the antennas apertures are spaced to maximize the aperture area. Recall that low mutual coupling is inherent with the parabolic Potter horn design selection.

The mechanical support for the array ensures minimal shifting of the antenna elements. The noise diode distribution network is visible behind the antennas and the receivers connected next in the signal path. The digital back-end is not visible in this image. GeoSTAR-D is currently equipped with the following features:

1. Sturdy housing for fully packaged system
2. Active temperature control system
3. Mylar radome to protect the antennas and improve temperature stability
4. Integrated Dicke radiometer for independent zeroth visibility measurements
5. Mounting stand which allows for repeatable changes to roll, pitch and yaw

The current GeoSTAR-D configuration allows for robust field application work while maintaining instrument stability for high quality data products.

2.5 SUMMARY

The theoretical basis of interferometric measurements is presented, focusing on the key parameters for system design. Reasonable assumptions are used to distill the equations into practical usable form that can be used to quickly ascertain the full system design parameters. The GeoSTAR requirements, based on the current AMSU specifications, is presented and used with the theoretical formulas to generate nominal instrument parameters. With the current hardware assumptions, the integration time required exceeds the requirements, but avenues exist to improve this, namely decreasing the quantization error and increasing the main beam antenna gain.

A demonstrator unit, GeoSTAR-D, is fabricated with a reduced array of 24 elements to address the challenges posed by a full sized array. The subsystem development has yielded two notable products, the parabolic Potter horn with low mutual coupling, and the LO phase-shifting measurement scheme that produces unparalleled instrument stability. The calibration and performance of GeoSTAR-D is presented in Chapters 3 and 4.

CHAPTER 3

GEOSTAR-D CALIBRATION AND INSTRUMENT VERIFICATION

3.1 GEOSTAR-D CALIBRATION METHODOLOGY

Traditional radiometers often depend on viewing known external sources as a means of final end-to-end instrument calibration. A simple two-point calibration determines the receiver noise temperature and gain, which in turn allows for the derivation of the antenna brightness temperature. A common method to track receiver gain variation during operation is then the deflection caused by injection of a known noise diode signal, or by comparison to a stable reference load plus an external cold source. Inherent in a two point calibration is the fact that the radiometer is a linear system. The calibration of GeoSTAR visibilities follows a similar two part framework. The final result of the calibration is a properly scaled visibility measurement in K.

The system allows for visibility calibration using either the correlator or the totalizer measurements. While the correlators measure the signal correlation between two different receivers, the totalizers measure the power received in a single receiver. Totalizers perform by counting the number of occurrences at each of the voltage bins, to determine the probability distribution function of the measurement, which is related to the power. For a perfect system, the results determined from each method should be identical regardless of the methodology. For a practical system, the difference in the

results gives a measure of the non-linearity and the correlator efficiency, as will be demonstrated.

3.1.1 TWO-POINT MAGNITUDE CALIBRATION

A standard two point calibration is used to calibrate the receivers and the noise diode reference magnitude. Observations are performed of a target made of absorber material at two known widely separated temperatures, ambient and liquid nitrogen (~77 K). Injecting the noise diode creates stable deflections in the measurements, which when scaled by the system noise temperature can be termed as a noise diode deflection (NDD) ratio, represented by

$$D_N = \frac{T_N}{T_R + T_A} \tag{3.1}$$

Where

D_N	=	Noise Diode Deflection Ratio
T_N	=	Noise Diode Brightness Temperature [K]
T_A	=	Antenna Brightness Temperature [K]
T_R	=	Receiver Noise Temperature [K]

For known targets, we can substitute the physical temperature of the target for the antenna temperature as

$$D_{N\_Amb} = \frac{T_N}{T_R + T_{A\_Amb}} \quad \text{and} \quad D_{N\_LN2} = \frac{T_N}{T_R + T_{A\_LN2}} \tag{3.2}$$

Where

D_{N_Aml}	=	Noise Diode Deflection with Ambient Target
T_{A_Amb}	=	Antenna Brightness Pointing at Ambient Target [K]
D_{N_LN2}	=	Noise Diode Deflection with LN2 Immersed Target
T_{A_LN2}	=	Antenna Brightness Pointing at LN2 Immersed Target [K]

Combining the equations in (3.2), the noise diode brightness temperature can be found by substituting for the receiver noise temperature using (3.3)

$$T_N = \frac{T_{A\_Amb} - T_{A\_LN2}}{\left(\frac{1}{D_{N\_Amb}} - \frac{1}{D_{N\_LN2}}\right)} \tag{3.3}$$

The corresponding receiver noise temperature can then be calculated from

$$T_R = \frac{T_N}{D_{N\_Amb}} - T_{A\_Amb} \quad \textbf{or} \quad T_R = \frac{T_N}{D_{N\_LN2}} - T_{A\_LN2} \tag{3.4}$$

These relationships can be used for either the correlator or the totalizer measurements once they are processed.

3.1.2 TOTALIZER PROCESSING

[start by describing the digitization – 2-bit with these weights at each quantization level] The output from the data system gives us normalized totalizer data in each of the 4 bins (-3, -1, +1, +3). In the data system, measurements are performed with 8-bit resolution and reduced to this 2-bit level. To determine the power in the noise signal from the totalizers, we use the following relationship

$$P(t) = \frac{1 - erf\left(\frac{t}{\sigma\sqrt{2}}\right)}{2} \tag{3.5}$$

Where

t	=	Threshold
σ	=	Standard Deviation of the Noise Signal
$erf(.)$	=	Gaussian Error Function

P denotes the probability of the occurrence of the samples that exceed the threshold (i.e. either the -1 or +1 normalized bins). Note that the modifications to the traditional error function are to scale the limits.

The variance of the signal can then be obtained from

$$P_t = \sigma^2 = \frac{t^2}{2}.\left(\frac{1}{erfinv[1-2P(t)]}\right)^2 \tag{3.6}$$

Where

P_t = Linear Measure of Power in Threshold Units

There are 4 different measurements of power, two each from the positive and negative thresholds of both the I and Q channels. How best to combine these four measurements of power is an ongoing topic of investigation. Currently, we simply use the geometric mean of all four results.

There are two different ways of utilizing these results that are mathematically equivalent if the system is linear and stable. The traditional Y-factor formulation is presented as [14, 19]

$$\text{with } G_Y = \frac{T_{A\_Amb} - T_{A\_LN2}}{P_{t\_Amb} - P_{t\_LN2}} \tag{3.7}$$

Where

G_Y = System Gain Calculated Using Y-Factor Method

P_{t_amb} = Measured Totalizer Power when Pointing at Ambient Target

P_{t_LN2} = Measured Totalizer Power when Pointing at LN2 Immersed Target

Alternatively, the totalizer NDD ratio can be calculated using

$$D_{N\_Amb\_t} = \frac{P_{t\_Amb+ND} - P_{t\_Amb}}{P_{t\_Amb}} = \frac{T_N}{T_{A\_Amb} + T_R}$$
$$D_{N\_LN2\_t} = \frac{P_{t\_LN2+ND} - P_{t\_LN2}}{P_{t\_LN2}} = \frac{T_N}{T_{A\_LN2} + T_R} \tag{3.8}$$

Where

$D_{N\_Amb\_t}$ = Totalizer Ambient Noise Diode Deflection Ratio

$D_{N\_LN2\_t}$ = Totalizer LN2 Noise Diode Deflection Ratio

When (3.8) is combined with (3.3) and (3.4), we arrive at calculations of receiver noise temperature and noise diode brightness temperature.

3.1.3 CORRELATOR DEFLECTION PROCESSING

For correlations measured between two receiver pairs *i* and *j*, the relationship that scales the result to visibilities is

$$\rho_{Aij} = \frac{V_{ij}}{\sqrt{\left(T_{Ri} + T_{Ai}\right)\left(T_{Rj} + T_{Aj}\right)}} \approx \frac{V_{ij}}{T_{Rij} + T_{Aij}} \tag{3.9}$$

Where

ρ_{Aij} = Complex Correlation from the Antenna
V_{ij} = Complex Visibility Component [K]
T_{Rij} = Geometric Mean of Two Receiver Temperatures $\sqrt{T_{Ri}T_{Rj}}$ [K]
T_{Aij} = Geometric Mean of Two Antenna Temperatures $\sqrt{T_{Ai}T_{Aj}}$ [K]

Assuming that the impedance match at the input to the receivers is adequate, we can replace the individual temperatures with the geometric mean of the two in question. When the noise diode is switched on, (3.9) becomes

$$\rho_{Nij} \approx \frac{V_{ij} + V_{Nij}}{T_{Rij} + T_{Aij} + T_{Nij}} \tag{3.10}$$

Where

ρ_{Nij} = Noise Diode Correlation
V_{Nij} = Complex Noise Diode Visibility Component [K]
T_{Nij} = Geometric Mean of Two Noise Diode Temperatures $\sqrt{T_{Ni}T_{Nj}}$ [K]

The same assumptions utilizing the geometric means which are valid if the magnitudes are similar.

The complex noise diode visibility can be related to the brightness temperature by

$$V_{Nij} \approx \sqrt{T_{Ni}T_{Nj}}e^{j\phi_{ij}} = T_{Nij}e^{j\phi_{ij}} \tag{3.11}$$

Where

ϕ_{ij} = Phase Difference Between the Noise Diode Signals

where the *j* factor in the exponent is the imaginary number unit.

Combining (3.9) and (3.10), and substituting for the value of the noise diode visibility using (3.11), we arrive at the expression for noise diode phase difference

$$e^{j\phi_{ij}} \approx \frac{T_{Rij} + T_{Aij}}{T_{Nij}}\left(\rho_{Nij} - \rho_{Aij}\right) + \rho_{Nij} \tag{3.12}$$

Tanner [give reference here] solved this equation by simultaneously solving for the magnitude ratio and phase of the noise diode to arrive at the correlator noise diode deflection ratio between two different receivers

$$D_{Nij\_c} \approx \frac{V_{Nij}}{T_{Rij} + T_{Aij}} = \frac{T_{Nij}}{T_{Rij} + T_{Aij}} e^{j\phi_{ij}} \approx \left(\rho_{Nij} - \rho_{Aij}\right) + \rho_{Nij}\left(\frac{2a}{-b + \sqrt{b^2 - 4ac}}\right) \tag{3.13}$$

Where

$$\begin{aligned} a &= \mathrm{Re}^2\left(\rho_{Nij} - \rho_{Aij}\right) + \mathrm{Im}^2\left(\rho_{Nij} - \rho_{Aij}\right) \\ b &= 2\left[\mathrm{Re}\left(\rho_{Nij}\right)\mathrm{Re}\left(\rho_{Nij} - \rho_{Aij}\right) + \mathrm{Im}\left(\rho_{Nij}\right)\mathrm{Im}\left(\rho_{Nij} - \rho_{Aij}\right)\right] \\ c &= \mathrm{Re}^2\left(\rho_{Nij}\right) + \mathrm{Im}^2\left(\rho_{Nij}\right) - 1 \end{aligned}$$

(3.13) can be used with the previously derived equations (3.3) and (3.4) to arrive at the receiver and noise diode temperatures.

3.1.4 RECEIVER CLOSURE

The totalizers measure the response of the individual receivers, while the correlators are sensitive to the geometric mean of the responses of a pair of receivers. For any three receivers (one in each arm), their geometric means can be combined to arrive at a single result for a receiver[27]

$$T_{Ri} = \frac{\sqrt{T_{Ri}T_{Rj}}}{\sqrt{T_{Rj}T_{Rk}}}\sqrt{T_{Ri}T_{Rk}} \tag{3.14}$$

The correlators perform 192 different measurements, and each receiver can be isolated from 64 different measurement triplets, by changing the combinations in the other two arms. This relationship can also work in reverse, utilizing the totalizer measurements to arrive at the correlator results. The combination of 64 measurements

reduces the noise contribution level. However, the noise is reduced by less than a factor of $64^{1/2} = 8$ because the noise in the measurements is not completely independent.

3.1.5 PHASE CALIBRATION

While the two point calibration calibrates the magnitude of the noise diode and receivers, the phase of the external incoming signal at the antennas must also be processed and related to the phase of the internal calibration source. This process requires a correlated signal that is measured through the antenna inputs. A correlated source in the anechoic chamber can act as an external phase calibrator. If we apply a similar process to (3.13) and instead use the difference in the correlation of an external souce, we arrive at

$$D_{Eij} \approx \frac{T_{Eij}}{T_{Rij} + T_{Aij}} e^{j\phi_{Eij}} \tag{3.15}$$

Where

D_{Eij} = External Source Deflection Ratio
T_{Eij} = Brightness Temperature of External Source
ϕ_{Eij} = Phase Difference of the External Source

The ratio of the deflection, (3.13) to (3.15), relates the external phase to the internal phase reference. The external phase is a function of the position of the source in the anechoic chamber and its position is chosen as the instrument boresight. Explicitly, this is represented as

$$\phi_{Dij} = \phi_{Eij} - \phi_{ij} \tag{3.16}$$

Where

ϕ_{bij} = External Boresight Antenna Phase Correction

A similar formulation is proposed in [62]. The phase calibration is used with the magnitude calibration to form calibrated brightness temperature images from the measurements.

3.1.6 FINAL VISIBILITIES

Once the external calibration measurements are performed, the magnitude of the noise diode is solved for using the noise diode deflection (3.13) with two known external references, as expressed by (3.3) and (3.4). The external phase calibration set to a point at boresight is measured using (3.16). During nominal operation of the instrument, the calibrated visibilities are calculated by combining (3.9) and (3.13) with the inter-element external phase calibration (3.16)

$$V_{ij} = \frac{\rho_{Aij}}{D_{Nij}} \left(T_{Nij} e^{j\phi_{Dij}} \right) \tag{3.17}$$

In (3.17), the terms in the brackets represent the calibration phase and magnitude values that were generated previously. Both ρ_{Aij} and D_{Nij} represent the measured values of the instrument. The calibrated visibilities have units of K.

3.2 INITIAL CALIBRATION RESULTS

The first magnitude calibration measurements of GeoSTAR-D were performed on 09/19/2005 to provide a reference for the anechoic chamber tests. The following compares the results as obtained from the various methods outlined in Section 3.1. Magnitude calibration is performed frequently, especially prior to deployment in measurement campaigns or after the instrument has been shipped.

3.2.1 TOTALIZER LINEARITY

The receiver temperatures were calculated using the totalizer Y-factor, totalizer NDD and correlator NDD methods. Figure 3.1 shows the results with a noticeable spread in the results of each method. Several receivers have much higher temperatures than the

rest, these are the receivers central to the array that have the isolators placed immediately after the antennas to reduce coupling as outlined in Section 2.4.3.

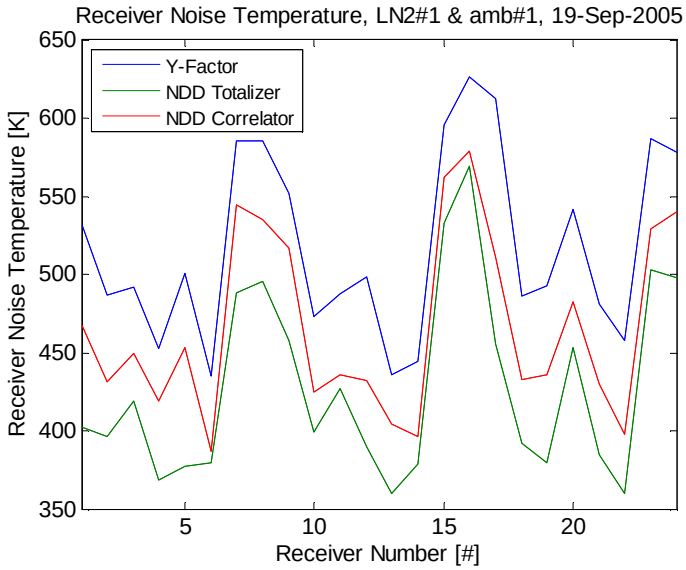

Figure 3.1: Receiver Brightness Temperature Calculated using the 3 Different Calibration Methods

A possible cause of the differences in the methods is the non-linearity of the totalizer measurements due to amplifier compression. These errors can be corrected using the following second order formula

$$P_{t\_corrected} = P_t + cP_t^2 \tag{3.18}$$

Where

P_t = Totalizer Power Threshold

c = Correction Coefficient

$P_{t-correct}$ = Corrected Totalizer Power Threshold

Equation (3.18) is applied to the threshold units as determined using (3.6). The correction coefficient is adjusted for each receiver till the receiver temperatures converge. The adjusted power levels causes convergence between both the totalizer methods. Figure 3.2 shows the results after the application of (3.18).

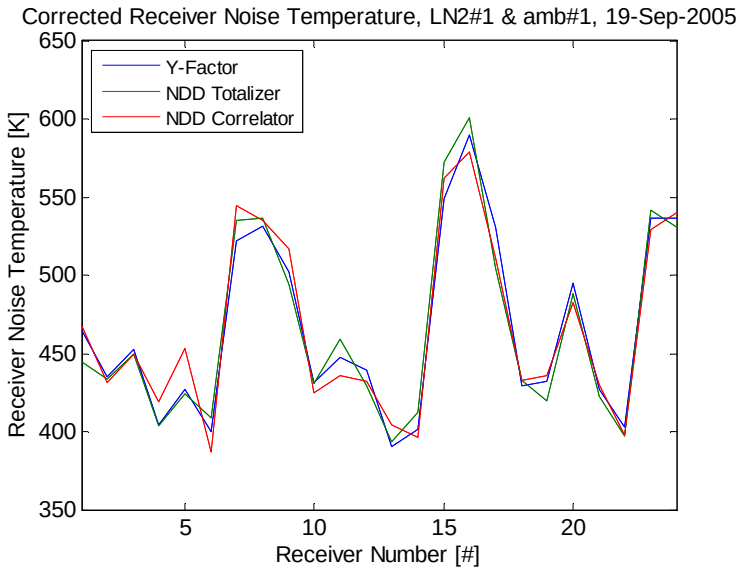

Figure 3.2: Receiver Brightness Temperature Recalculated with Totalizer Linearity Correction

The average magnitude of the correction coefficient 'c' is 0.09, with a standard deviation of 0.02 among the 24 receivers. The corresponding noise diode temperatures calculated with the totalizer linearity correction is shown in Figure 3.3.

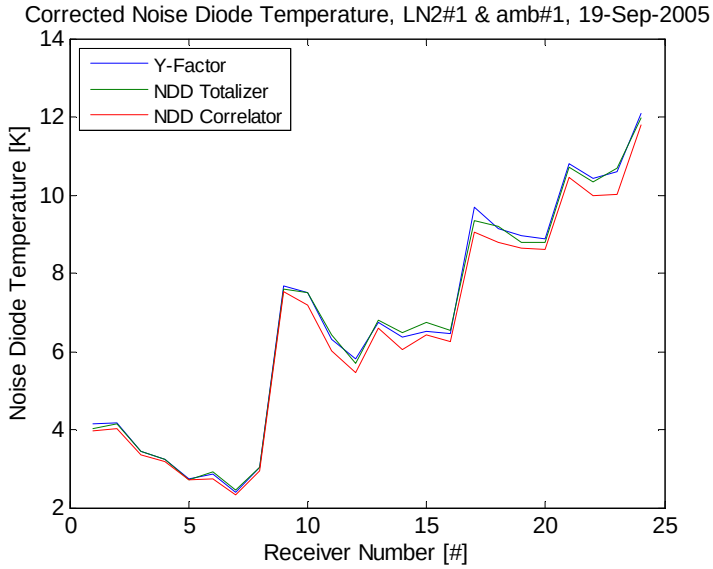

Figure 3.3: Noise Diode Temperatures Calculated with Totalizer Linearity Correction

3.2.2 CALIBRATED RECEIVER AND NOISE DIODE BRIGHTNESS TEMPERATURES

Table 3.1 summarizes the calibrated receiver temperatures with the arrangement of the receivers according to Figure 2.10. The innermost elements are highlighted to show

that the brightness temperatures are higher due to the presence of the isolators placed to reduce coupling between the receivers.

Table 3.1: Receiver Noise Temperatures

Receiver	T_R [K], Arm 1	Receiver	T_R [K], Arm 2	Receiver	T_R [K], Arm 3
1	429.0	**9**	446.8	**17**	483.7
2	433.7	**10**	396.7	**18**	410.8
3	456.7	**11**	422.1	**19**	414.8
4	409.6	**12**	416.5	**20**	472.5
5	425.0	**13**	374.6	**21**	418.2
6	390.8	**14**	384.4	**22**	388.4
7	515.2	**15**	527.0	**23**	505.8
8	525.3	**16**	526.3	**24**	508.3

Table 3.2 shows the associated calibrated noise diode brightness temperatures.

Table 3.2: Noise Diode Brightness Temperatures

Receiver	T_R [K], Arm 1	Receiver	T_R [K], Arm 2	Receiver	T_R [K], Arm 3
1	3.85	**9**	6.91	**17**	8.67
2	4.11	**10**	6.97	**18**	8.33
3	3.38	**11**	5.87	**19**	8.15
4	3.22	**12**	5.36	**20**	8.19
5	2.74	**13**	6.33	**21**	10.00
6	2.83	**14**	5.98	**22**	9.58
7	2.30	**15**	6.13	**23**	9.53
8	2.94	**16**	5.85	**24**	10.97

The noise diode distribution system has the highest magnitudes for Arm 3 followed by Arm 2 and then Arm 1.

3.2.3 CORRELATOR EFFICIENCY

Another comparison of the results can be made utilizing the NDD as calculated with the corrections. If we take the correlator NDD ratio (3.13) and divide it by the totalizer NDD ratio (3.8), the resulting ratio can be used as a measure of the correlator efficiency, η_c

$$\eta_c = \frac{D_{N\_Amb\_c}}{D_{N\_Amb\_t}} = \frac{D_{N\_LN2\_c}}{D_{N\_LN2\_t}} \tag{3.19}$$

Where

η_c	=	Correlator Efficiency
$D_{N\_Amb\_c}, D_{N\_LN2\_c}$	=	Correlator Noise Diode Deflection, Ambient and LN2 Targets
$D_{N\_Amb\_t}, D_{N\_LN2\_t}$	=	Totalizer Noise Diode Deflection, Ambient and LN2 Targets

Table 2.1 shows the correlator efficiency for each receiver in GeoSTAR-D calculated by taking the geometric mean of the values calculated from (3.19). Without the totalizer correction, all the efficiencies are greater than one, clearly in error. The mean efficiency of the correlators after the correction is ~96%.

Table 3.3: Correlator Efficiency for Each Receiver

Receiver	Arm 1	Receiver	Arm 2	Receiver	Arm 3
1	0.950	**9**	0.957	**17**	0.961
2	0.971	**10**	0.966	**18**	0.957
3	0.979	**11**	0.973	**19**	0.959
4	0.963	**12**	0.955	**20**	0.986
5	0.948	**13**	0.953	**21**	0.964
6	0.984	**14**	0.958	**22**	0.967
7	0.939	**15**	0.969	**23**	0.957
8	0.967	**16**	0.981	**24**	0.972

3.3 ANECHOIC CHAMBER TESTS

GeoSTAR-D was fully integrated and tested end-to-end at the NASA Goddard Space Flight Center (GSFC) Building 19 anechoic chamber from 09/26/2005 to 10/01/2005. The facility is a dual range, shaped in an 'L'. Traditional far field range measurements at low frequencies can be made along one length of the L. Along the other length is a Scientific Atlanta 5706 compact range. Figure 3.4 shows the instrument mounted facing the reflector.

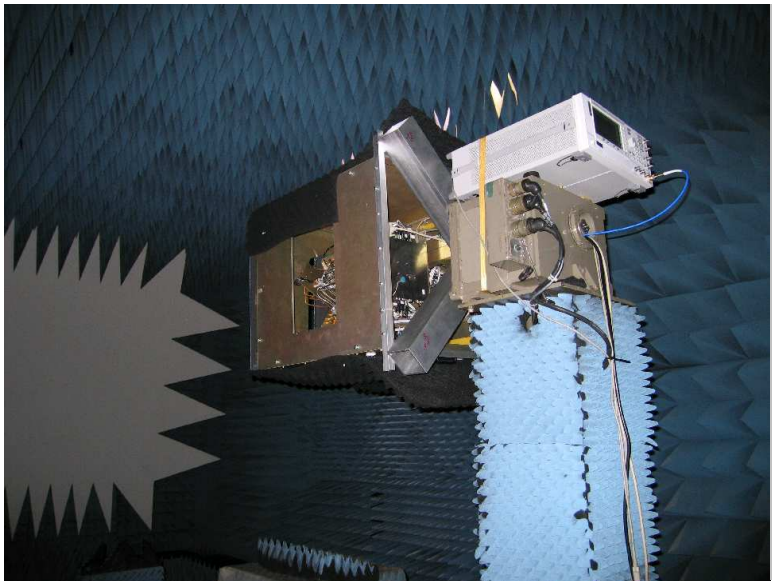

Figure 3.4: GeoSTAR-D Mounted and Pointed at the Compact Range Reflector

The pedestal mount on which GeoSTAR-D is attached has 4 degrees of freedom, 3 of which are utilized while making measurements – azimuth, polarization and range (toward/away from the main reflector). The elevation axis was zeroed and set using a carpenter's level and remained unchanged throughout the measurements. Figure 3.5 shows the typical measurement configuration with the noise diode source in the foreground. The source mount allows for rotation in antenna polarization. Care was taken to ensure that spurious standing waves would not be generated by covering any exposed metallic areas with absorber material.

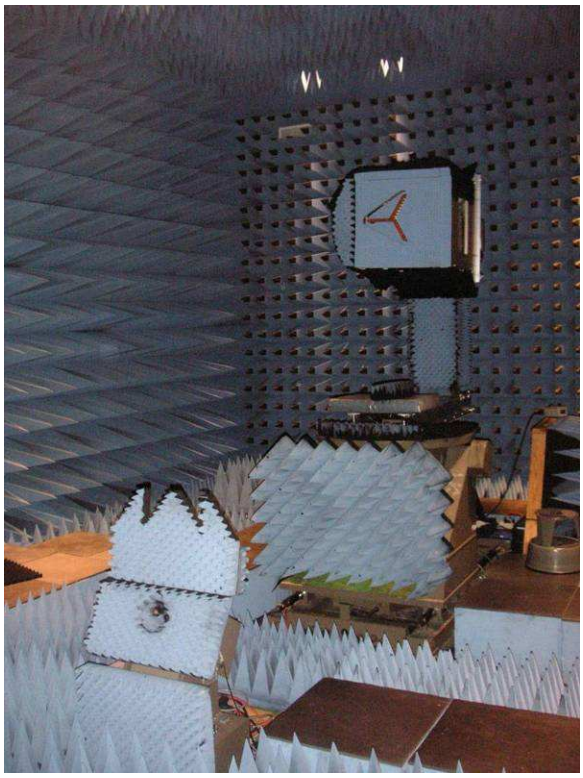

Figure 3.5: GeoSTAR-D in the Background, Noise Diode Source in the Foreground

Figure 2.1 shows the instrument with the author to depict scale.

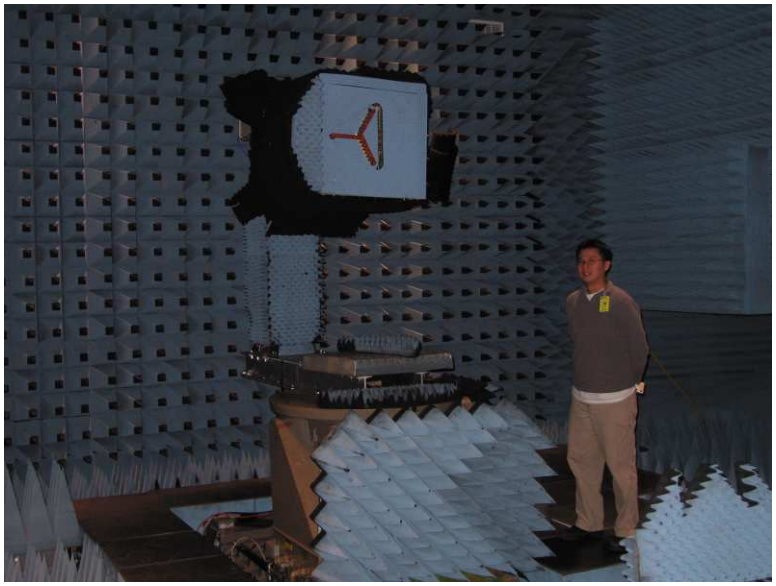

Figure 3.6: GeoSTAR-D at the GSFC Compact Range, 90^0 Polarization, with Author

3.3.1 TEST OBJECTIVES

The primary chamber test objectives were three-fold. First, this would be the first full end to end test of the system taking data in an operational mode. The collected data would be processed by the retrieval software developed jointly at JPL and the University of Michigan to evaluate any future data processing requirements as well as confirm the current software capabilities. Secondly, the results would be used to validate the theoretical antenna pattern model of the full array structure and the resulting interference fringes. Recall that there are two alternatives proposed for the generation of the antenna pattern, the theoretical model or measurements of the full array. If it can be shown that the theoretical model properly simulates the full array with acceptable error levels, then careful full array measurements that are prohibitively costly for the space borne instrument need not be performed. Finally the measurements would provide an external phase calibration of the system that would be used in generation of images when the instrument was deployed in the field.

An important secondary objective pertains to the formulation of the experimental G-matrix [32, 63], a function that relates the brightness temperatures to the visibilities. Due to limited time for measurements, even with the reduced scale demonstrator, spatial Nyquist sampling could not be performed. The interference fringe measurements are examined closely to determine if there is information that can be used to aid in the theoretical formulation of the G-matrix.

3.3.2 THEORETICAL ANTENNA PATTERN MODEL

The theoretical antenna pattern model for the GeoSTAR-D parabolic Potter horn is calculated based on an ideal spherical wave expansion using code provided by the

designer, Bill Imbriale at JPL. Figure 3.7 shows the theoretical vertical and horizontal polarization antenna patterns of the parabolic Potter horn, for the half space in front of the antenna. The antenna pattern is symmetric off bore sight in the model. In addition to the low mutual coupling, the antenna design also exhibits a continued roll off in the pattern, and very low side lobe levels.

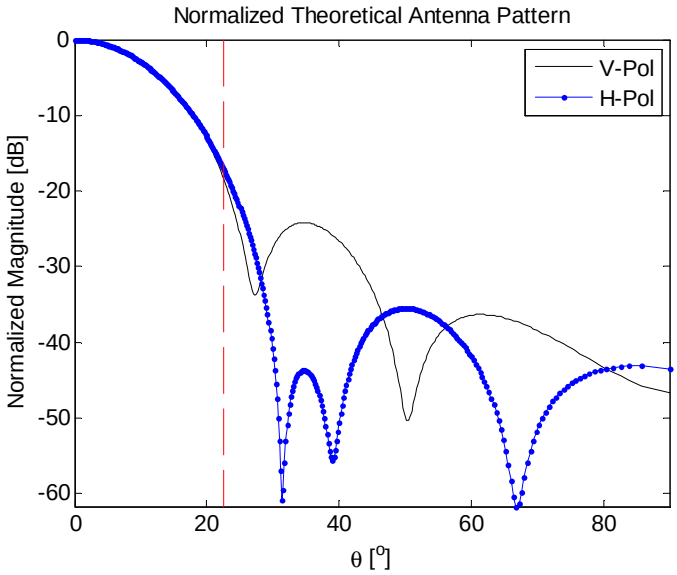

Figure 3.7: Horizontal and Vertical Plane Antenna Patterns

A vertical line is drawn at $\pm 22.5^0$, showing the cutoff at which the beam efficiency is approximately 99.5%. This cutoff shows the maximum limit for which fine range measurements will be made. In particular, the limit most crucial will be the angular extent of the Earth disk from GEO ($\sim 7.6^0$).

3.3.3 MEASUREMENTS PERFORMED

Initial measurements were performed to ensure the proper operation of the entire system and synchronization with the chamber control software. A full summary of the measurements made, and the problems encountered can be found in Appendix A – the following is a brief list of the measurements made:

- Polarization scans
- Direct source illumination
- Coarse azimuth scans
- Source ‘Lo-power’ and ‘Hi-power’ scans
- Full polarization and azimuth scan

The scanning of the system was configured for ‘discrete’ sampling where the instrument stops at the sampling point so that measurements can be taken. Due to the settling time from mechanical movement and the fine resolution of some measurements, the longest measurement set ran over ten hours long and was made overnight. Data were taken continuously, however samples taken while the instrument or the target source was moving was not used. The rationale for utilizing this scheme was to avoid the decorrelation effects of a continuous scheme, exacerbated by the multiple samples required for each realization of a data point (8 local oscillator phases, 4 noise diode states).

3.4 ANTENNA PATTERN COMPARISON

The measured antenna patterns can be derived from both the correlator and totalizer measurements. The antenna patterns shown are derived by normalizing the power to the boresight levels. While this is not an absolute measurement, it will suffice for GeoSTAR since all we are interested in are relative pattern error, especially within the region of the Earth disk. Figure 3.8 shows the results from experiment 3, where 2 principal plane cuts were made (0^0 and 90^0).

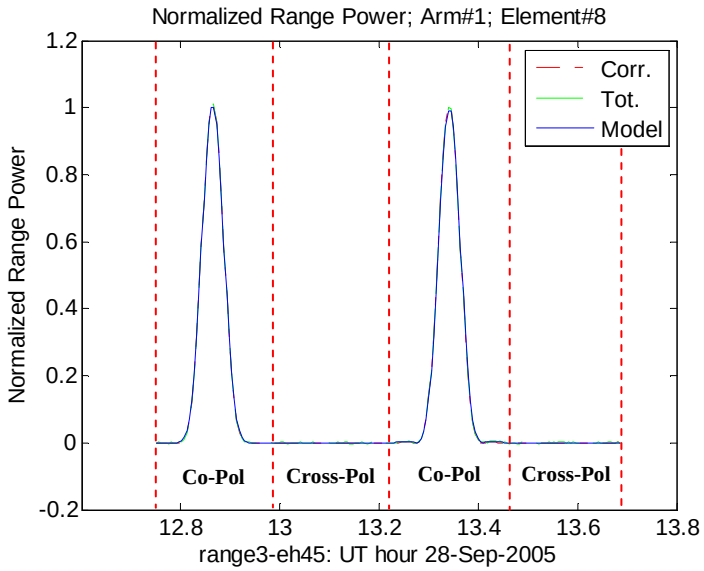

Figure 3.8: Normalized Range Power Compared to Theoretical Antenna Pattern Model

Co-pol and cross-pol measurements were made by rotating the range noise source, which explains the low power levels after the peaks in the pattern. It is apparent that the errors in the antenna pattern are small and barely noticeable in a linear scale. Figure 3.9 shows the same results in a decibel scale. The side lobe levels are well characterized by the model and similar results are obtained with all the other antenna elements [59].

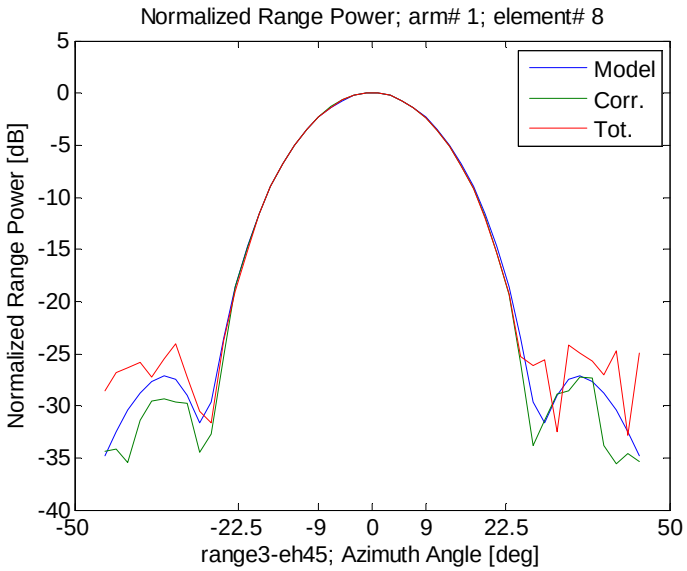

Figure 3.9: Normalized Range Power Compared to Theoretical Antenna Pattern Model dB Scale

Table 3.4 summarizes the measured antenna pattern errors when compared with the theoretical model for both the correlators and the totalizers from Experiment 18, which had the highest azimuthal resolution (1^0). The correlation of the results between the methods gives us high confidence in the quality of both methods.

Table 3.4: Antenna Pattern Errors Calculated Using Both Measurement Methods

Antenna Pattern Error as Measured by Correlators [%]

Element [#]	1	2	3	4	5	6	7	8
Arm 1	0.69	0.90	0.73	0.61	0.54	0.36	0.52	0.44
Arm 2	0.86	0.72	0.27	0.19	0.80	0.71	0.63	1.00
Arm 3	0.56	0.28	0.42	0.24	0.46	0.61	0.40	0.32

Antenna Pattern Error as Measured by Totalizers [%]

Element [#]	1	2	3	4	5	6	7	8
Arm 1	0.72	0.98	0.77	0.71	0.57	0.33	0.49	0.41
Arm 2	0.83	0.70	0.23	0.27	0.80	0.70	0.66	1.00
Arm 3	0.50	0.30	0.39	0.26	0.50	0.66	0.46	0.35

The element #'s are counted from the outside of the array to the inner elements, so that the closest elements to each other are elements 8 in each arm. The mean errors are on the order of 0.6% with maximum errors at 1.0%. Note that these errors are calculated by comparing the difference in the pattern to the normalized value. The errors are within less the half of the requirements the specifications that were outlined in Chapter 2. Another method to visualize the pattern error magnitudes is shown in Figure 3.10, where the multiple polarization cuts are combined to generate an error map. The following results were generated using the correlator measurements and the color scale is chosen to saturate when errors are larger than 3%.

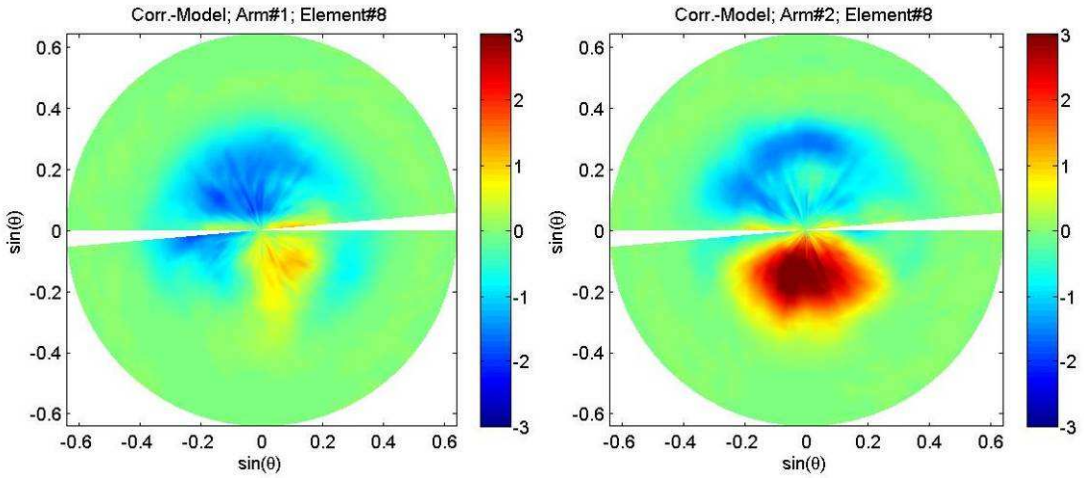

Figure 3.10: % Error Map of Two Antennas at the Center of the Array [%]

Two antennas at the center of the array are selected, from arm #1 and arm #2. For both antennas, the errors appear to be biased in different directions, which rules out an overall gross pointing error for the entire instrument as the only error. This error is most likely due to the pointing of the individual antennas themselves. In this example, the error in element #8 in arm #2 is significantly larger than that in most of the other antennas. In addition, errors appear to be largest within the main beam, where we will be observing the Earth disk.

Figure 3.11 shows the error map generated for each element in the entire array. The inset shows the actual face of the array.

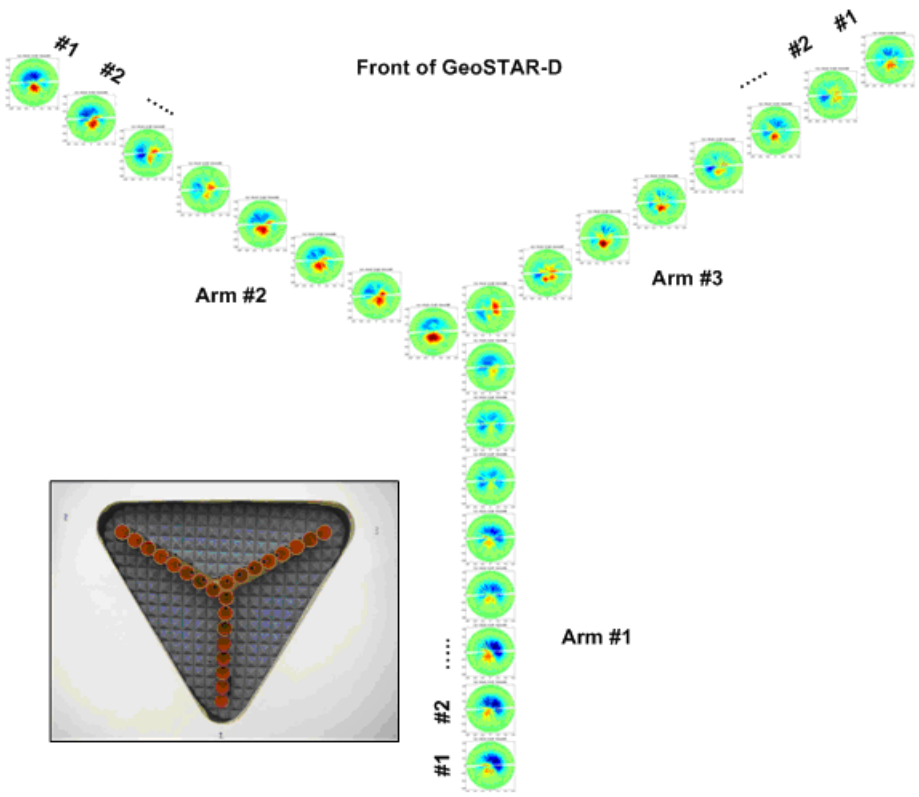

Figure 3.11: Error Map of the Entire Array with an Image of the Face of the Actual Array

The errors for arm #1 seem to be quite well behaved. Errors are smaller at the center of the array and increase at the ends of the arm, and all point downwards and offset to the left at the ends of the array. This suggests that there may be a systematic error, perhaps bending in arm #1 inwards at the end of the array. A similar trend can be seen in arm #2, however with a minimum at the middle elements and large errors at the ends. Errors in arm #3 appear to be more random in nature, though some may be explained by flexing of the arm downwards.

The antenna pattern measurements on the antenna range show good quality, and the relative magnitudes compared with boresight are well within the requirements of the eventual flight system. In addition, with some analysis of the polarization measurements, we are able to ascertain to some extent the pointing errors of the individual antennas. The pointing error of each antenna can be found, with some contribution from the

systematic flexing of the arms. While best practices were followed during the mechanical integration of the GeoSTAR-D, tighter tolerances would reduce the level of these errors significantly below our requirements.

3.4.1 ANTENNA ALIGNMENT VERIFICATION

The following analysis was performed by Tanner [64], and is presented here to complete the antenna pointing problem. In 2007, during the integration of a Dicke radiometer to perform the total power measurement for the GeoSTAR-D, careful mechanical alignment measurements of the array antennas were performed. The alignment was performed by placing a reflecting mirror within each antenna and measuring the deflection of a laser pointer reflection (Figure 3.12). Through simple trigonometric identities, the vertical and horizontal pointing error of each antenna can be determined.

Figure 3.12: (Left) Reflecting Mirror in Antenna and (Right) Retro-Reflection Measurements [64]

To ascertain the antenna range offset, the apparent center of each of the elemental antenna patterns was calculated using the chamber measurements. Figure 3.13 shows the offset comparison in the horizontal and vertical direction between the anechoic chamber and retro-laser experiments. Even with the measurements performed more than 1½ years

apart, the pointing errors track very well. This result shows that the physical pointing errors correspond very well with those obtained in the anechoic chamber.

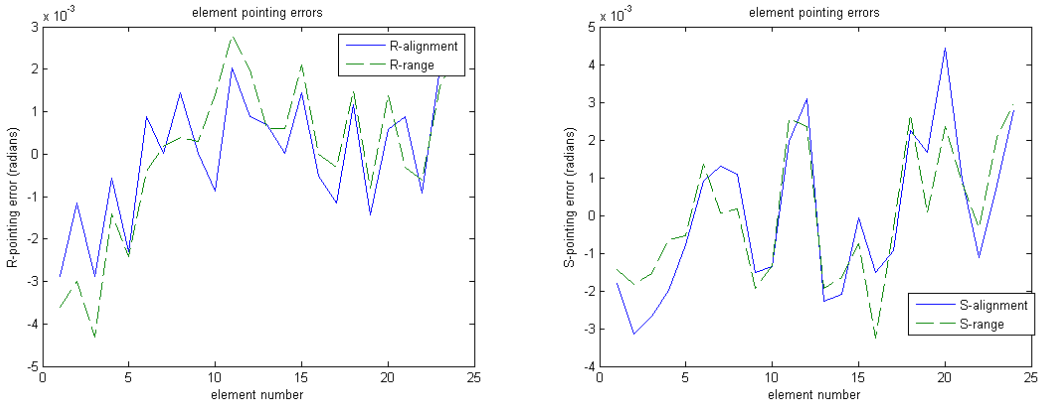

Figure 3.13: GeoSTAR-D (Left) Horizontal and (Right) Vertical Antenna Offset Comparison [64]

3.5 ARRAY PHASE CALIBRATION

The array phase calibration was extracted from the anechoic chamber data using procedures outlined in Section 3.1.5. The phase calibration, when combined with the magnitude calibration, generates fully calibrated visibilities in the far-field for the instrument. Note that the absolute magnitude of the external source is not utilized during the generation of the phase calibration, as only the phase information is used. The phase information is determined for a single boresight point only. The boresight calibration is performed for when the orientation of the Y-array follows that of nominal operation with an array arm pointing downwards (see Figure 3.11).

3.5.1 BORESIGHT ALIGNMENT IMPERFECTIONS

Figure 3.14 shows the measured phase of the signal between antenna 24 and antennas 1 to 4 at various polarization rotation angles in the anechoic chamber. The measurement at 0^0 polarization represents the boresight calibration point, with the instrument in the nominal operation alignment. Mechanically, GeoSTAR-D was attached

to a rotator with significant weight at the end of a boom (see Figure 3.4). Flexing of the attachment could have caused the face of the instrument to deflect depending on the polarization rotation, especially if the phase front of the demonstrator was not exactly perpendicular.

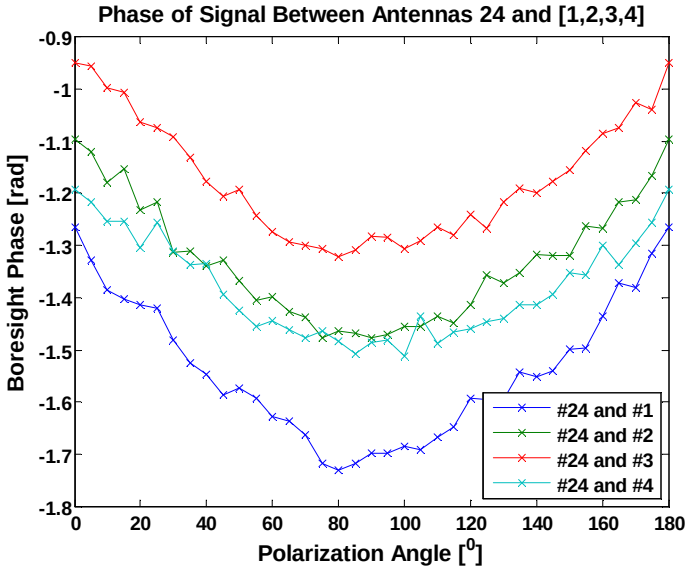

Figure 3.14: Phase of Signal Between Antenna 24 and Antennas 1-4 for the Boresight Pixel at Various Polarization Rotation Angles

3.5.2 ADDITIONAL PHASE INFORMATION

Figure 3.15 shows the calibrated phase pattern for the pair of antennas #24 and #8 for the entire measured field of view. The white hexagon outlines the retrieved field of view, and the white point is the center boresight pixel from which the array calibration is performed. Several features are notable to this image. The phase information is well retrieved within the area for which the antenna pattern has not suppressed the measurement below the noise floor, as opposed to the edge of the measurements where the phasing is arbitrary. While the antenna pair is only separated vertically, the phase front is not exactly perpendicular to separation. This indicates that the physical positions of these phase centers are not only vertically separated.

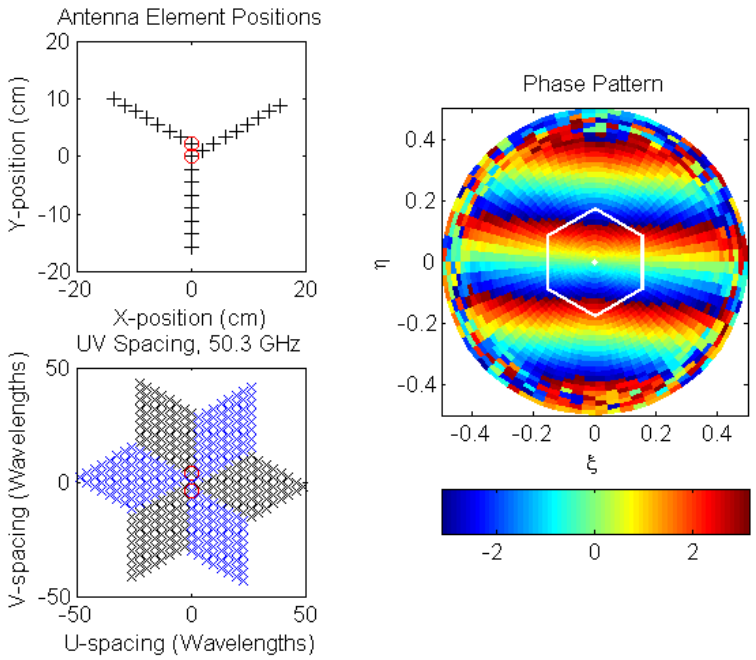

Figure 3.15: Measured Phase Pattern of the External Source

The comparison of these phase imperfections will provide additional information that can be used to improve the reconstruction algorithms to be discussed shortly.

3.6 IMAGE RECONSTRUCTION ALGORITHM

The original G-Matrix combines the effects of both the sampling and the antenna pattern [32, 63] so that direct measurements from the anechoic chamber can be used to invert the visibilities. The following section outlines an image reconstruction algorithm that combines the theoretical instrument models with the anechoic chamber results so that imperfections in the array can be accounted for without a full sampling of the G-Matrix.

3.6.1 UNDER-SAMPLED DATA

Measurement of the full G-Matrix in the anechoic chamber could not be performed due to time constraints, resulting in under-sampled data. The Nyquist sampling rate in

the image domain for the interference fringe generated by the longest baseline can be calculated using the following

$$\Delta\theta_N \approx \sin^{-1}\left(\frac{1}{2\sqrt{3}[d_\lambda(N_{EL}-1/3)]}\right) \tag{3.20}$$

Where

$\Delta\theta_N$ = Nyquist Sampling Rate for Largest Interference Fringe [rad]

For the demonstrator array, this value results in a sampling every 0.01 radians (0.57^0). The chamber measurements would then have to be sampled with a minimum of 31 pixels across the field of view. Figure 3.16 shows the differences in the theoretical and anechoic chamber sampling grids for the reconstructed field of view (outlined in red).

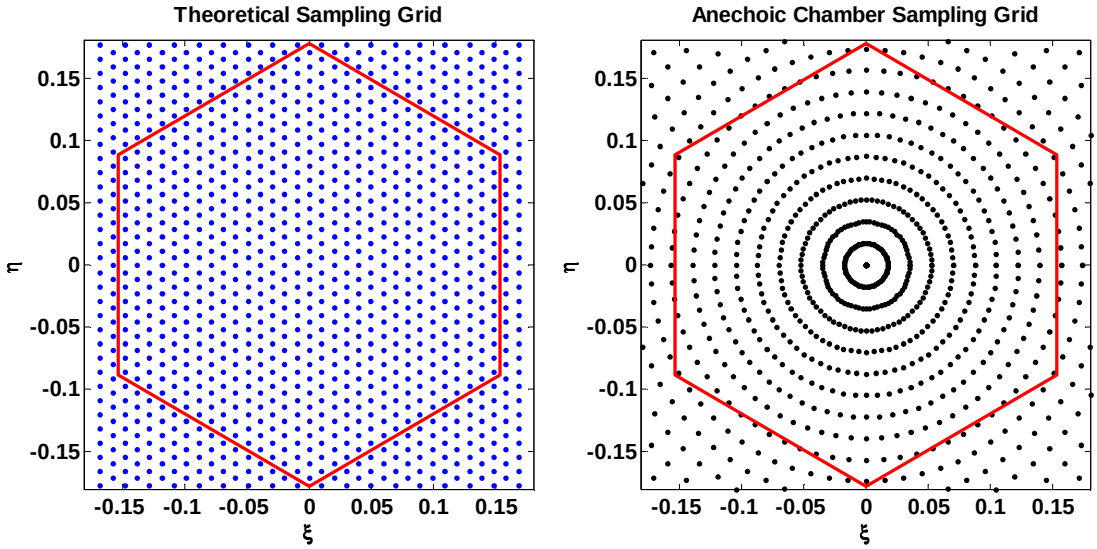

Figure 3.16: (Left) Theoretical Nyquist Sampling vs. (Right) Anechoic Chamber Sampling

The finest anechoic chamber measurements were made with 1^0 azimuth steps and 5^0 polarization steps. The theoretical sampling grid is generated with equal sampling in the directional cosine coordinates. The polar radiating circular nature of the measurement in the anechoic chamber is consistent with measurements made with equal spacing in degrees rather than in directional cosine coordinates. Note that away from boresight, the samples in the anechoic chamber become sparser.

Figure 3.17 shows a simulation of the real part of an over sampled theoretical interference pattern for the largest baseline with the associated position of the antenna pair and the sampling in the visibility domain. The imaginary part will be 90^0 out of phase. Two samples are called out in the visibility domain to show the Hermitian symmetry, even though only one measurement is made. The two dimensional interference pattern is regular with magnitude variation only in the direction defined by the separation of the antenna pair. The magnitude perpendicular to that direction is constant.

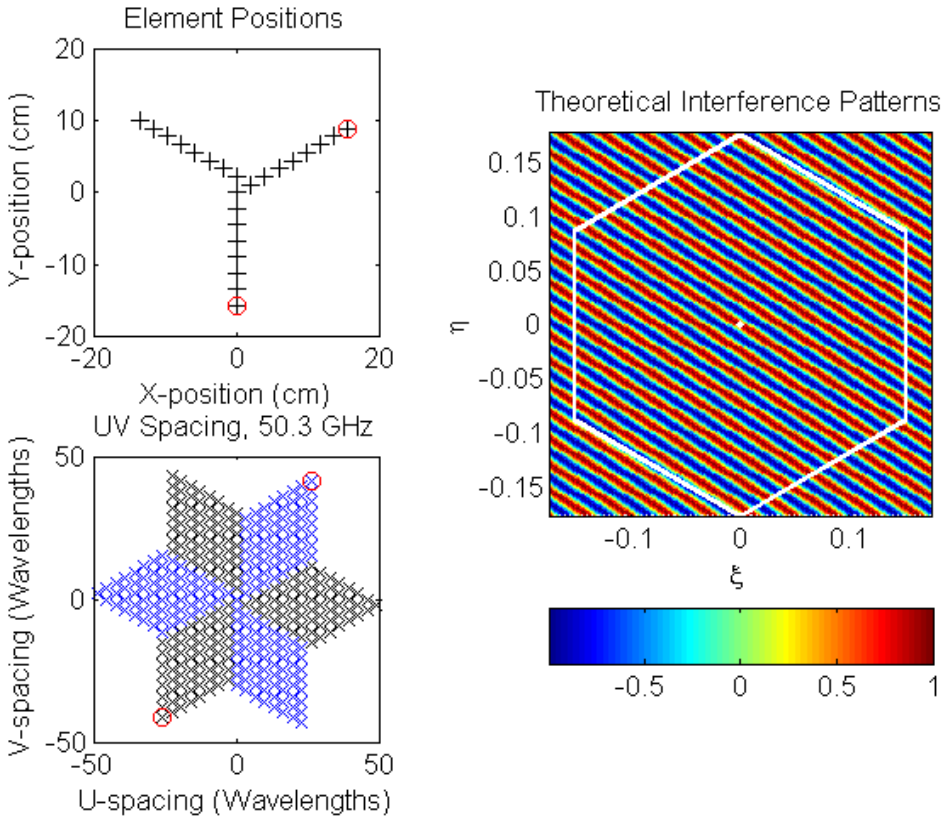

Figure 3.17: Real Part of the Interference Pattern for Largest Baseline with Associated Antenna Position Pair and Spatial Frequency Component Including Hermitian Conjugate (Blue)

Figure 3.18 shows the associated theoretical under sampled interference pattern.

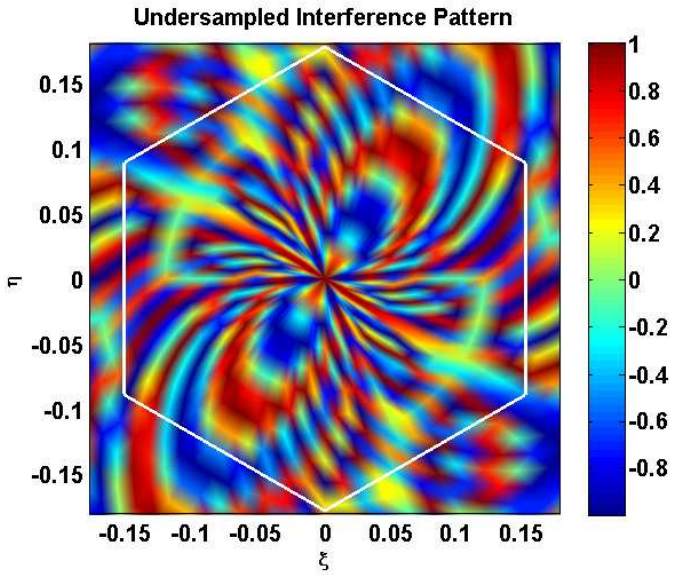

Figure 3.18: Simulated Under Sampled Interference Pattern of Largest Baseline

The well formed regular interference pattern is no longer recognizable; instead the pattern formed shows beating effects from the irregular sampling. Clearly the measured interference patterns from the anechoic chamber cannot directly be used to formulate a usable G-matrix due to the improper sampling.

3.6.2 WELL SAMPLED BASELINES

While the finest anechoic chamber sampling rate does not satisfy the Nyquist criterion at the largest baselines, this criterion is not violated for the smaller baselines. One of the innermost baselines is presented, that formed by antennas 24 and 8. In addition to the nominal processing, the boresight phase correction is also applied to the measurements and the theoretical interference patterns are weighted by ideal antenna patterns with ideal pointing. Figure 3.19 shows the real component of the interference pattern generated from antenna elements 24 and 8. The measured correlation magnitude is normalized to the maximum value in the full measurement set to ensure that the peak is

captured. With the boresight phase correction, the theoretical interference pattern line up well with the phase calibrated measurement.

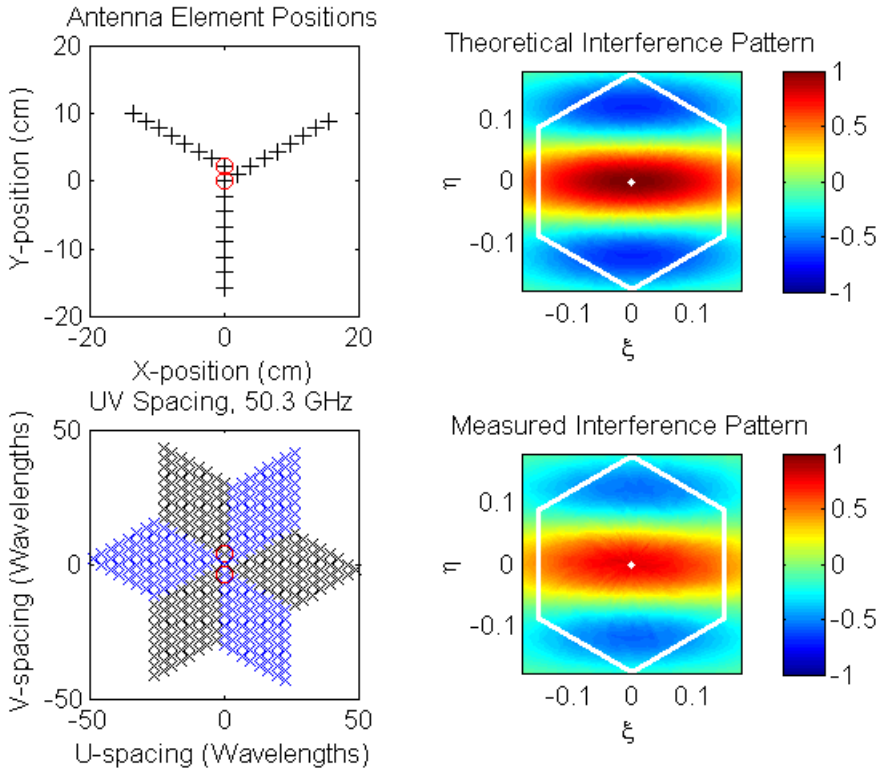

Figure 3.19: Interference Pattern Generated From Antenna Elements 24 and 8

3.6.3 BORESIGHT CENTER CORRECTION FROM THEORETICAL PATTERNS

The residual difference between the measured and corrected theoretical interference patterns is minimal, but can still be used to calibrate pointing errors of the instrument. The theoretical fringes are generated assuming that the pointing of the instrument is perfect at boresight. Deviations of the measurement and from the theory will give a measure of the boresight pointing error of the instrument as a whole. Dividing the measured pattern by the theoretical pattern, the residual phase is an additional correction factor that can be applied to the calibration. Figure 3.14 already shows that the phase of

the boresight pixel varies with the polarization angle. Figure 3.20 shows the residual phase of the antenna elements 24 and 8 (same pair as Figure 3.19).

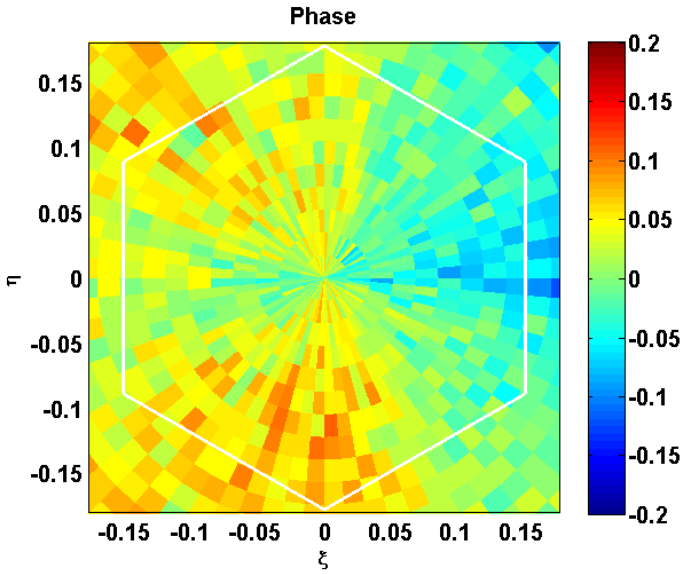

Figure 3.20: Residual Phase Error Generated From Antenna Elements 24 and 8

The residual errors in this image are relatively small in magnitude and most likely due to the non-planar phase front in the compact range itself, in addition to the pointing error.

To extract the pointing error, two different sets of measurements are examined, the antenna pairs that are only separated in a vertical direction and those separated in a horizontal direction. The residual phase error correction for η is generated by taking the mean of the error in the η direction for the elements separated in the vertical. A similar correction is performed with respect to ξ. The resulting boresight deviation is $\eta_C = 0.026$ and $\xi_C = -0.006$.

3.6.4 THEORETICAL G-MATRIX FORMULATION

A discrete version of (2.4) which relates the modified brightness temperature to the visibilities can be represented in matrix form as

$$V = GT_{MB} \tag{3.21}$$

Where

G = G-Matrix

The G-Matrix defined here with the modified brightness temperature does not include the effects of the antenna patterns but instead is simple the sampling due to the Fourier like transform, $e^{-j2\pi(u_{ij}\xi+v_{ij}\eta)}$. Within the limits of this theoretical approach, the inverse formulation G^{-1} is simply $e^{j2\pi(u_{ij}\xi+v_{ij}\eta)}$. If we represent the relationship between the T_B and T_{MB} by the matrix F (mainly the antenna pattern effects), (3.21) can be rewritten as [58, 65]

$$V = GFT_B \tag{3.22}$$

The estimated brightness temperature $\hat{T}_B$ image can then be retrieved using

$$\hat{T}_B = F^{-1}G^{-1}V \tag{3.23}$$

(3.23) represents the ideal theoretical formulation of the retrieval algorithm where both G^{-1} and F^{-1} are determined using models and when combined with (3.17) gives us the relationship between the measurements and the estimated brightness temperatures.

Section 3.4 shows that the antenna patterns errors are within tolerance giving us confidence in the usage of the theoretical formulation of F^{-1}. The accuracy of G^{-1} is improved by the secondary boresight correction as outlined in Section 3.6.3.

3.7 SUMMARY

A calibration methodology has been outlined for GeoSTAR-D that performs the brightness temperature magnitude calibration by using a traditional two-point calibration. The phase calibration is completed using measurements taken of a correlated source in a

compact range positioned at boresight. An image retrieval algorithm is presented that utilizes both these measurements and the various theoretical models of the antenna patterns and the visibility sampling.

The theoretical antenna pattern is verified using normalized measurements of both the correlator and totalizer measurements. Both methods produce results of similar magnitude and are well behaved, giving us confidence in both the measurement and the methodology. The average error within 22.5^0 of boresight is within the tolerances that were outlined in Chapter 2, by more than a factor of 2. However, the maximum error, especially within the Earth disk extent, has magnitudes larger than specifications.

By combining the various polarization cuts of each antenna, an error map can be generated which gives us a visual method to determine systematic errors. An analytical look at the results is verified by careful physical measurements performed nearly a year and a half later. Large scale pointing errors are easily mitigated with a more robust structure design and with tighter mechanical tolerances. These results are highly promising as they indicate that the theoretical model produces results that are well within our current specifications. These errors can be further reduced by improved mechanical design of the instrument.

The external phase calibration is performed utilizing a pixel at boresight while the instrument is in the nominal operating geometry. Variations in the 'boresight' phase during polarization rotation measurements are most likely due to physical geometric errors in the instrument setup and alignment. A secondary calibration to the expected theoretical results will decrease the boresight pointing error. Chamber errors and effects are notable, especially of the non-planar phase front, and possible mechanical flexing of

the instrument mount. These are embedded in the calibration directly, even with the best measurement practices.

The measurements in the anechoic chamber cannot be used directly in the image reconstruction algorithm due to the under sampling of the interference fringes. Instead, an image reconstruction algorithm is formed that relies mainly on the theoretical models of both the antenna and the visibility sampling, with corrections based on anechoic chamber measurements. While images with the proper contrast are easily reconstructed with the outlined algorithm, determining the absolute differences between $\hat{T}_B$ and T_B is difficult. Evaluation of the theoretical image reconstruction methods can only be performed with known and calibrated scenes. This effort and the results will be outlined in Chapter 4.

CHAPTER 4

GEOSTAR-D EARTH DISK MEASUREMENTS

4.1 SIMULATING GEOSTAR MEASUREMENTS

Upon successful functional testing and calibration in the anechoic chamber, GeoSTAR-D performed measurements at JPL and generated the first calibrated images. Figure 4.1 shows the first calibrated image of a hillside at 50.3 GHz with reference photograph [59, 66].

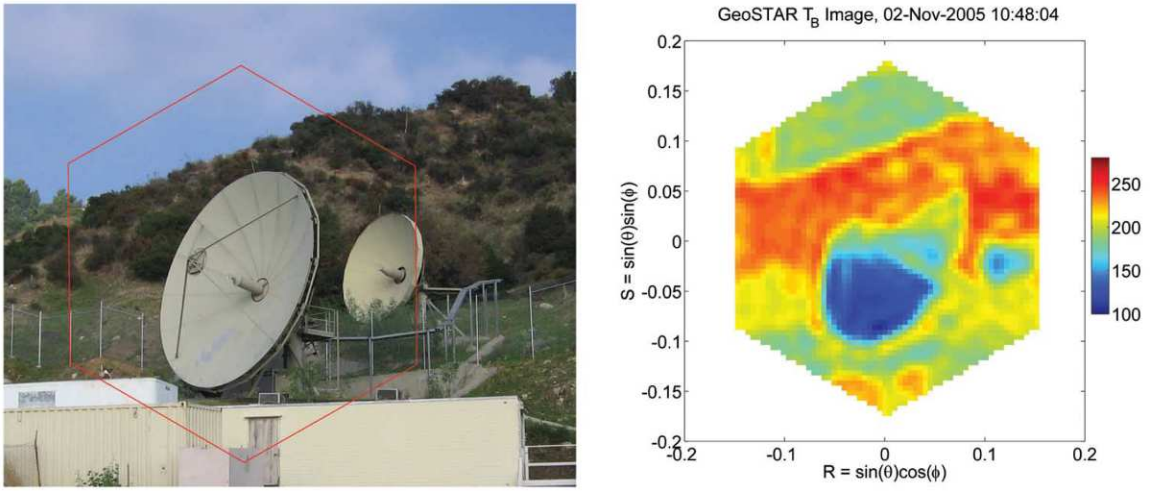

Figure 4.1: GeoSTAR-D First Calibrated Images of a Hillside at JPL [41]

The lower temperature area in the middle of the brightness temperature image represents the reflected value of the colder sky in the dish antenna. Difficulties arise when evaluating the performance of the instrument with images such as these since extensive knowledge of the measured scene is required for proper comparison. To a first order, GeoSTAR-D appears to be performing well as the images produced have the right contrast; however a more controlled test scene is required for true evaluation of the

instrument and the associated post-processing algorithms. An ideal control scene will imitate measurements from GEO in terms of the geometry, contrast on the Earth disk and background brightness.

Generating this control scene required the engineering of an Earth disk target, circular shaped to mimic the geometry of the Earth from GEO. Independent heating zones on the target will generate the required contrast for the continental boundaries. Thermistors embedded throughout the target to allow for monitoring of the physical temperature of the target and comparison to the retrieved image temperatures. Replicating the cold space background will not be possible due to the effects of the atmosphere at 50 GHz. The sky with a suitable measurements and models to generate the atmospheric profile is an acceptable proxy. Figure 4.2 shows the experimental setup at the JPL mesa antenna range. The difference between GeoSTAR-D and GeoSTAR images will be that of pixel resolution as the demonstrator image has significantly fewer pixels.

Figure 4.2: Experimental Setup at the JPL Mesa Outdoor Antenna Range. The Earth disk target is highlighted in the upper left and GeoSTAR-D in the bottom right.

The following sections outline the engineering of the Earth disk target, the tests performed, the generation of the supporting models and the results obtained.

4.2 THE EARTH DISK TARGET

The Earth disk target is created to allow for GeoSTAR type measurements to be performed with GeoSTAR-D, at a reduced scale. As the target is meant for deployment outdoors, the target is also designed to be light weight and portable. The target is a 12 foot diameter disk constructed from foam insulating sheets that cover microwave absorber. These light weight sheets provide excellent structural stability in addition to insulating the microwave absorber. The materials selected are transparent at 50 GHz such that the surface emissivity of the target is approximately that of the microwave absorber, i.e. 1. Figure 2.1 shows the folded target attached to the antenna range boom prior to deployment. The white surface is 1 cm expanded polystyrene for additional thermal insulation.

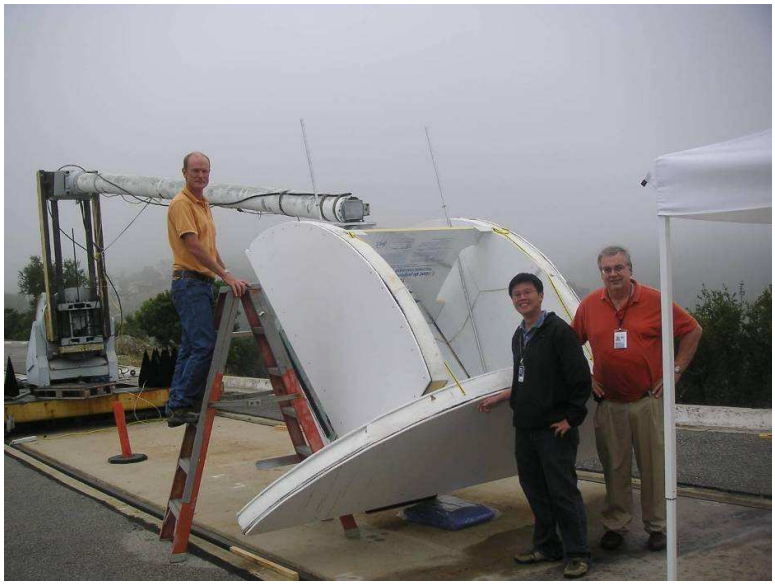

Figure 4.3: Earth Disk Target Folded and Attached to Boom Arm Prior to Deployment

The target also contains 2 independent heating regions, 22 thermistors distributed throughout and a microwave beacon for near-field phase correction.

4.2.1 INDEPENDENT HEATER REGIONS

To create contrast on the target to mimic the difference between land and ocean brightness temperatures, two separate heating zones of different sizes are created. The physical dimensions of these areas are 2x2 ft and 4x4 ft, with convective air heating within the zones. Figure 4.4 shows the target deployed with the two zones highlighted.

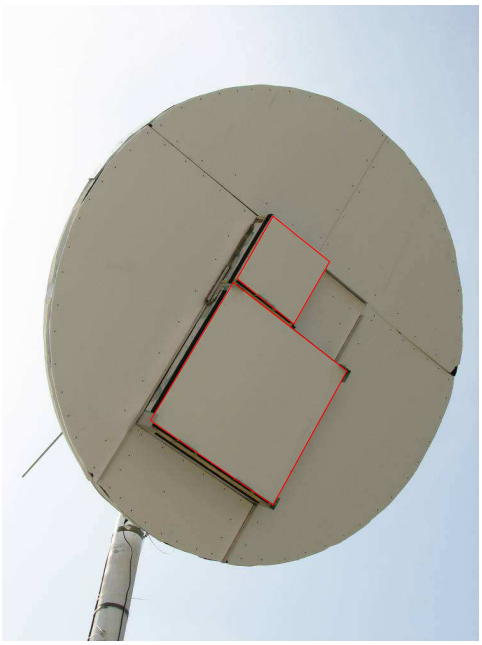

Figure 4.4: Earth Disk Target with the Two Independent Heating Zones Highlighted in Red

The 2x2 ft zone is placed in the upper hemisphere and the 4x4 ft zone in the lower hemisphere. These zones may be heated up independently to a physical temperature of approximately 55^0 C (~323 K).

4.2.2 EMBEDDED THERMISTORS

During the construction of the Earth disk target, a total of 21 thermistors were embedded within the absorber material across the target. 4 thermistors were placed

within the 2x2 ft heated region, 8 thermistors within the 4x4 ft heated region and 9 thermistors within the unheated region. Figure 4.5 shows the thermistors locations with the heated regions outlined. The thermistors will provide information that can be used for comparison to the measured brightness temperatures.

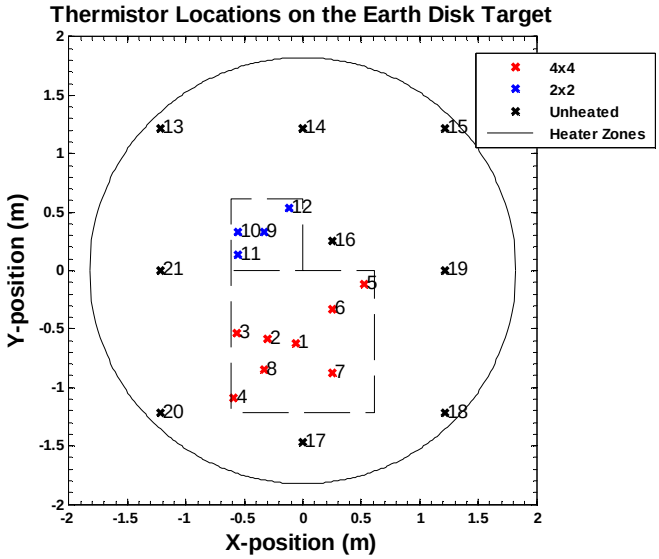

Figure 4.5: Thermistor Locations on the Earth Disk Target

4.2.3 TARGET BEACON

A noise diode source is place within the center of the target to act as a phase reference for near-field phase correction. The beacon has a period of ~240 s and remained switched on for ~26 s for a ~94% target duty cycle). The antenna attached to the beacon is the same parabolic Potter horn used in GeoSTAR-D.

4.3 NEAR FIELD CORRECTION

The far field of the GeoSTAR-D instrument is larger than 40 m, so measurements closer than that distance must be corrected for the near-field effects. The largest source of error for measurements made in the near field is the phase error due to the still

spherical expansion. In the region between 10m and 40m, amplitude effects account for less than 1% of the error [67]. The simplest method to calibrate the phase difference is to utilize a single pixel at the target range as a focus point for which the near-field errors can be corrected [68]. A pixel at boresight is the best choice because it reduces the phase errors the most throughout the image [67]. To this end, the beacon source at the center of the target provides for a suitable phase reference. The effects of this correction have been demonstrated in a laboratory setting successfully. Figure 4.6 shows the results of the near field correction, imaging a person in the laboratory holding an insulated mug. The insulation is transparent to the microwave frequency of measurement.

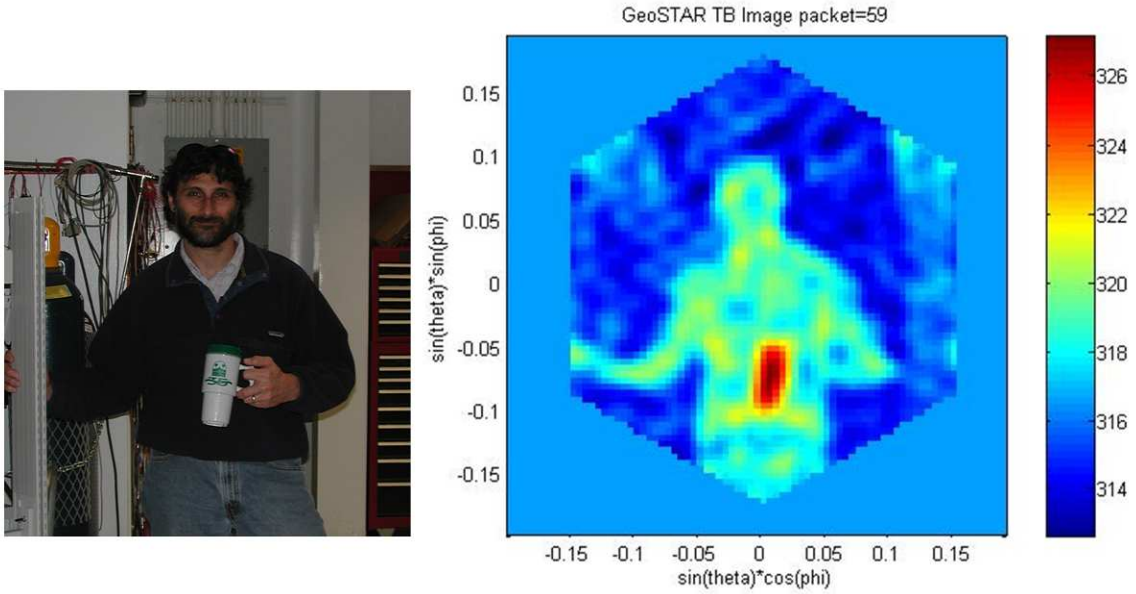

Figure 4.6: GeoSTAR-D Near Field Calibrated Image of a Person Holding a Hot Cup of Coffee [66]

This phase correction is performed in addition to the external phase calibration in the anechoic chamber that calibrates the inter-element antenna phases to the noise diode magnitude calibration.

$$V_{ij}^{FF} = V_{ij}^{NF} e^{j\phi_{NFCij}} \tag{4.1}$$

Where

$\hat{V}_{ij}^{FF}$ = Corrected Far Field Visibility [K]

V_{ij}^{NF} = Near Field Visibility [K]

ϕ_{NFCij} = Measured Near Field Correction Phase [rad]

4.4 JPL MESA TESTS

Deployment of GeoSTAR-D at the JPL mesa antenna range was performed over two different dates. The initial deployment from June 5th 2006 to June 8th 2006 performed the preliminary measurements to determine the interplay between all the different systems. In particular, the Earth disk target devices (heater control, thermistors data logger, calibration beacon) had to be full tested in the field. The following is a brief summary of the initial tests performed:

- Positional alignment of GeoSTAR-D to the target
- Fine tuning of the calibration beacon power levels
- Target measurement with heater zones varying
- 'Tip curve' measurement of the atmosphere
- Polarization rotation measurements
- Aliasing demonstration

These tests were performed during the day time and both the target and the instrument stowed at the end of the day. Upon completion of these tests, a cursory examination of the data was performed to determine quality of the data. Initial results were promising and followed the theoretical expectations closely.

The second deployment performed near continuous measurements of the Earth disk target from June 19th of 2006 to June 23rd 2006. Tip curve measurements were performed periodically as an external calibration. The position of GeoSTAR-D relative to the Earth disk target was chosen such that the sun would pass directly behind the target

during the day. Figure 4.7 shows a sun transit, where the target completely obscures the sun, and measurements made at dusk.

Figure 4.7: GeoSTAR-D Viewing the Target (Left) During a Sun Transit and (Right) at Dusk

The following preliminary results were generated using the retrieval algorithm outlined in Section 4.5, without the application of the theoretical antenna pattern.

4.4.1 NEAR FIELD CORRECTION

Figure 4.8 shows the image retrieval measuring a beacon pulse without near field phase correction and with near field phase correction. In the near field, the point source response has the 'Y' shape of the physical array. With the near field correction, the response is typical of the hexagonal sampling, and matches the theoretical expectations giving us confidence in the methodology outlined in Section 4.3.

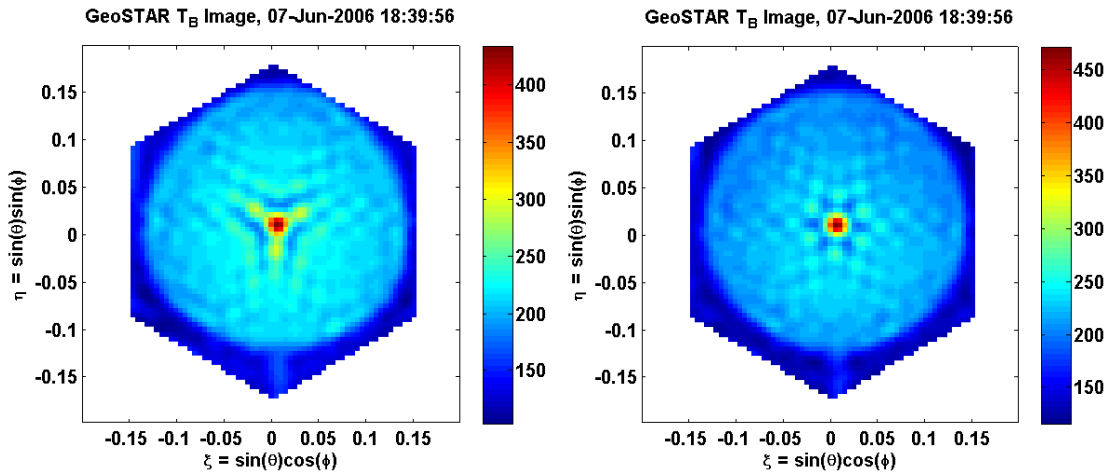

Figure 4.8: GeoSTAR-D Retrieved Brightness Temperatures of a Beacon Pulse (Left) Nominal Processing and (Right) Near Field Correction Applied

4.4.2 IMAGE ALIAS DEMONSTRATION

The impact of aliasing is demonstrated by pointing the instrument away from the center of the Earth disk target. The center of the target is placed at the edge of the field of view such that the half the target is still visible in the field of view. Figure 4.9 demonstrates the aliasing with the only half of the target visible in the field of view.

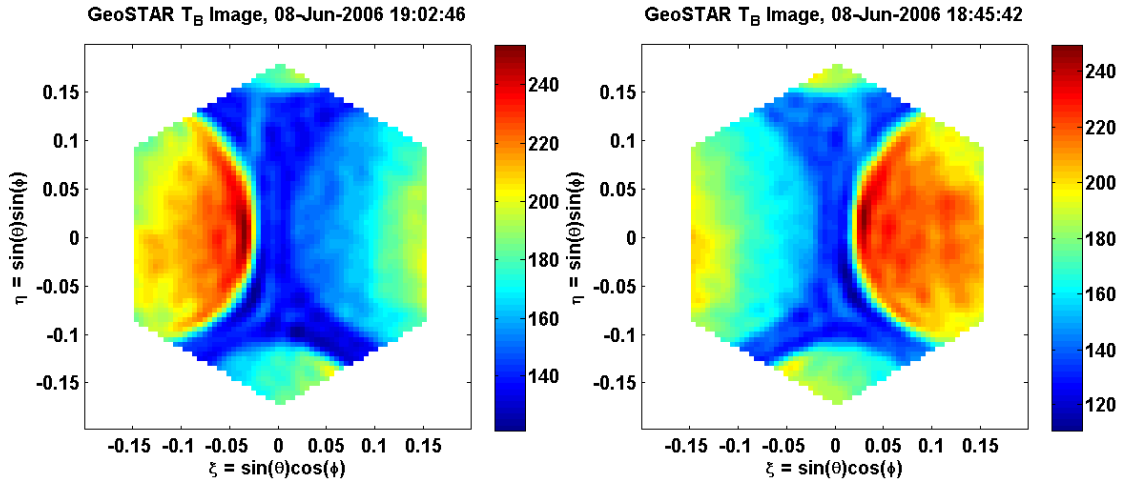

Figure 4.9: GeoSTAR-D Observing Off the Earth Disk Target Center to Demonstrate Aliasing (Left) Earth Disk Target is Left of Instrument Boresight and (Right) Right

The brighter areas represent the real target within the field of view. The gradient away from nadir represents the antenna pattern suppression that is not accounted for in

this nominal processing. The image alias appears with further reduced levels in the field of view due to the same antenna pattern effects.

4.4.3 SUN TRANSIT

Figure 4.10 shows successive images generated as the sun moves behind the Earth disk target.

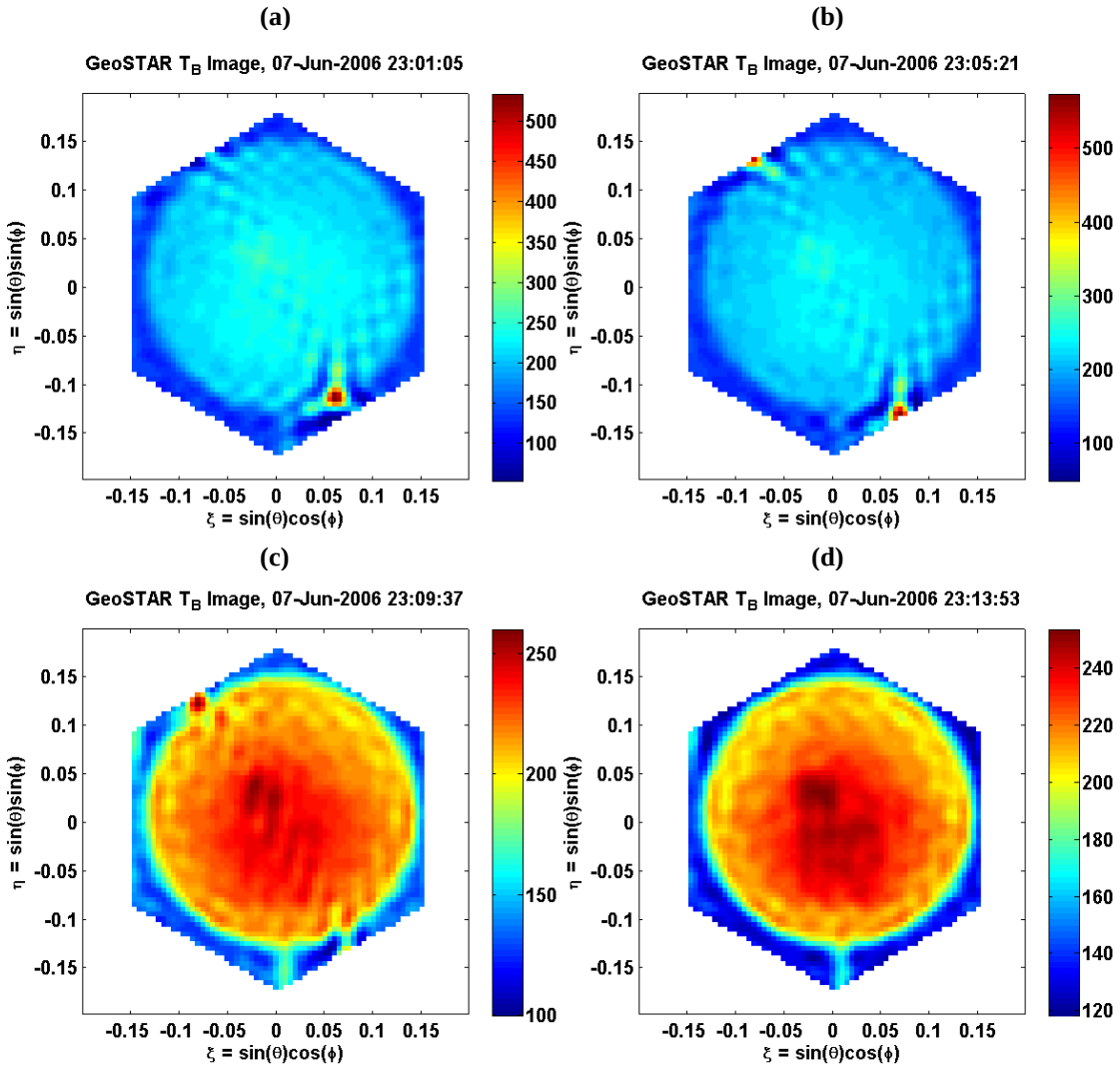

Figure 4.10: Sequence Showing a Sun Transit Behind the Earth Disk Target
(a) Actual Sun Position in the Northwest of the Image, But Aliased Sun in Visible in Southeast
(b) Actual Sun Now Visible in the Image, while Alias Moves Out of the Image
(c) Sun is Right at the Edge of the Target in Northwest (d) Sun moves behind the Target

The sun first appears in the field of view due to aliasing and is a bright source even with the antenna pattern suppression, Figure 4.10a. The sun does not have a hexagonal point spread function since the near field correction is applied, and the source is actually in the far field, resulting in an over correction. Figure 4.10b shows both the sun (northwest) and its alias (southeast) present in the image at the same time. Figure 4.10c shows the image right before the sun is obstructed by the target and in Figure 4.10d the sun is fully behind the target. The four images are generated in a span of about 12 minutes.

4.5 GENERATING GROUND TRUTH MODELS

For the GeoSTAR-D calibration validation, two different models must be generated, one for the brightness temperature of the atmospheric background and another for the physical temperatures across the Earth disk target. The brightness temperature of the atmosphere is retrieved using a complementary instrument and a simplified atmospheric opacity model. The Earth disk target model requires interpolation and extrapolation of the measured data and a methodology to retrieve the physical parameters (such as target range, roll, pitch and yaw). Careful measurements of the physical target parameters were not performed between measurement cycles so these must be retrieved. Figure 4.11 demonstrates the instrument to target pointing calibration.

Figure 4.11: Instrument Pointing Calibration Conducted During the Mesa Tests

4.5.1 ATMOSPHERIC BACKGROUND MEASUREMENTS AND MODELING

The background temperature of the sky was measured using the JPL water vapor radiometer (WVR) which operates at 20.7 and 31.4 GHz. Measurements were performed simultaneously with the tests conducted at the mesa antenna range. Determining brightness temperatures at 50.3 GHz from the WVR was based on pressure-corrected regression of forward modeled radiances from representative radiosondes data. This model was provided by Dr Shannon Brown at JPL. The 50.3 GHz zenith brightness temperatures were then converted into elevation angle corrected values using the following simplified model [58, 65]

$$T_B(\theta) = T_e - (T_e - 2.7) l_Z^{1/\sin(\theta)}, \text{ where } l_Z = \frac{T_e - T_Z}{T_e - 2.7} \quad (4.2)$$

Where

θ	=	Elevation Angle [^{0}]
T_e	=	Effective Air Temperature of 285 K
l_Z	=	Zenith Transmissivity
T_Z	=	Zenith Brightness Temperature [K]

Figure 4.12 shows the generated atmospheric brightness temperature over the hemispherical field of view with a GeoSTAR-D elevation of 39^0. The instrument image retrieval field of view is outlined in white.

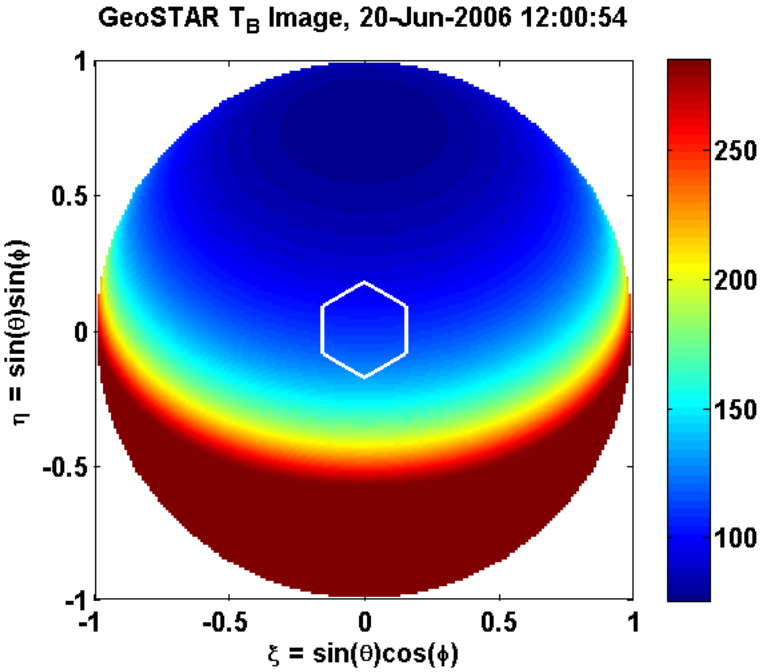

Figure 4.12: Atmospheric Brightness Temperature at 50.3 GHz for Entire Field of View

This atmospheric brightness temperature model is integral for algorithms that investigate image alias removal, but will also be used as the background for the Earth disk model.

4.5.2 ADDED THERMISTORS FOR TEMPERATURE INTERPOLATION

To generate a filled image of physical temperatures on the target, additional sample points must be defined on the target model. The simulated image is built up by first defining the points within each independent heater zone. Since these zones are physically

separated from the disk background, these temperatures must be calculated separately to prevent false interpolation gradients. The temperatures of the unheated disk background are then generated, and the calculated temperatures for the heated areas overlaid on top of the background temperatures. Figure 4.13 and Figure 4.14 shows the added thermistors points in the 2x2 ft and 4x4 ft heated areas respectively. Real thermistors are marked with an '**x**' and the added thermistors are marked with an '**o**'.

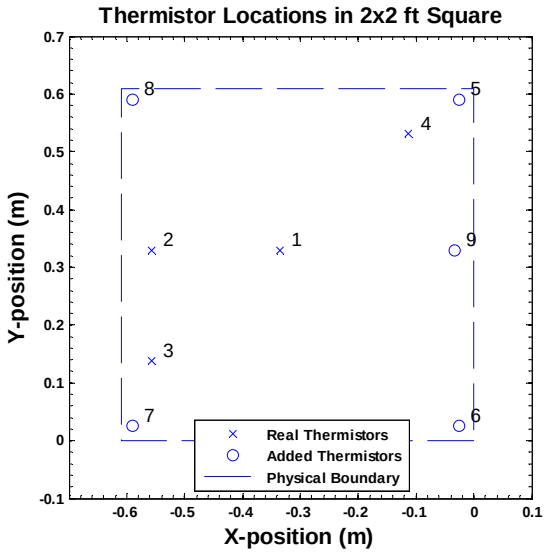

Added thermistor properties for 2x2 ft square:-
#5 and #8 = #4 (vertices)
#6 and #7 = #3 (vertices)
#9 = #2

Figure 4.13: Real and Added Thermistor Locations in the 2x2 ft Heated Area

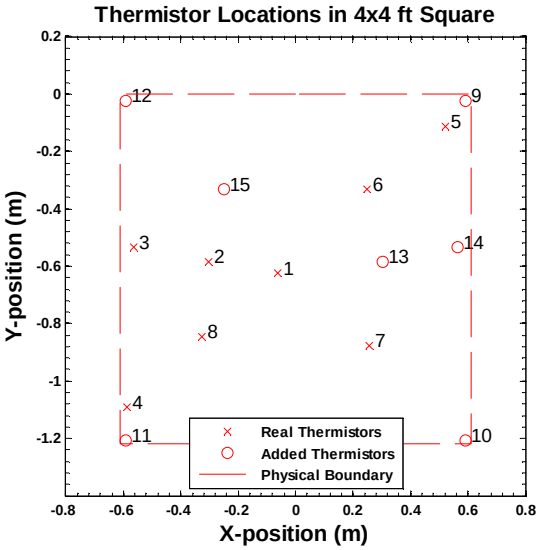

Added thermistor properties for 4x4 ft square:-
#9 and #12 = #5 (vertices)
#10 and #11 = #4 (vertices)
#13 = #2
#14 = #3
#15 = #6

Figure 4.14: Real and Added Thermistor Locations in the 4x4 Heated Areas

Figure 4.15 shows the added thermistors on the unheated background.

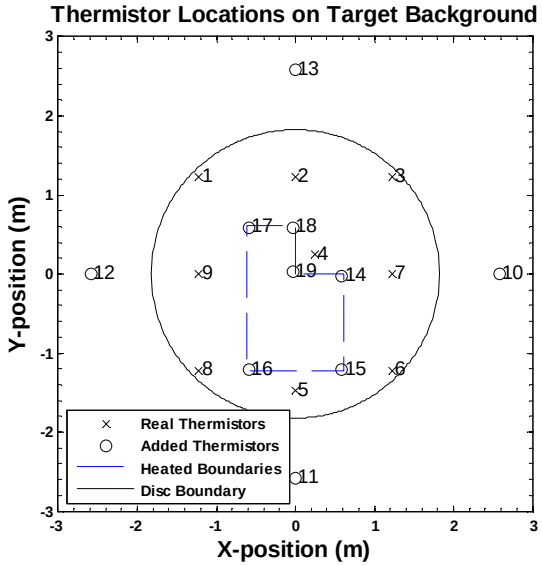

Added thermistor properties for target background:-
#10 = #7 (vertice)
#11 = #5 (vertice)
#12 = #9 (vertice)
#13 = #2 (vertice)
#14 = (#4+#7)/2
#15 = (#5+#6)/2
#16 = (#5+#8)/2
#17 = (#1+#2+#9)/3
#18 = (#2+#4)/2
#19 = #4

Figure 4.15: Real and Added Thermistor Locations on the Target Unheated Background

In general the added thermistors will be at the vertices of the interpolation area so that all values can be interpolated. The value for the added thermistors is nominally the measurement value of the closest thermistors. This approximation is valid to the first order; however it does not capture the fine temperature gradients on the target. The interpolation is performed using linear Delaunay triangulation. Figure 4.16 shows a sample model output of the target temperature distribution for an afternoon scene. For this scene, both heating zones are active, and the target background temperature is approximately 32 ^{0}C (305 K).

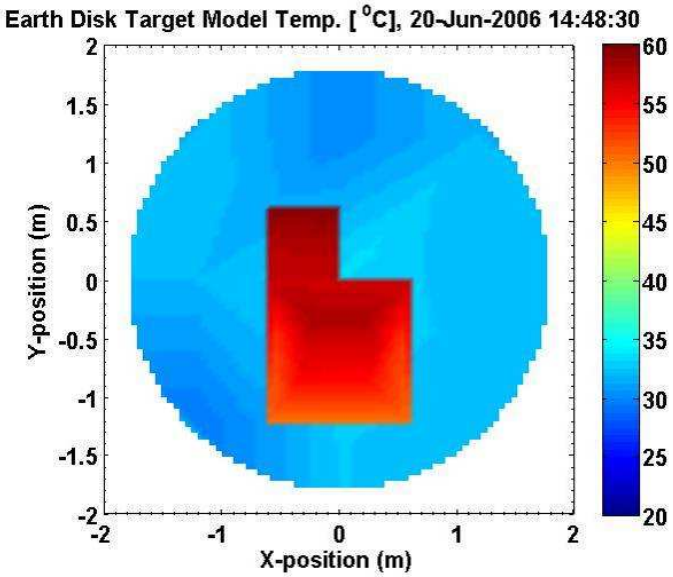

Figure 4.16: Sample Earth Disk Target Model Temperatures [^{0}C]

In addition to the generation of the physical temperature map, the target model also allows for variation of the physical antenna parameters of roll, pitch and yaw and the relative positional parameters of target center and range. This allows for the geometry of the target model to match the actual measurement plane.

4.6 VISIBILITY CORRECTION ALGORITHMS

The current image retrieval algorithm is simple and does not account for the effects due to the aliases or the known impact of spatial frequency truncation, known as Gibbs ringing [69, 70]. The following improved image retrieval methods rely on the property that the relationship between the brightness temperatures and the visibilities is linear. The algorithm is improved incrementally, first by accounting for the sky alias and then a differential model to account for the Gibbs phenomenon. Similar methodologies have been proposed [71] for error reduction in image retrievals.

4.6.1 SKY BACKGROUND CORRECTION

A usable sky model was developed in Section 4.5.1, based on concurrent measurements performed by the WVR. This model is input into a forward model in order to generate the sky visibilities that GeoSTAR-D would measure. The forward model is generated for the full forward half space ($\xi^2 + \eta^2 \leq 1$) so that the aliases are properly generated. In order to perform this calculation, the forward model sampling density is evaluated in the visibility space to determine the smallest sampling density that would produce tolerable errors in the final visibility. The forward model that describes the sky visibilities can be represented in a similar manner to (3.22)

$$V_{FFOV,Sky} = G_{FFOV} F_{FFOV} T_{FFOV,Sky} \tag{4.3}$$

Where

$V_{FFOV,Sky}$	=	Sky Visibilities, Full Field of View [K]
G_{FFOV}	=	G-Matrix, Full Field of View
F_{FFOV}	=	Antenna Pattern Model, Full Field of View
$T_{FFOV,Sky}$	=	Sky Brightness Temperature, Full Field of View [K]

Since the system is linear, the difference between the actual measured scene and a scene with sky only and aliases is

$$V_{D,Sky} = V_M - V_{FFOV,Sky} \tag{4.4}$$

Where

$V_{D,Sky}$	=	Difference Between Measured and Sky Visibilities [K]
V_M	=	GeoSTAR-D Measured Visibilities [K]

The same retrieval algorithm is then applied as (3.23) to generate the estimated brightness temperature with the sky and its aliases removed.

$$\hat{T}_{D,Sky} = F^{-1} G^{-1} V_{D,Sky} \tag{4.5}$$

Where

$\hat{T}_{D,Sky}$	=	Retrieved Brightness Temperature with Sky and its Aliases Removed [K]

Recall that this retrieval only generates the brightness temperatures in the defined GeoSTAR-D field of view, as demonstrated in Figure 4.1 and Section 4.3.4. To return to the actual sky alias corrected image, the sky brightness temperature distribution within the field of view, T_{FOV}, must be added back to $\hat{T}_{D,Sky}$

$$\hat{T}_{B,DA} = \hat{T}_{D,Sky} + T_{FOV,Sky} = F^{-1}G^{-1}(V_M - G_{FFOV}F_{FFOV}T_{FFOV,Sky}) + T_{FOV,Sky} \quad (4.6)$$

Where

$\hat{T}_{B,DA}$ = Retrieved Brightness Temperature with Sky Alias Correction [K]

T_{FOV} = Sky Brightness Temperature, GeoSTAR-D Field of View [K]

(4.6) is the same expression shown in [58, 65], and $\hat{T}_B$ now has the aliases from the sky removed.

To show the performance of the algorithm, a scene is selected where both heater zones are active, with the 4x4 ft square at a slightly higher physical temperature (60^0C) than the 2x2 ft square (55^0C). Figure 4.17 shows the results of the processing from Section 3.6 with F^{-1} uniform (flat) and with the ideal element pattern.

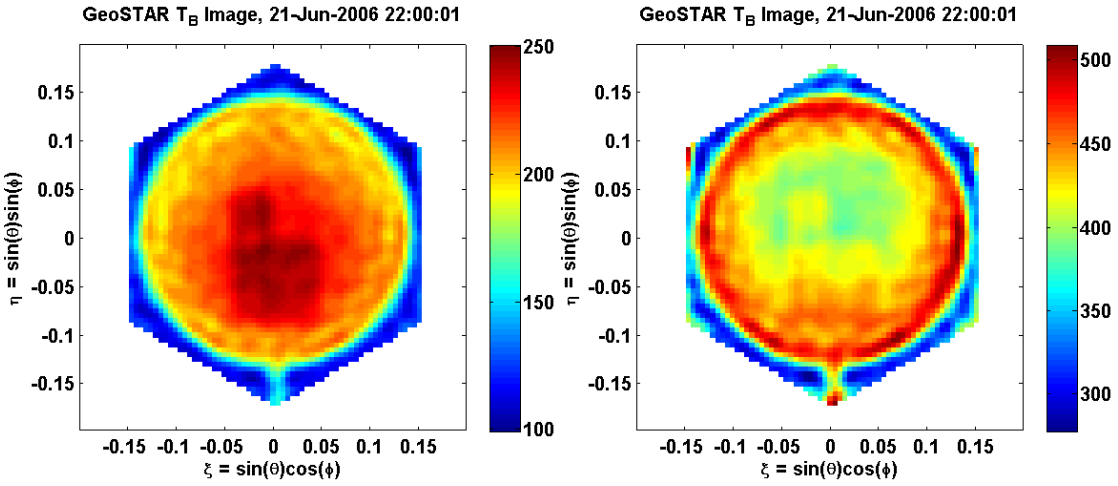

Figure 4.17: Processing with (Left) Flat Antenna Pattern and (Right) Theoretical Antenna Pattern

With the theoretical antenna patterns applied, the retrieved brightness temperatures are very large, a result of the image aliases. Note that for the eventual GeoSTAR system, the cold space aliases are several orders of magnitude smaller than the current sky

background (~100 K vs. ~2.7 K), so the impact will not be as pronounced as in this demonstration.

Figure 4.18 shows the result of the sky alias removal outlined by (4.6). The magnitude of the retrieved brightness temperatures are now closer to the expected values with the sky aliases removed.

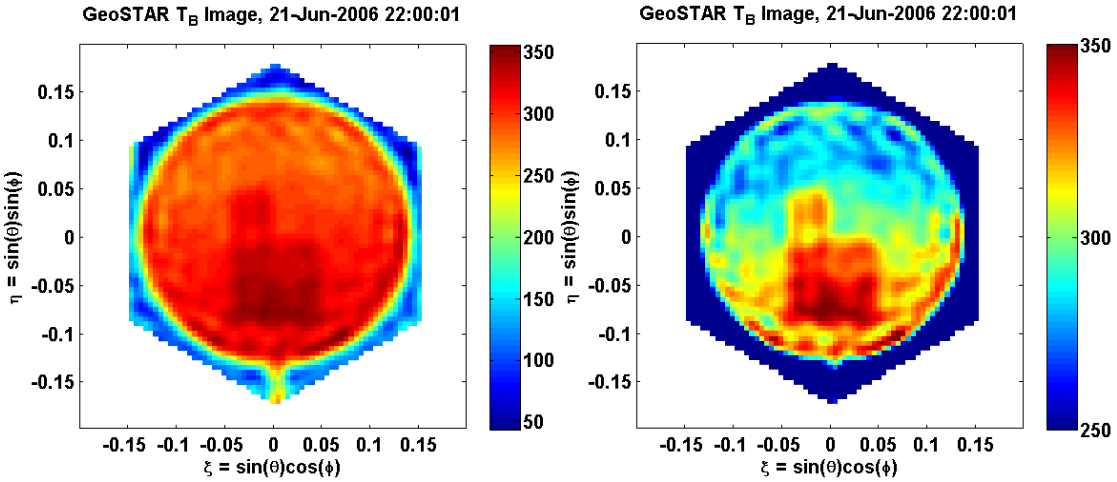

Figure 4.18: Sky Alias Removal Processing (4.6) (Left) Full Scale and (Right) Reduced Scale

The image on the right shows a reduced color scale output where an unrealistic gradient on the target is observed. This gradient is due to the pointing errors between the elemental antennas and the instrument as a whole that were observed in the anechoic chamber. Applying the gross pointing correction that was determined from the comparison to theoretical patterns in Section 3.6.3, a more realistic image is generated in Figure 4.19. A significant amount of variation on the target disk has been removed by the application of this correction. Note however that ripples are still evident in the image due to the Gibbs phenomena, and mitigation of this will be discussed shortly.

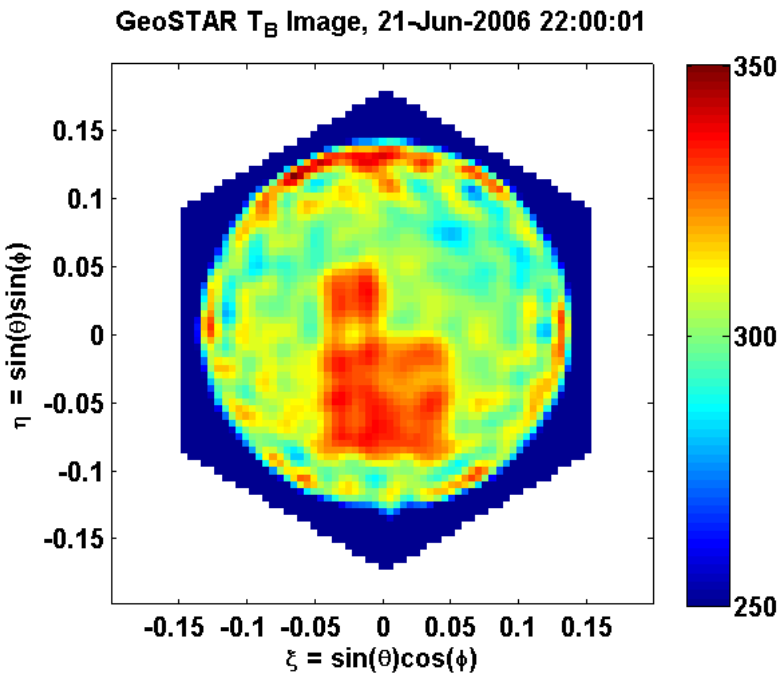

Figure 4.19: Retrieved Image with Sky Aliases Removed and Gross Pointing Correction Applied

From the image, the maximum temperatures are still higher than expected. Some of these effects are due to the elemental antenna pointing errors which have yet to be integrated into the calibration. The exact deviation of the current retrieved image from the actual scene requires comparison to the target thermistors.

4.6.2 EXTRACTING RANGE PARAMETERS

The range parameters are estimated for each measurement set independently since the relative position between the instrument and the target varied. Before solving for the range parameters, the target center position must be determined, easily obtained by solving for the target beacon which is physically located at the center of the target. The range image error is defined as the RMS difference between a sky alias calibrated image (4.6) and the image generated by the target model, and will be used in the subsequent analysis. The first target parameter solved is the target range, which determines the size of the disk. This represents the first overall correction. From there, the fine correction of

the target roll, pitch and yaw can be performed. Figure 4.20 shows a flow chart that describes the procedure to determine the target parameters.

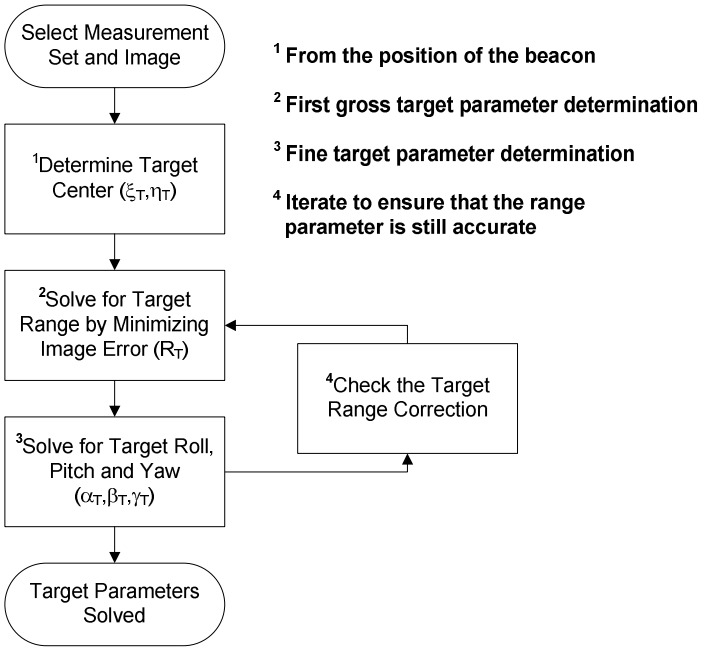

Figure 4.20: Flow Chart Describing the Target Parameter Extraction

Figure 4.21 shows the results of the parameter determination with the scene from Section 4.6.1.

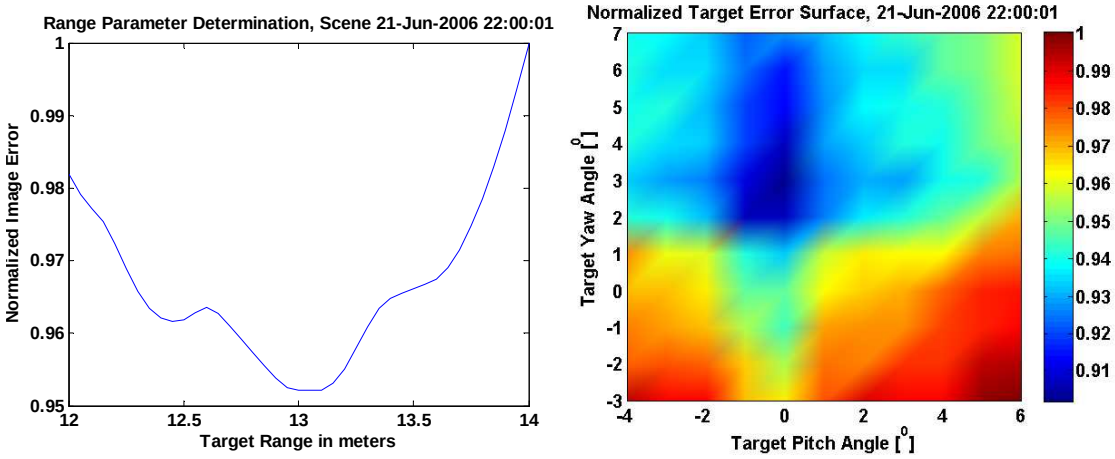

Figure 4.21: Target Parameter Values (Left) Range and (Right) Pitch and Yaw

Results from the various datasets indicate that the position of the target roll is consistent in all the datasets, and as such the fine parameter reduction is performed for the pitch and

yaw only. For this particular measurement set, the beacon center is almost zero ($\xi_T = 2.5e-4, \mu_T = -5e-4$), the target range is, $R_T = 13.1m$ and the target roll, pitch and yaw are $\alpha_T = 0, \beta_T = 0, \gamma_T = 0.05$ radians. The estimation of the range parameters is not perfect due to the nature of the reconstructed image. The impact of the Gibbs ringing at the edges of the retrieved image, which we use to define the physical border of the target, causes false positives on the error surface. The following represents the best guess resolved solution of actual target parameters.

Figure 4.22 shows the direct comparison between the GeoSTAR-D measured brightness temperatures and the model output assuming that the emissivity of the target is 1. The deviations from the model are significant, and the standard deviation of the pixels on the Earth disk target is approximately ~10K.

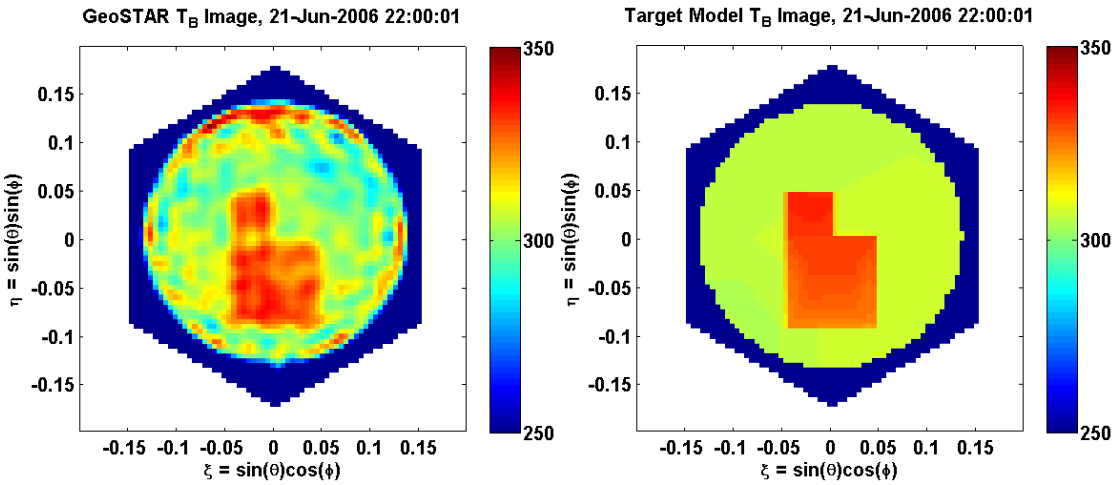

Figure 4.22: (Left) Calibrated Brightness Temperatures and (Right) Target Model Output

The residual errors are due to several sources. The target model is generated with a sparse set of thermistors, resulting in a very smooth temperature field. The temperature distribution of the actual target will be more varied than the model outputs. In addition, the thermistor measurements will be slower to respond to the physical temperature

changes than GeoSTAR-D, by a certain time constant dependent on the thermistors and their embedded location on the target. The following section will deal only with the ripples in the image and the mitigation of the Gibbs phenomenon.

4.6.3 GIBBS PHENOMENA MITIGATION

The starting point of the Gibbs mitigation algorithm will be the de-aliased image from Section 4.6.1 with the addition of the target model. (4.6) is modified to include the Earth disk model full field of view visibilities and GeoSTAR-D field of view temperatures

$$\hat{T}_{B,DA+GM} = F^{-1}G^{-1}(V_{D,Sky} - G_{FFOV}F_{FFOV}T_{FFOV,ED-Sky}) + T_{FOV,Sky} + T_{FOV,ED-Sky} \quad (4.7)$$

Where

$\hat{T}_{B,DA+GM}$ = Retrieved Brightness Temperature, De-Aliased and Gibbs Mitigated[K]
$T_{FFOV,ED-Sky}$ = Earth Disk Model T_B Minus Sky Pixels, Full Field of View [K]
$T_{FOV,ED-Sky}$ = Earth Disk Model T_B Minus Sky Pixels, GeoSTAR-D Field of View [K]
$T_{D,Sky+ED}$ = Retrieved T_B with Sky Alias and Gibbs Removed [K]

To maintain the linearity of the system, the brightness temperature of the sky must be subtracted from the pixels of the target model. In addition, the imperfections in GeoSTAR-D must be replicated in the models in order to create realistic visibilities. This mainly involves the pointing correction that was outlined in Section 3.6.3 and applied to generate Figure 4.19.

It is convenient here to define $\hat{T}_D$, the retrieved brightness temperature after removing the effects of aliasing and correcting for the inadequate sampling visibility domain. This may be interpreted as the algorithm residual error.

$$\hat{T}_D = \hat{T}_{B,DA+GM} - T_{FOV,Sky} - T_{FOV,ED-Sky} = F^{-1}G^{-1}(V_{D,Sky} - G_{FFOV}F_{FFOV}T_{FFOV,ED-Sky}) \quad (4.8)$$

Where

$\hat{T}_D$ = Residual Retrieval Error [K]

If the models were both perfect with full resolution, the resulting $\hat{T}_D$ from (4.8) would tend to the inherent instrument imperfections. Figure 4.23 shows the various images that are generated using the correction algorithm (4.7) and (4.8).

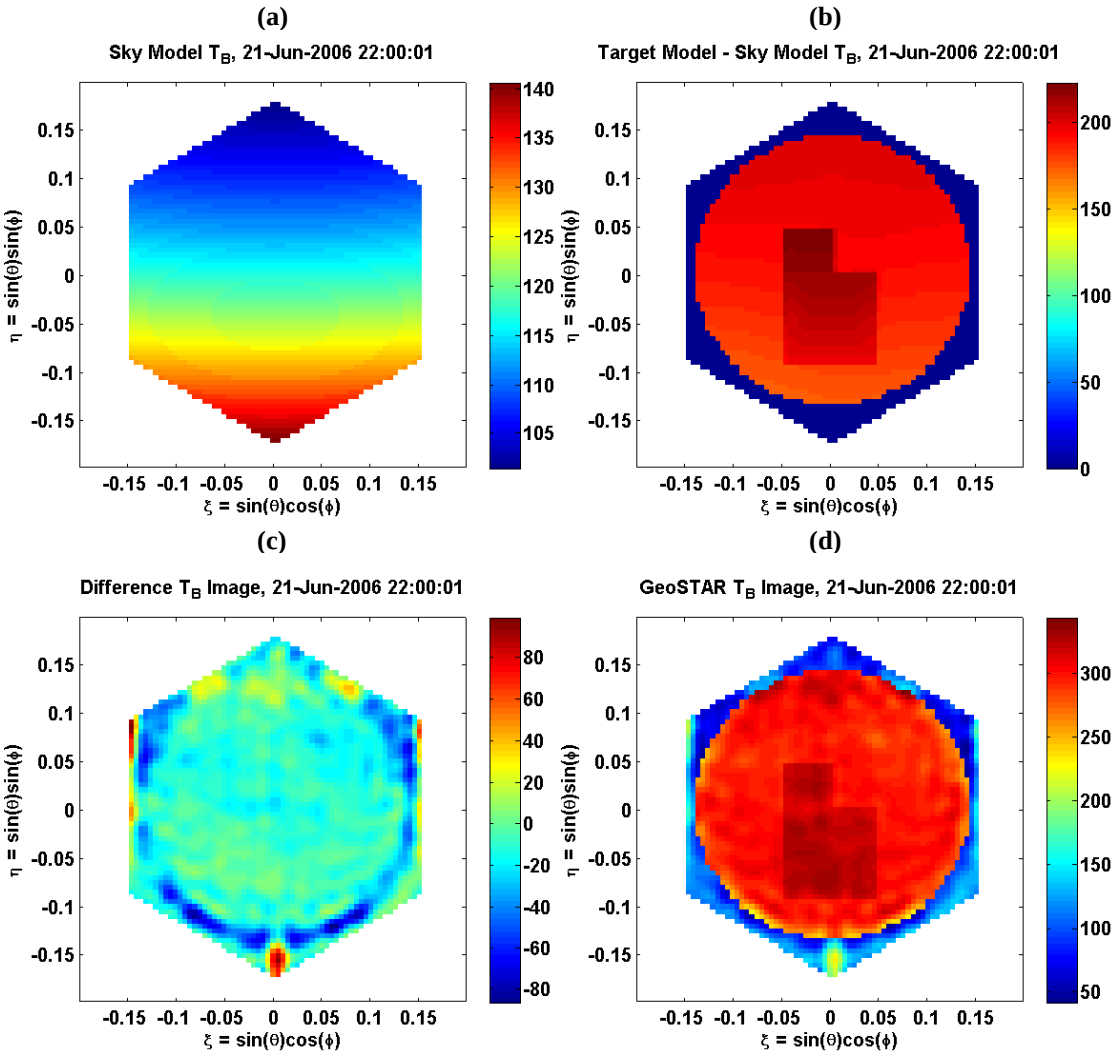

Figure 4.23: (a) Sky Model T_B within the FOV (b) Target Model – Sky Model Pixels T_B within the FOV (c) Residual Retrieval Error (d) GeoSTAR-D Fully Corrected Image

The largest residual error is due to the boom of the range system, which is not modeled and seen in the south of Figure 4.23c with aliases in the northeast and northwest corners. Large errors also appear in the south, most likely due to the imperfect retrieval of the range parameters. The final corrected image in Figure 4.23d is significantly smoother

than Figure 4.19, though small imperfections are still visible. The error of the pixels on the target has been reduced from ~10 K to ~5 K. The Gibbs correction has reduced errors by almost half.

4.7 SUMMARY

GeoSTAR-D was deployed at the JPL mesa antenna range to simulate GeoSTAR type measurements viewing an engineered Earth disk target. The target simulates contrast from continental boundaries with two separate heating zones, and embedded thermistors allow for concurrent measurement of the physical target temperature. A beacon is placed at the center of the target and used for near field correction and location of the target center. A variety of tests were conducted at the mesa, demonstrating the effects of aliasing and the impact of a sun transit on retrievals.

Two separate models are generated, an atmospheric correction model that utilizes measurements the JPL WVR and a target model that extracts the various thermistors readings to generate a full target temperature field. The target model also allows for variation in the pointing parameters which when combined with the proper error minimization scheme can be used to extract the target physical parameters. An iterative scheme is employed that corrects for both the gross and fine geometric errors.

The performance of the originally proposed calibration algorithm utilizing the theoretical G-Matrix and antenna pattern is improved by correcting for pointing errors in the anechoic chamber. A sky alias correction algorithm is proposed that relies on the fact that the brightness temperature and visibility transform relationship is linear. The resulting image has contrast at the right areas and magnitudes close the expected

brightness temperature, a significant improvement over the initial calibrated image. Ripples are evident in the image due to the Gibbs phenomena. A secondary correction utilizing the Earth disk target model reduces the retrieved image errors by almost half, with final error magnitudes of ~ 5 K.

This result is typical of the algorithm performance during the test period and represents an error of less than 2%. This error includes the known imperfections from the anechoic chamber measurements, uncertainties in the target temperatures due to thermal lag and interpolation, thermal sensitivity of the antennas to direct sunlight and noise temperature calibration errors from inadequate temperature and humidity control of GeoSTAR-D. Overall the performance of the instrument is excellent and shows repeatability as the calibration from the anechoic chamber is applied with success in an outdoor environment.

CHAPTER 5

DEVELOPMENT OF A HIGH RESOLUTION FULL EARTH DISK MODEL

5.1 RATIONALE AND NECESSITY

A high resolution full Earth disk model is an important tool that can be used in the development of GeoSTAR, especially in characterizing sensor performance and calibration strategies. This effort can be seen as a first look Observing System Simulation Experiment (OSSE), to answer the basic concerns of the instrument design. In particular, one important issue to be addressed is the magnitude of the measured visibilities, especially at the large baselines, where typically the signal to noise ratio (SNR) is small. This effort attempts to characterize the information content available to the instrument. The error in this measurement has been discussed in Chapter 2 and is a function of the hardware and the integration time. While reasonable guesses at the eventual hardware design can be made, the integration time is a parameter that can be varied, as long as it falls within the original requirement of new images generated (approximately hourly). In addition, the model will allow us to evaluate several proposed image processing strategies, especially in the mitigation of known image effects such as the Gibbs Phenomenon.

Reduced spatial scale Earth models have been successfully used to examine array distortion errors [72]. While appropriate for antenna redundancy and perturbation analysis, these models do not properly account for the high spatial components of the

visibility measurement. Additional analyses performed comparing GeoSTAR to a traditional scanning radiometer have the desired spatial resolution (~5 km) but focus only on regional areas [24]. To this end, a new model must be developed. Initially, the model will be developed for the 50 GHz temperature sounding channels as the assumptions are more easily met.

5.2 FULL DISK MODEL ASSUMPTIONS

The inputs to the model will be outputs of various existing geophysical parameter models. This will reduce the development time significantly if we use already developed products and enhance confidence in the results. In order to utilize these products, several key assumptions must be made so that the results are reasonable for our use. In the following sections, spatial resolution will be defined in either degrees longitude/latitude or kilometers. The rule of thumb conversion relates 1^0 to approximately 100 km at the equator.

5.2.1 HIGH SPATIAL VISIBILITY CONTRIBUTORS

The key assumption in the generation of this model is that not all atmospheric parameters vary significantly at the spatial scales of the measurement. In fact, most parameters vary smoothly spatially and hence contribute minimally to the high frequency components of visibility. The major contributors to the high frequency visibilities are the sharp transitions, in particular the:-

1. Earth disk / Cosmic Background
2. Continental Boundaries
3. Clouds

Of these three, only the clouds change on the time scales of the measurement. The other two parameters vary minimally yearly if at all. While high spatial resolution measurements for all these three contributors are necessary, only the cloud parameters need to be updated regularly. It is this assumption that allows us to combine the appropriate datasets to produce the full resolution inputs into the radiative transfer model.

5.2.2 SCATTERING FREE ATMOSPHERE AT 50 GHZ

The current model does not include a scattering model for precipitation - liquid or ice. The effects of liquid scattering are known to be minimal at 50 GHz since absorption effects dominate, except for large hydrometeors in stratiform and convective precipitation cells [73]. However, ice scattering aloft, especially in strong convective storm cells, is known to produce a brightness temperature darkening and this effect is also unaccounted for in the present model. A scattering model will be integrated should the model be extended for operation at 183 GHz where this is known to be a dominant process.

5.3 GEOPHYSICAL PARAMETER DATASETS

Existing high quality datasets are typically obtained from specialized spacecraft measurements. Additional parameters are generated from numerical weather prediction (NWP) models. In general the following descriptions will only give brief details regarding the parameter retrievals, since each is a research topic in its own right. In many cases several different datasets were evaluated and the suitability of the chosen set is explained rather than the shortcomings of the discarded set. All the chosen datasets are publicly distributed and available for access.

5.3.1 SURFACE PARAMETERS AND VERTICAL ATMOSPHERIC PROFILES

The basis of the model from which the other parameters are overlaid is the National Centers for Environmental Prediction (NCEP) Global Data Assimilation System (GDAS). GDAS is generated every 6 hours using a Medium Range Forecast model (MRF) and consists of the minimum set necessary to regenerate NCEP analysis fields. The primary benefit of using GDAS over other NCEP products is the spatial resolution of the GDAS1 dataset, at 1.0^0 x 1.0^0 gridded equally over the globe. For vertical resolution, the data is available at 26 levels for temperature and geopotential height and 21 levels for relative humidity (up to 10 mb).

In addition to the vertical profiles, GDAS also provides surface fields, including wind speed which is necessary for the generation of the ocean emissivity product.

5.3.2 LAND SURFACE EMISSIVITY

One of the most challenging parameters to define is the land surface emissivity in any satellite measurement. It is common to utilize values that are determined based on the land use classification of the area. However, these values are known to vary depending on the conditions at the location itself, especially that of moisture content which is not easily available. The impact of diurnal variations, especially due to the presence of surface dew is known to decrease emissivity values [74] in the microwave frequencies of interest. A large dataset of derived values will minimize the impact of the diurnal variations.

The French '*Groupe de Modélisation pour l'Assimilation et la Prévision*' (GMAP) provides land emissivity atlases that are derived from cloud-free measurements made on various satellite instruments (SSMI, TMI and AMSU), though we will primarily focus on

the product derived from AMSU [75-77]. Emissivity values derived from the measurements are binned into low and high incidence angles (recall that AMSU scans to a maximum EIA of 58^0), and atlases are available in the form of monthly averages. The difference in the mean emissivity between the 2 incidence angle bins is found to be 0.023 at 50.3 GHz [75], and for all frequencies emissivity is larger at low zenith angles.

Figure 5.1 shows a sample surface emissivity atlas for March 2007 derived from AMSU-A measurements across the globe. Emissivities are typically larger at the lower latitudes due to the impact of the vegetation cover.

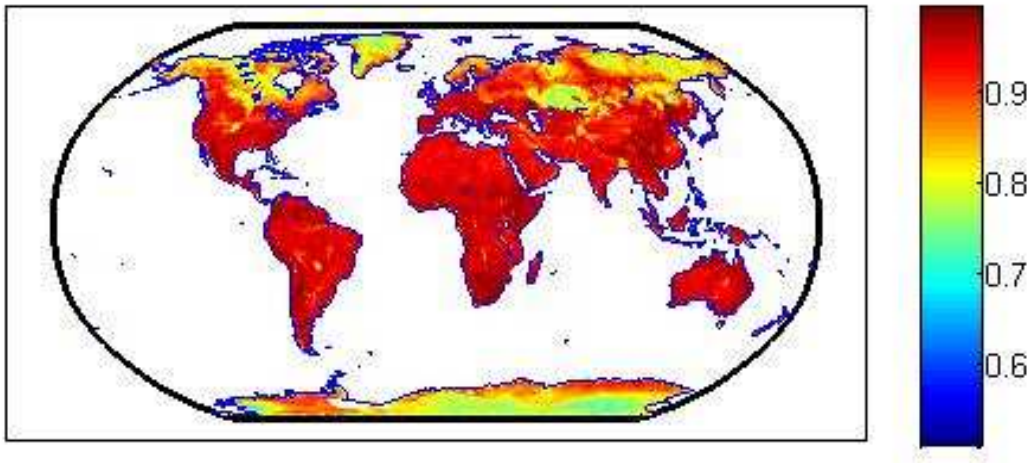

Figure 5.1: AMSU-A Low Angles Surface Emissivity Atlas 50.3 GHz, March 2007

5.3.3 SEA SURFACE SALINITY

Ocean emissivity calculations require sea surface salinity (SSS) values. In general the SSS does not vary significantly temporally and spatially, and as such, a high resolution spatial field is not necessary. The World Ocean Atlas (WOA) from the Ocean Climate Laboratory (OCL) provides objective analyses and statistics for various parameters including ocean temperature, salinity and dissolved oxygen. These fields are available at a 1.0^0 x 1.0^0 grid, and are generated roughly every four years. The most recent version was produced in 2005 (previous versions in 1998, 2001 and 2005) [78].

The chosen dataset is the objectively analyzed monthly means which are smooth filled fields objectively interpolated mean fields generated from the sparse data.

Figure 5.2 shows the smoothed field for the month of March generated with an algorithm that fills the gaps near the coastlines. Areas of low salinity at river mouths are apparent, especially at the Amazon. While the salinity field is a necessary input to generating the ocean emissivity, it is a secondary effect. The parameter that has the largest bearing on the emissivity value is the incidence angle.

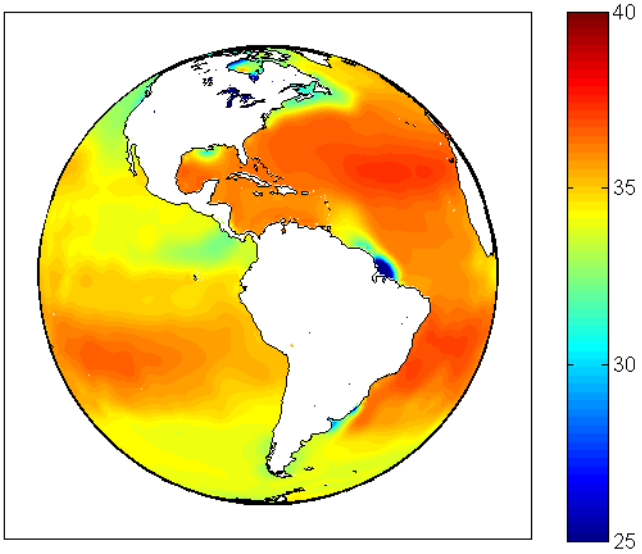

Figure 5.2: WOA2005 Objectively Analyzed Salinity Field March [psu]

5.3.4 CLOUD PRODUCT

A high resolution cloud product is integral to the development of the full earth model. Aside the need for a spatially high resolution image, the spatial extent must also be sufficient. In particular, products derived from GOES data are ideal as they satisfy these criteria, but must be combined with additional inputs in order to produce meaningful results. The NASA Langley Cloud and Radiation Research group generates a cloud product utilizing an algorithm that combines the Visible Infrared Solar-Infrared Split-Window Technique (VISST), Solar-infrared Infrared Split-window Technique

(SIST), and Solar-infrared Infrared Near-infrared Technique (SINT) [79]. Additional inputs to the algorithm include temperature and humidity profiles from NOAA Rapid Update Cycle (RUC) or Global Forecast System (GFS) forecasts for estimations of skin temperature, cloud height and radiance attenuation calculations. Surface-type definition is based on the International Geosphere-Biosphere Program (IGBP) surface map; spatial distributions of snow/ice are taken from real-time maps generated by the NOAA/NESDIS Interactive Multisensor Snow and Ice Mapping System (IMS); and clear-sky reflectance data from the Clouds and Earth's Radiant Energy System (CERES) are used to provide background radiances for cloud detection and retrieval [80].

These products are generated by the NASA Langley Cloud and Radiation Research group at near real time to support numerical weather prediction models (validation and assimilation), estimating surface atmospheric radiation budgets and other 'nowcasting' applications. The most recent release of the dataset extends the Continental United States (CONUS) to a full GOES East disk.

Figure 5.3 shows the first experimental result of the dataset generated on January 3rd 2008. From the figure it is apparent that the product does not extend to the full disk. To reduce longitude gaps, the dataset is combined with similar products for GOES-West and METEOSAT. The gaps in the upper latitudes cannot be filled, however due to the large atmospheric path at those incidence angles, the impact of inaccurate cloud product should be minimal.

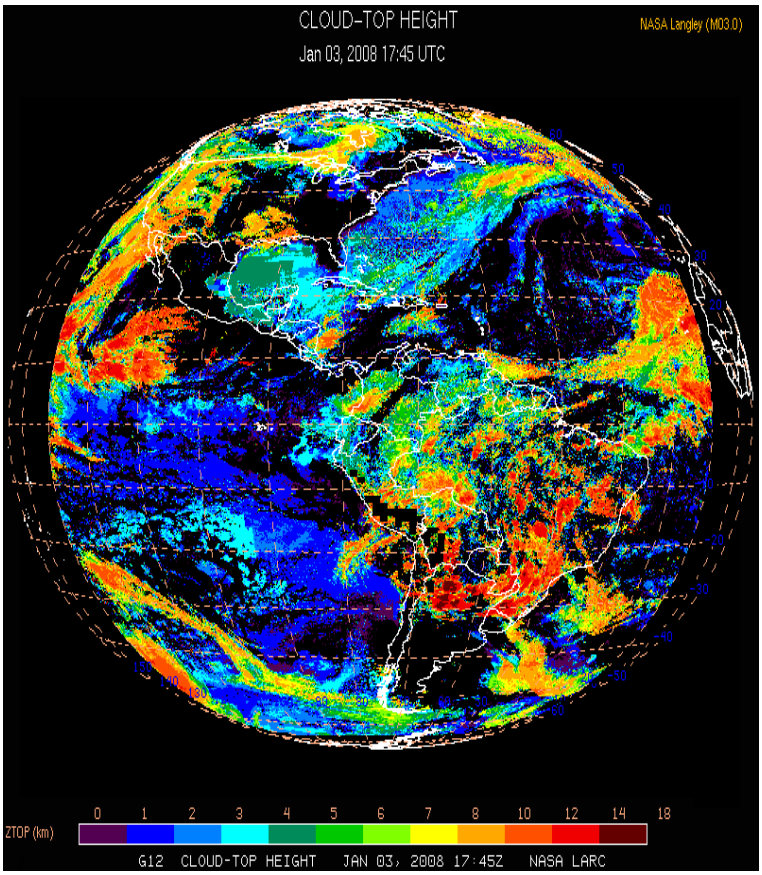

Figure 5.3: LaRC Cloud Top Height GOES-East (01/03/08 23:45Z) [km]

This new full disk product from LaRC is ideal for our use. Note however that the cloud product relies heavily on the visible channels to generate the high resolution product and as such, during times when there is no solar illumination, the actual resolution decreases significantly. As such, data at 00:00Z is partially degraded as most of the GOES-East Earth disk is not illuminated. Figure 5.4 shows the GOES-East 0.65 μm reflectance, a crucial input into the algorithm, at 23:45Z (~00:00Z) showing the extent of data available. At 06:00Z, the entire GOES-East disk is not illuminated. As such for our purposes, we can only utilize products generated for 12:00Z and 18:00Z. This limits the generation of continuous time lapse images, as there are significant gaps daily.

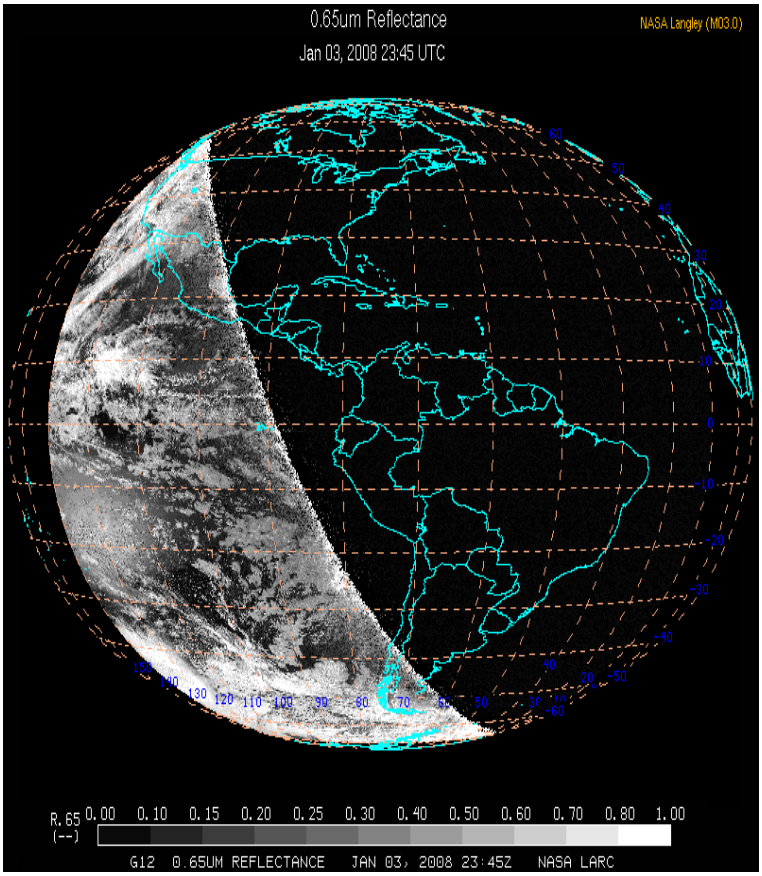

Figure 5.4: LaRC 0.65 µm Reflectance GOES-East (01/03/08 23:45Z)

In addition, as this is a new product, in cases in which the algorithms do not produce realistic results, the entire product is not released. As the algorithm improves, these 'dropouts' in the released full disk cloud product will decrease significantly. The cloud parameters used from the product are a cloud mask, cloud bottom pressure, cloud top pressure and integrated liquid water.

5.3.5 LAND/SEA MASK

The land/sea mask is crucial for the determination of the transitions between the surface emissivity values since liquids and solids have significantly different emissivity characteristics. These sharp transitions will have significant impact on the large baseline visibility magnitudes. The mask selected is obtained from the GODAE High Resolution

Sea Surface Temperature Pilot Project (GHRSST-PP) [81]. The 1 km x 1km resolution product is derived from a similar product available from the USGS, and covers the latitude from 80.3 N to 80.3 S and all longitudes. The reduced latitude is compatible with GEO geometry and our requirements.

The available resolution is several orders of magnitude finer than our needs and allows for more sophisticated processing as opposed to a binary 1 and 0 mask. Each 10 km x 10 km surface pixel is generated from the ensemble of the enclosed pixels to arrive at an effective land fraction. During the generation of the surface emissivities, this fraction is used to combine the emissivity maps to create realistic pixel weighted values. This processing minimizes the introduction of unrealistic visibility components.

5.3.6 DIGITAL ELEVATION MAP

The Digital Elevation Map (DEM) provides the surface position from which atmospheric profiles are valid for the radiative transfer calculation. The National Geophysical Data Center (NGDC) provides several products, of which the ETOPO2v2 Global Gridded 2-minute Database is found to be the most suitable [82]. The vertical resolution is 1 m and the spatial resolution is approximately 4 km x 4km. The dataset also includes ocean depth which we do not utilize.

5.3.7 DATASET SUMMARY

Table 1.1 summarizes the various parameter datasets that are used with emphasis on the temporal and spatial resolution. The highlighted values represent the crucial datasets that have spatial resolution of 8km or better. A total of 6 different datasets are utilized to produce the high resolution Earth disk model.

Table 5.1: Summary of the Various Parameter Datasets Used

Measured Parameters	Data Source	Spatial Res.	Temporal Res.	Levels
Land Emissivity	NWPG France	50km x 50km	Monthly Averages	Surface
Ocean Wind Speed	NCEP GDAS	100km x 100km	6 Hour Refresh	Surface
Sea Surface Temp.	NCEP GDAS	100km x 100km	6 Hour Refresh	Surface
Sea Surface Salinity	WOA 2005	100km x 100km	Monthly Averages	Surface
Temperature Profile	NCEP GDAS	100km x 100km	6 Hour Refresh	26 Pressure Levels
Geopotential Height	NCEP GDAS	100km x 100km	6 Hour Refresh	26 Pressure Levels
Humidity Profile	NCEP GDAS	100km x 100km	6 Hour Refresh	22 Pressure Levels
Surface Parameters	NCEP GDAS	100km x 100km	6 Hour Refresh	Surface
Cloud Liquid/Ice Water	NASA LaRC	8km x 8km	~3 Hour Refresh	
Cloud Top/Bottom Temp.	NASA LaRC	8km x 8km	~3 Hour Refresh	
Land Sea Mask	GODAE GHSTT	1km x 1km	Generated in 2002	Surface
Digital Elevation Map	NGDC	4km x 4km	Generated in 2006	Surface

5.4 GEOPHYSICAL PARAMETER MODELS

In addition to the raw input data, many other variables have to be derived utilizing the appropriate geophysical parameter model prior to the application of the radiative transfer model. Similar to Section 5.3, many models were evaluated, and the following description will deal only with the selected models.

5.4.1 OCEAN EMISSIVITY

The dielectric constant of water is computed from the Klein-Swift model [83]. A correction for roughness and foam fraction is calculated using coefficients from FastEM2 developed for Radiative Transfer for TOVS (RTTOV), code and algorithms generated for the TIROS Operational Vertical Sounder (TOVS) [8]. The specific coefficients used are those optimized for AMSU-A, the POES version instrument that performs GEOSTAR-like measurements.

The model inputs frequency, temperature, salinity, wind speed and incidence angle of measurement to generate the ocean emissivity values in both vertical and horizontal polarization.

5.4.2 GASEOUS ABSORPTION

Absorption for atmospheric gases, including water vapor is, calculated using the Rosenkranz98 absorption model [84]. The model provides absorption coefficients for oxygen, nitrogen and water vapor, given a frequency, temperature, pressure and water vapor density.

5.4.3 CLOUD PARAMETERS

Several different cloud parameters must be calculated. Cloud liquid absorption is calculated under the assumption that the absorption is proportional to the column density of the cloud liquid [85]. Cloud liquid profiles are assumed to be constant in height given a cloud liquid path. This approximation is valid to a first order as no distinction is made between different cloud types in the model. As such, applying any specific profile to the entire Earth disk would not improve the accuracy. Finally, the vertical profile of liquid in the freezing layer is modeled by an exponential lapse [86].

5.5 RADIATIVE TRANSFER MODEL

The standard radiative transfer equation for calculating the brightness temperature as seen at the top of the atmosphere is [73]

$$T_b(\theta) = T_u(\theta) + T_e(\theta)e^{-\tau_0 \sec\theta} + T_r(\theta)e^{-\tau_0 \sec\theta} \quad (5.1)$$

Where

T_b	=	Top of Atmosphere Brightness Temperature [K]
T_u	=	Upwelling Atmospheric Brightness Temperature [K]
T_e	=	Surface Emitted Brightness Temperature [K]
T_r	=	Surface Reflected Atmospheric Brightness Temperature [K]
θ	=	Angle from Nadir [degrees]
τ_0	=	Total Atmospheric Opacity
$\sec\theta$	=	Slant Path Correction in a Plane Parallel Atmosphere

Three major components make up (5.1), the upwelling brightness temperature of the atmosphere $(T_u(\theta))$, the emitted brightness temperature from the surface $(T_e(\theta))$ and the reflected atmospheric brightness temperature from the surface $(T_r(\theta))$. Note that all these expressions are also a function of frequency, but the explicit dependence is dropped in the equations for brevity.

The upwelling atmospheric brightness temperature is expressed as

$$T_u(\theta) = \sec\theta \int_0^{TOA} T(z)\alpha(z)e^{-\tau(z)\sec\theta}dz \quad (5.2)$$

Where

TOA	=	Level of the Top of the Atmosphere [km]
T	=	Physical Temperature [K]
z	=	Height of the Evaluated Layer [km]
α	=	Absorption Coefficient
τ	=	Opacity of that Layer to the TOA

(5.2) represents the integrated upwelling radiation contributed from each layer z to the top of the atmosphere (TOA). The integrated absorption $(\tau(z))$ from the layer of interest to the TOA is expressed as

$$\tau(z) = \int_z^{TOA} \alpha(z')dz' \quad (5.3)$$

The emitted brightness temperature from the surface is dependent on the surface conditions, which we will assume to be smooth, homogenous and isothermal. This

reduces the dependence of the emission to only the physical temperature and emissivity of the layer as shown

$$T_e(\theta) = \varepsilon_s(\theta) T_s \tag{5.4}$$

Where

ε_s = Surface Emissivity

T_s = Surface Physical Temperature [K]

The reflected atmospheric brightness temperature only contains the downwelling brightness temperature in the specular direction θ, a results of previous assumptions, and is expressed as

$$T_r(\theta) = [1 - \varepsilon_s(\theta)] T_d(\theta) \tag{5.5}$$

Where

$1 - \varepsilon_s$ = Power Reflection Coefficient

T_d = Downwelling Atmospheric Temperature [K]

The downwelling atmospheric brightness temperature is calculated using

$$T_d(\theta) = T_c e^{-\tau_0 \sec\theta} + \sec\theta \int_{TOA}^{0} T(z)\alpha(z) e^{-[\tau_0 - \tau(z)]\sec\theta} dz \tag{5.6}$$

Where

T_c = Cosmic Background Brightness Temperature [K]

For the downwelling atmospheric brightness temperature, the first term represents the cosmic background radiation component as attenuated by the atmosphere. The formulation for (5.6) is similar to that for (5.2) except the direction of the integration path changes. Figure 5.5 shows the various components of (5.1) as they propagate through the atmosphere.

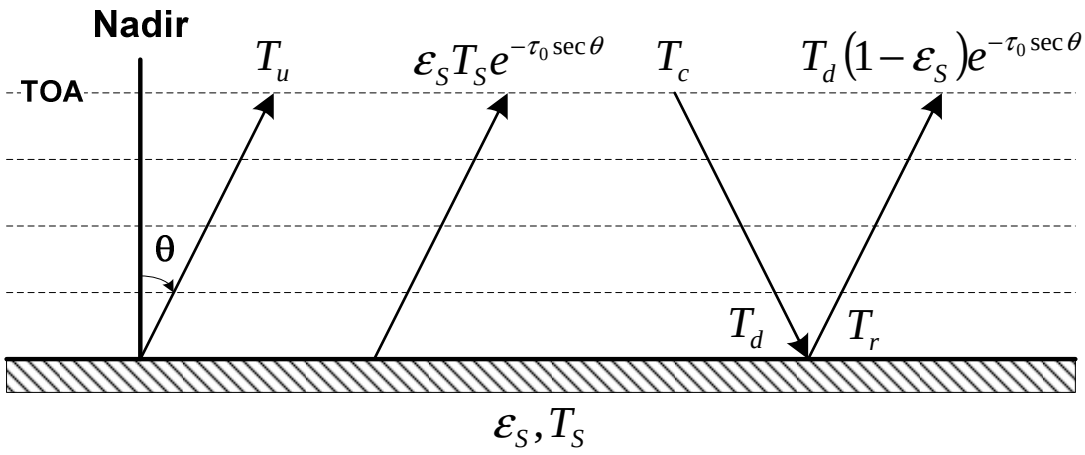

Figure 5.5: Diagram Showing the Components of the Radiative Transfer Calculation

The actual calculation of the TOA brightness temperature is performed using a discrete version of (5.1), and the associated equations.

5.6 COORDINATES AND GRIDS

Two separate coordinate systems are used in the model. The first is the geophysical parameter grid, for which the different atmospheric parameters and model outputs from Section 5.1.2 and 5.1.3 respectively, are overlaid. The second coordinate system is required for the generation of the images in the GeoSTAR frame of reference.

5.6.1 GEOPHYSICAL PARAMETER GRID

The geophysical parameter grid is a 10 km x 10 km equal area grid. Essentially this grid has variable longitude spacing that is dependent on latitude. The longitude spacing increases to compensate for the decreasing circumference of the latitude circle as the coordinates approaches either pole. The resulting geophysical parameter grid has pixels that are equal in area, and it is this grid that the radiative transfer model is applied. Note that from (5.1), the atmospheric path for the upwelling and downwelling is

calculated separately. While the atmosphere is assumed to be plane parallel, each pixel in each layer is based on the actual atmospheric state (i.e. the atmosphere is not homogeneous across each layer).

5.6.2 GEOSTAR GRID

The GeoSTAR image grid is equally spaced in the direction cosine domain. The nadir looking pixel size on the earth disk is 10 km, and increases off nadir. Specific points on the GeoSTAR grid are selected based on the expected image resolution. These points are then co-located on the geophysical parameter grid in terms of latitude and longitude, and the direction of radiation propagation determined by the GEO geometry. The radiative transfer model is then applied at these points.

Figure 5.6 shows a similar viewing geometry if a satellite was placed over the North Pole. The specific case for the GeoSTAR viewing geometry uses the vertical plane of projection [87]. From Figure 5.6, the geometry that causes the poles to be obscured is also demonstrated as the locations for which the horizon is not visible.

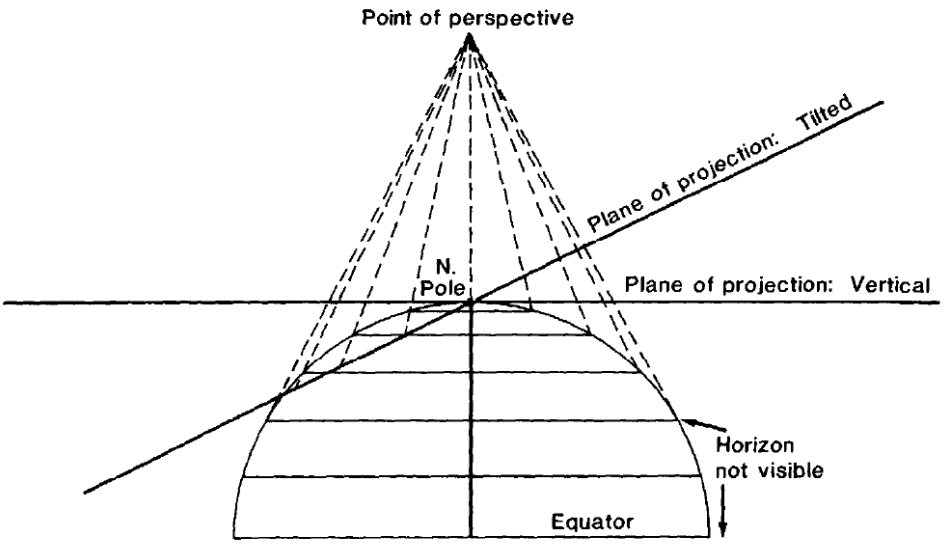

Figure 5.6: Diagram Illustrating the Vertical Perspective Projection [87]

5.7 IMAGE POLARIZATION

The polarization in the image plane differs depending on the pixel of interest. The antennas are currently designed to measure a linear polarization; however, the emission from the polar region is orthogonal to that at the equatorial limb and varies across the entire Earth disk, except at nadir. The emissivity values of the GMAP surface atlases (Section 5.1.2.2) and those derived from the ocean emissivity model (Section 5.1.3.1) are combined to generate a full Earth emissivity map. Figure 5.7 shows the intermediate generated product for which the emissivity is set at the local vertical or horizontal polarization across the entire globe. There is minimal variation with incidence angle for the land surface emissivity values. Ocean emissivity, however, is dominated by the Earth incidence angle (EIA) effect. The divergence of the emissivity values at the different polarizations towards the limbs is consistent with theoretical expectations.

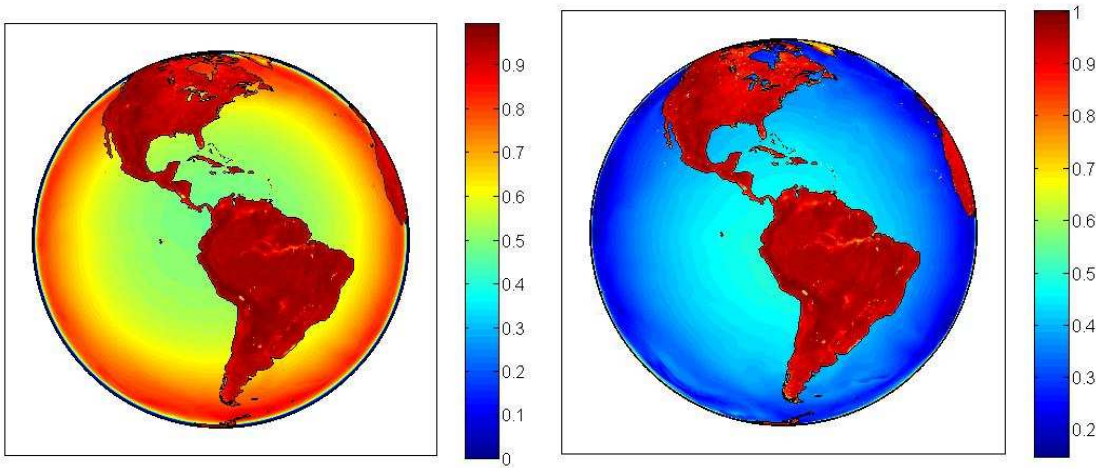

Figure 5.7: Combined Emissivity Map with No Polarization Correction (Left) Vertical Polarization and (Right) Horizontal Polarization

The polarization maps generated in Figure 5.7 are then combined by correcting for the viewing geometry across the Earth disk. The measurement polarization is defined vertical at the poles and varied accordingly across the Earth disk. The following equation

describes the resulting instrument observed surface polarization as a function of the directional cosine coordinates and the azimuthal angle

$$\varepsilon_s(\xi,\eta) = (1-p_c)\varepsilon_{s,V}(\xi,\eta) + p_c\varepsilon_{s,H}(\xi,\eta)\text{, with } p_c = {|\phi|}/{(\pi/2)} \tag{5.7}$$

Where

$\varepsilon_s(\xi,\eta)$	=	Instrument Observed Combined Surface Emissivity
$\varepsilon_{s,V}(\xi,\eta)$	=	Local Emissivity Vertical Polarization
$\varepsilon_{s,H}(\xi,\eta)$	=	Local Emissivity Horizontal Polarization
p_c	=	Polarization Correction Factor

The polarization correction factor has a value of 0 at the poles and 1 at the equator. Figure 5.8 shows the resulting combined vertical polarization emissivity map.

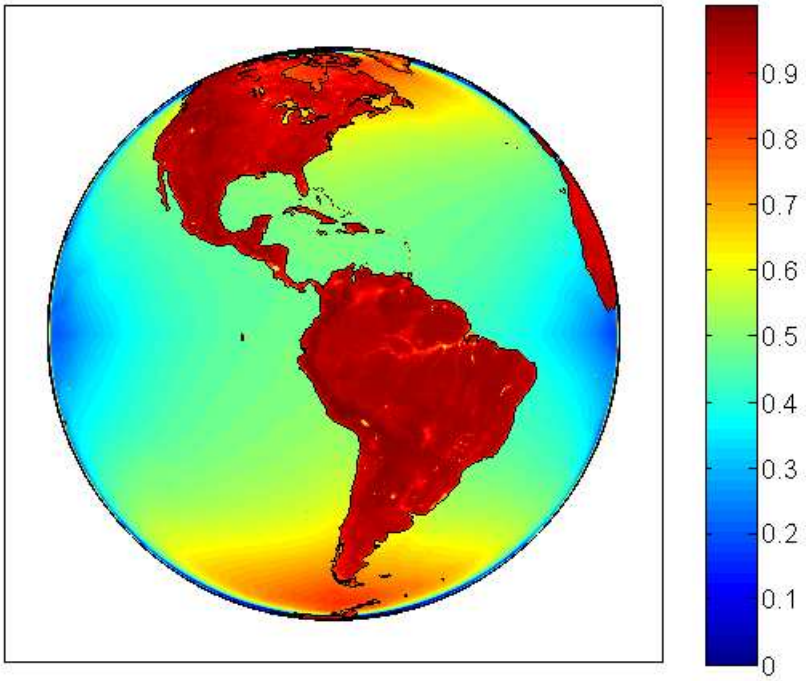

Figure 5.8: Combined Emissivity Map with Vertical Polarization at the Poles

This is the expected operational GEOSTAR mode, with measurements made with vertical polarization at the poles.

5.8 INTERMEDIATE PRODUCT VERIFICATION

The following images show some of the other intermediate products that were generated to verify the model output. These products were used during the development to ensure that the model was performing physically and as expected.

5.8.1 EXCESS EMISSIVITY DUE TO WIND

Figure 5.9 shows the ΔT_B image generated by differencing images for the full model and one for which the wind across the globe is set to zero and the associated surface wind map.

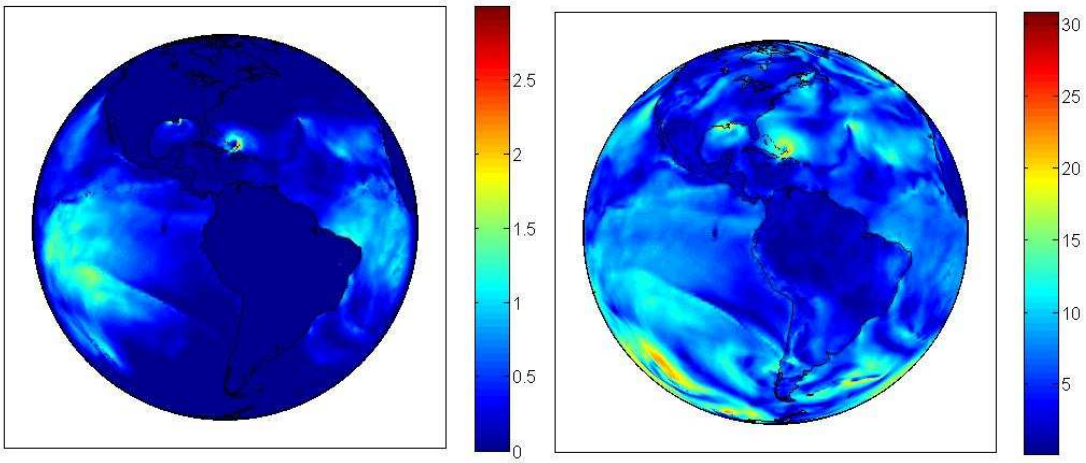

Figure 5.9: (Left) 50.3 GHz ΔT_B Image From Wind Excess Emissivity [K] and (Right) Associated Surface Wind Map [m/s] (09/01/08 18:00Z)

The areas of high winds in the Atlantic where there is significant hurricane activity are visible, as well as regions in the Pacific. Winds closer to the limbs do not have significant impact on T_B due to the large atmospheric path length. In addition, the emissivity response is modified by the polarization mixing across the Earth disk since horizontal polarization measurements are more sensitive to the changes in the winds than vertical polarization. Hence measurements at the north and south poles are muted in comparison.

5.8.2 ATMOSPHERIC TRANSMITTANCE

The total atmospheric transmittance is defined as

$$\Gamma = e^{-\tau_0} \tag{5.8}$$

where τ_0 is the total atmospheric opacity as defined earlier. Figure 5.10 shows the transmittance of the modeled atmosphere at 50.3 GHz on September 1st 2008 at 18:00Z. The transmittance for this window frequency is high, especially in areas of high altitude as seen in the outline of the Andes in South America.

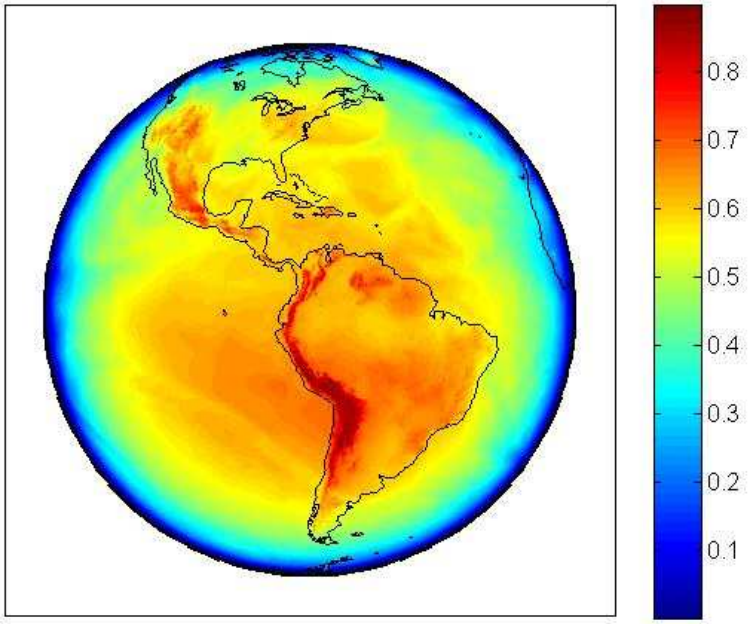

Figure 5.10: Atmospheric Transmittance (09/01/08 18:00Z)

The low transmittance at the limbs is low due to the large atmospheric paths at large earth incidence angles. For the opaque channels, the atmospheric transmittance is close to zero throughout the Earth disk.

5.8.3 EARTH INCIDENCE ANGLE EXTENT

Central to the future discussion of the GOES-East images is an understanding of the geometry of the measurement. The area covered by stepping through various EIA

values is not equally spaced, with different areas subtended by the different incident angles. Figure 5.11 shows the band of EIAs which are larger than 60^0 (left) and 80^0 (right) respectively. The area past 80^0 corresponds to only a small area and includes mostly unusable data due to the extreme atmospheric path lengths and opacity.

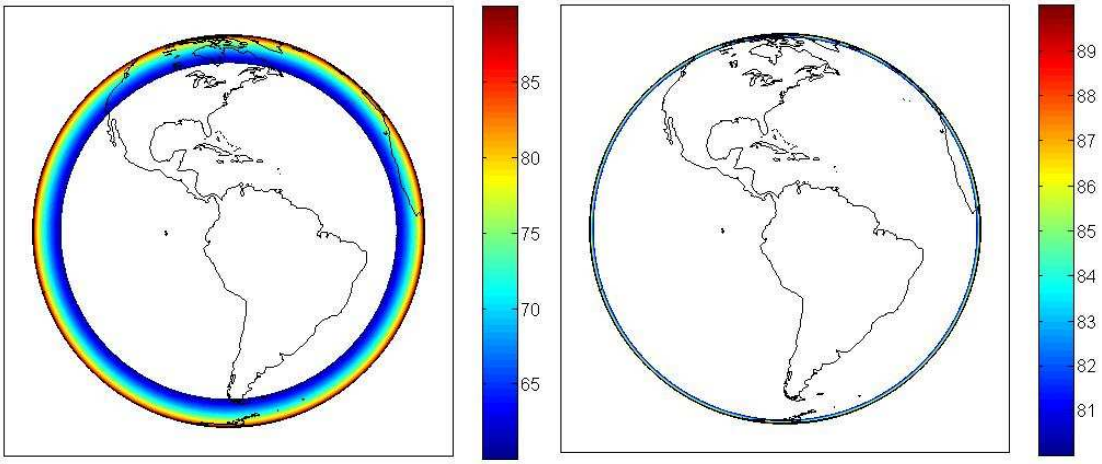

Figure 5.11: (Left) Earth Incident Angle Area > 60^0 and (Right) Earth Incident Angles > 80^0

Currently most GOES-East products are usable only to 60^0; similar LEO microwave sounding instruments have maximum scan angles of 60^0. The regions covered up to the 60^0 extent include most of the continental United States and the Atlantic hurricane region.

5.9 SUMMARY

A high resolution full Earth disk model has been generated with the best available geophysical parameter datasets and models. Leveraging existing data products has decreased the development time of the model significantly. The simulated T_B images will have the highest spatial resolution and coverage available to date to aid in the design and development of the temperature sounding channels of GEOSTAR. The flexibility of the model allows for the creation of non-physically realizable T_B scenes which can be used to assess the instrument sensitivity of different geophysical parameters. In addition

this product can be used in the differential mode to calibrate out Gibb's artifacts as demonstrated in Chapter 4 and applied in Chapter 6. Figure 5.12 outlines the processing in the model.

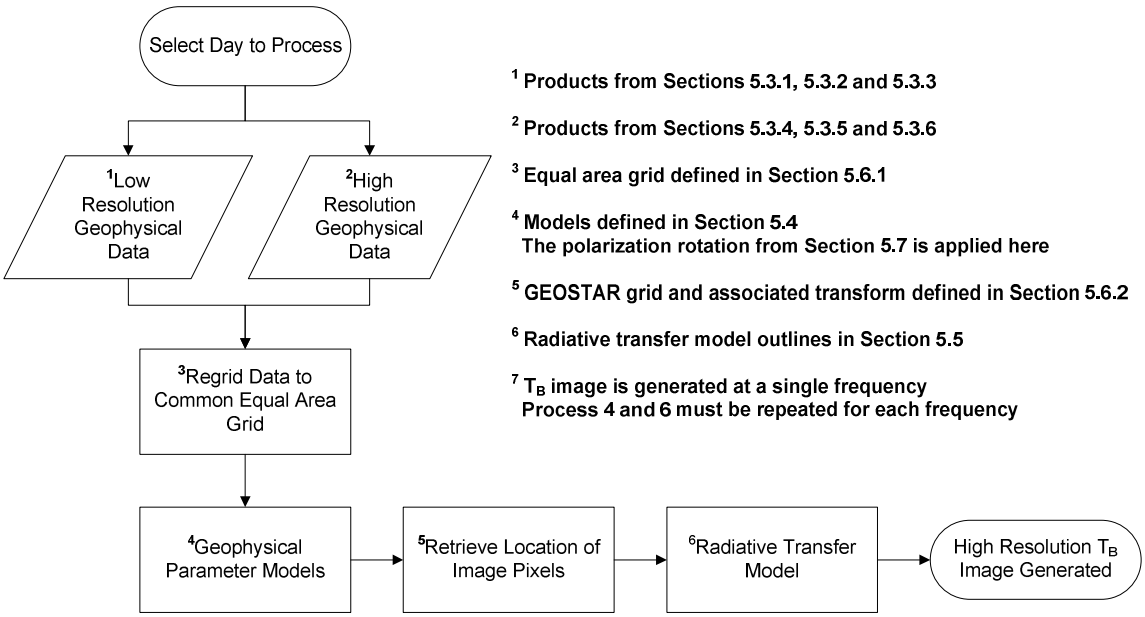

Figure 5.12: High Resolution Model Process Flow Chart Outlining the Major Components

CHAPTER 6

EVALUATING INFORMATION CONTENT AND RETRIEVAL STRATEGIES

6.1 GEOSTAR INSTRUMENT SIMULATOR

The GeoSTAR simulator is implemented in software on the Matrix Laboratory (Matlab^{TM}) platform, on a single desktop personal computer. The full simulation of a theoretical G-Matrix is currently difficult to perform for the full temperature sounding array with N_{EL}=100 (Section 2.1.2), using current computer hardware, especially at the resolution of the full disk model. The number of pixels of the expected GeoSTAR temperature sounder is ~60,000 without oversampling. This number increases to 1.5 million pixels with a 10 km x 10 km nadir resolution for the high resolution model. If the theoretical G-Matrix were to be utilized [32], this matrix would have dimensions of 1.5E6 x 1.5E6, and inversion of this matrix would be challenging and prohibitively time consuming given normal computer hardware.

For the eventual flight system, with more workstations and coupled with parallel and iterative processing, this calculation will be able to be performed. At the moment, the current simulator is simplified, relying on the two-dimensional (2-D) fast Fourier transform (FFT) to perform the conversion from brightness temperature to visibilities.

6.1.1 2-D FFT PROCESSING

Algorithms are available that use rectangular processing [43, 48, 88] to produce a hexagonal output. These methods utilize indexing to a secondary grid and expansion of

the coverage space to be compatible with rectangular algorithms. For simplicity and processing speed, the rectangular processing is maintained. The major difference in the output is simply the sampling scheme in the visibility space, in particular the density, as outlined in Chapter 2. As the following analysis does not utilize specific visibility magnitude values, but instead the averages across spatial frequency ranges, the differences between the rectangular and hexagonal processing is minimal for our evaluation purposes, especially at the larger baselines.

6.1.2 ADDITIVE NEΔV

The value of the NEΔV is calculated using expected GeoSTAR parameters as outlined in Section 2.3. Combining equations (2.17) and (2.20) with the assumptions for the expected hardware and array parameters leads to

$$\Delta T(\xi,\eta)_{\Delta V} \approx 2\sqrt{2\left(\frac{T_A + T_R}{\sqrt{2B\tau}}\right)^2 N} \tag{6.1}$$

(6.1) is a direct relationship between the integration time and the retrieved pixel error if all the other parameters are known. Figure 6.1 shows the trade space for the current array - for a 1 K pixel error, the integration time is approximately 8 minutes and for a 0.57 K pixel error this increases to 24 minutes which is the current requirement.

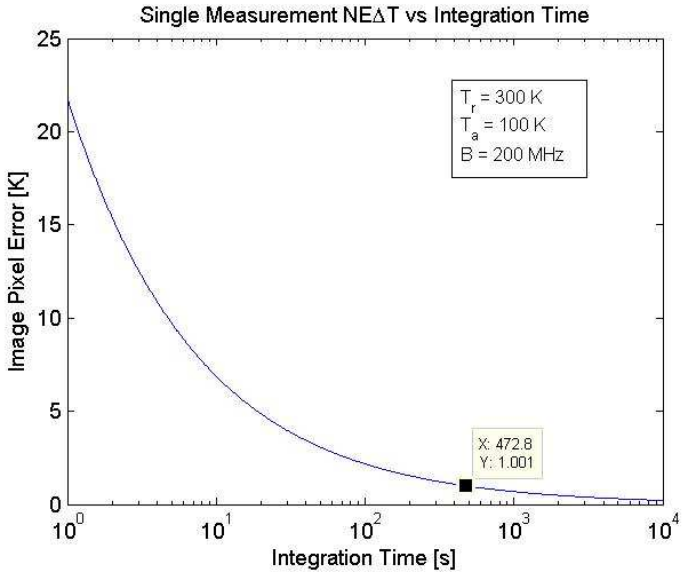

Figure 6.1: Image Pixel Error vs. Integration Time for Temperature Sounding Array [K]

Adding NEΔV error to the simulations is straightforward in the spatial frequency domain, though care must be taken to ensure that the added noise is Hermitian symmetric.

6.1.3 STANDARD PROCESSING ALGORITHM

For ease of discussion, a standard processing algorithm is defined from which other algorithms are compared. This nominal processing method demonstrates how a GeoSTAR type instrument performs measurements in the spatial frequency domain and the inherent information that is unavailable due to the limited sampling extent. The algorithm is as follows:

1. T_B image is generated at highest resolution possible (~10 km)
2. Elemental antenna taper is applied to the image
3. Rectangular 2-D Fourier transform applied
4. Fourier components are removed to match the GeoSTAR resolution (~50 km)
5. NEΔV noise added
6. Apodization function applied
7. Inverse 2-D Fourier transform applied
8. Inverse elemental antenna taper is applied to the image
9. Error evaluated

Figure 6.2 shows the first four processing steps, which results in the visibility product that GeoSTAR would measure. The difference between this output and the hexagonal is simply that of the sampling density.

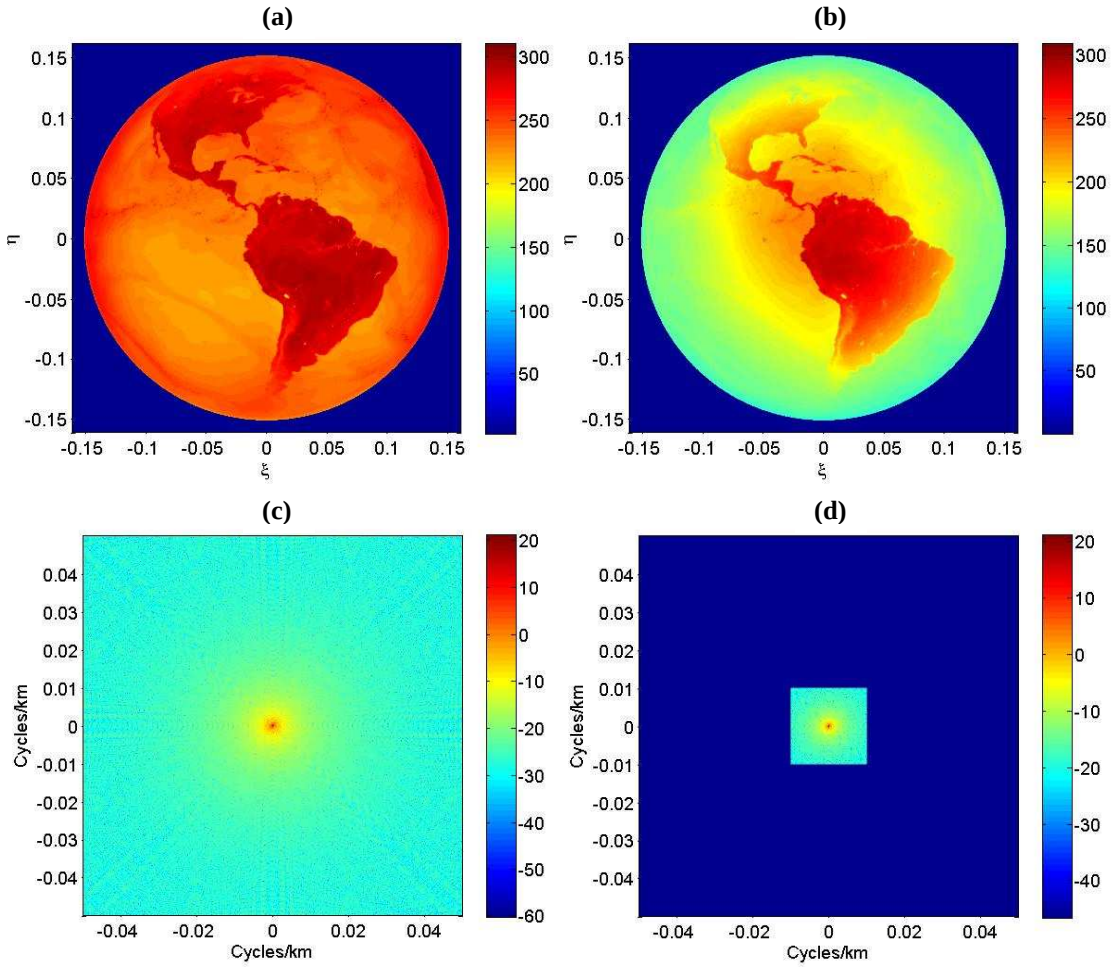

Figure 6.2: Images of the Intermediate Products Generated by the Standard Algorithm
(a) High Resolution T_B Image, 10 km [K] (b) T_B Image with Antenna Taper Applied [K]
(c) Spatial Frequency Components After 2-D FFT Application [dB]
(d) Spatial Frequency Truncation to the GeoSTAR Resolution, 50 km [dB]

Comparing Figure 6.2c and Figure 6.2d, we can see the information lost to a GeoSTAR imager due to the limited spatial frequency measurement. For the nominal processing algorithm, the apodization applied will be uniform. The impact of the NEΔV has been outlined in Section 2.1.6 and 6.1.2. To demonstrate the effects of the NEΔV visually, it is necessary to generate an extreme case where the per pixel error at ~10 K (5 second

integration). Figure 6.3 demonstrates the impact of large amounts of additive noise to the visibilities which results in speckle like noise throughout the retrieved image.

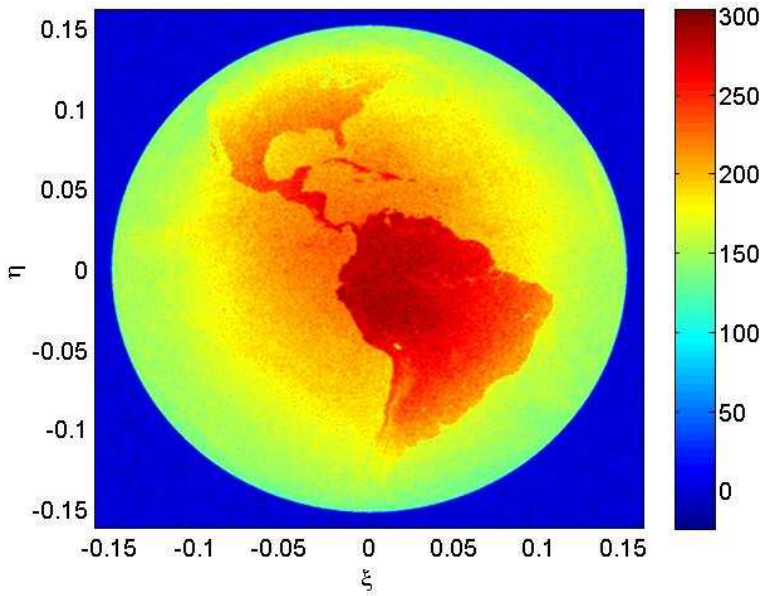

Figure 6.3: Retrieved Image with NEΔV and 5 Second Integration Time, Step 7 [K]

Side by side comparisons of the images are difficult to discern on paper without the proper resolution. Figure 6.4 shows the difference between the retrieved image and the original.

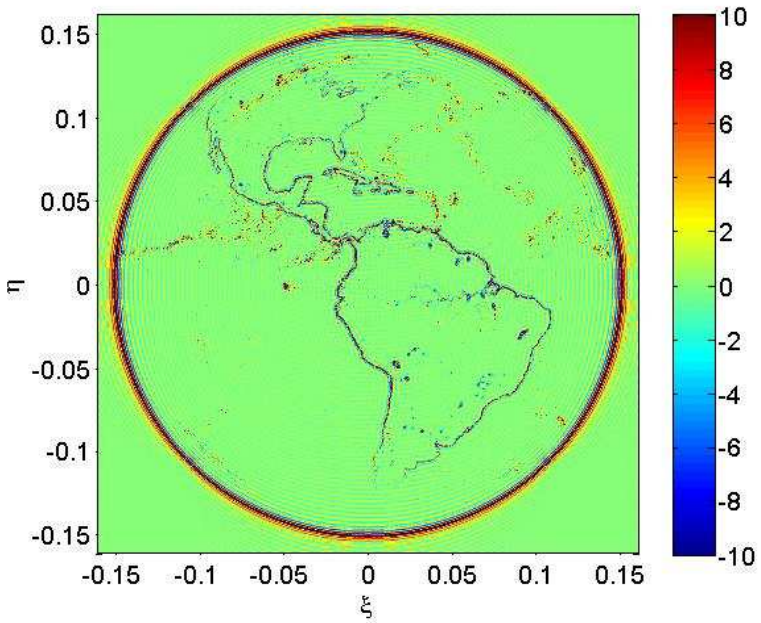

Figure 6.4: ΔT_B Image Indicating the Significant Presence of Gibbs Ringing [K]

Errors are localized around areas of large transitions, especially the Earth disk / cosmic background transition and the continental boundaries. Weather phenomena that are discontinuous events are also visible. The errors at the transitions are known as the Gibbs Phenomena, ringing artifacts that are inherent when discontinuities are represented by a finite number of terms in the Fourier series [69, 70]. In this case, the truncation of the spatial visibilities from Figure 6.2c to Figure 6.2d, leads to these artifacts. GeoSTAR will be significantly affected by the Gibbs phenomenon. While these are large errors, the Gibbs phenomenon is a known effect that can be corrected in post processing.

Another detail in Figure 6.4 is the muted continental features at the Earth limbs where the atmospheric path length is significant. The current sample images are generated for the transparent 50.3 GHz channel, and more surface features are expected to be obscured as the frequency moves towards the peak of the oxygen line. Typically, we expect that these errors, which are due to the inadequate sampling, will be largest for the transparent channels and minimal for the opaque channels.

6.2 COMPARISON TO AN IDEAL REAL APERTURE ANTENNA

A significant difference between a synthetic aperture and a real aperture are the characteristics of the antenna pattern. A synthetic aperture can have negative side lobes that alternate in sign from the main beam. The first side lobe level with a uniform taper is at 6.6 dB as opposed to the 13 dB side lobes associated with a real aperture. Figure 6.5 shows the difference between an ‘equally’ sized synthetic and real aperture. Note that equally sized means equally sized in the visibility space rather than the physical aperture.

We equate the maximum circular band limited area with a circular aperture of equivalent size.

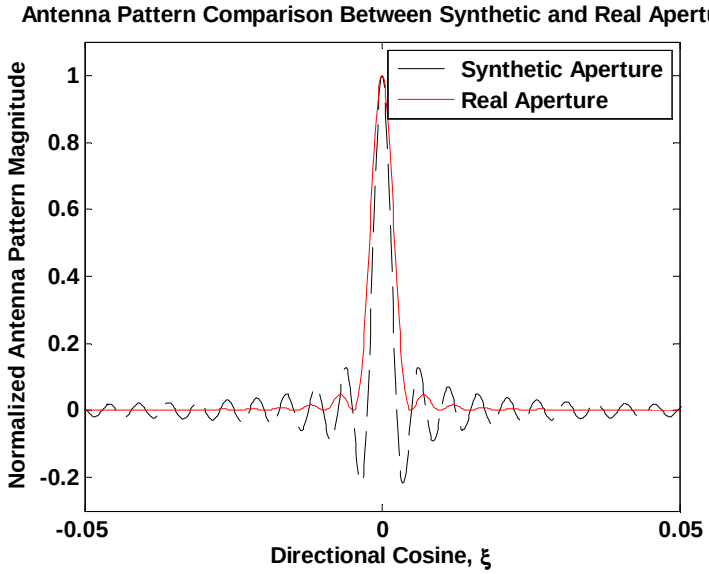

Figure 6.5: Antenna Pattern for a Uniform Synthetic and Real Aperture

The application of a triangular taper, gives the synthetic aperture 13 dB side lobes, but at the expense of the beam width [29], and in Figure 6.5, the real aperture pattern is similar to the synthetic aperture with a triangular taper.

6.2.1 CIRCULAR APERTURE ANTENNA

The normalized radiation pattern of a circular aperture is defined by [14]

$$F_n(r) = \left(2\frac{J_1(2\pi R_\lambda r)}{2\pi R_\lambda r} \right)^2 \tag{6.2}$$

Where

F_n = Normalized Radiation Pattern
J_1 = Bessel Function of the First Kind
R_λ = Aperture Radius Divided by Wavelength
r = $\sqrt{\xi^2 + \eta^2}$

and (5.1) has been modified to combine the terms for the aperture radius and the wavelength. The distribution is more commonly known as the Airy disc, and the position of the first null marks the null to null beam width of the pattern

$$\beta_{Null} = \frac{1.22}{R_\lambda} \tag{6.3}$$

The 3 dB beam width is calculated from

$$\beta_{3dB} = \frac{1}{2R_\lambda} \tag{6.4}$$

Equating (6.4) with the expression for the hexagonal angular 3 dB resolution (2.10), we arrive at the relationship between the physical parameter that defines a synthetic aperture y-array (length of the array arm in wavelengths) and the physical parameter that defines a real aperture (radius of the aperture)

$$R_\lambda = \frac{2\sqrt{3}}{\pi} D_{\lambda,\max} \approx 1.10 D_{\lambda,\max} \tag{6.5}$$

Equation (6.5) states that to produce an equivalent 3 dB beam width, a circular aperture must be larger than the synthetic aperture. This is consistent with the results that we see in Figure 6.5 where even with the same coverage in the visibility space the synthetic aperture has a smaller beam width indicating that the real aperture must be larger for an equivalent beam width.

6.2.2 REAL APERTURE PERFORMANCE

In order to evaluate the performance of the synthetic aperture, a comparison with a real aperture solution must be performed. The following analysis does not take into account the feasibility of deployment of a large real aperture antenna and the associated scanning issues, and only makes comparisons based on equivalent systems. Two real

aperture antennas will be used as points of comparison: matching the synthetic aperture beam width with a uniform apodization and a triangular apodization. Table 6.1 summarizes the parameters of interest.

Table 6.1: Antenna Parameter Comparison at 50.3 GHz

Parameter	Real Aperture 1	Synthetic Aperture Tapered	Real Aperture 2	Synthetic Aperture
$D_{\lambda,\max}$ *or* R_{λ}	327	377	416	377
Radius [m]	1.83	2.24	2.48	2.24
β_{3dB} [deg]	0.09^0	0.09^0	0.07^0	0.07^0
Side Lobe Level [dB]	13	13	13	6.7
Side Lobe Sign	Positive	Positive	Positive	Positive/Negative

The real aperture retrievals are generated by performing a 2-D convolution with the input image. The retrieved image from the synthetic aperture is generated assuming that the elemental antenna patterns are known and identical. The synthetic aperture with taper has the triangular apodization applied. Table 6.2 summarizes the values with an input image from the start of hurricane season June 2nd 2008, while Table 6.3 summarizes the values for an input image from September 1st 2008 when Hurricane Gustav made landfall.

Table 6.2: Retrieved Image Error, 06/02/2008 18:00Z

Beam	Full Image [K]	Earth Disk [K]	Region < 60^0 [K]
Real Aperture 1	10.2	8.3	2.8
SA with Δ Taper	8.5	7.0	2.4
Real Aperture 2	9.0	7.3	2.5
Synthetic Aperture	8.3	7.0	2.4

Table 6.3: Retrieved Image Error, 09/01/2008 18:00Z

Beam	Full Image [K]	Earth Disk [K]	Region < 60^0 [K]
Real Aperture 1	10.2	8.2	2.7
SA with Δ Taper	8.5	7.0	2.3
Real Aperture 2	9.0	7.3	2.4
Synthetic Aperture	8.3	6.9	2.3

Three different values are presented in Table 6.2 and Table 6.3, and errors here represent the standard deviation of the difference between the retrieved and original image. The

first column calculates the error across the whole image, including the cosmic background. The second column calculates the error for the pixels on the Earth disk only. Finally the third column calculates the error for the pixels that extend up to a maximum EIA of 60^0, where most current GOES products are deemed useful.

Both tables yield similar results; however the most notable feature is that the errors for the synthetic aperture are smaller in magnitude for a beam width of equivalent size, even with higher side lobe levels. In addition, the application of the triangular taper to the synthetic aperture seems to have little impact on the errors.

Figure 6.6 displays the error image generated by the real aperture with the matched synthetic aperture beam width. The characteristic difference between Figure 6.4 and Figure 6.6 is a product of the positive and negative side lobes of the synthetic aperture antenna pattern. The alternating sign of the side lobes of the synthetic aperture create the ripples in the image, while the positive side lobes of the real aperture generate these smoother error fields.

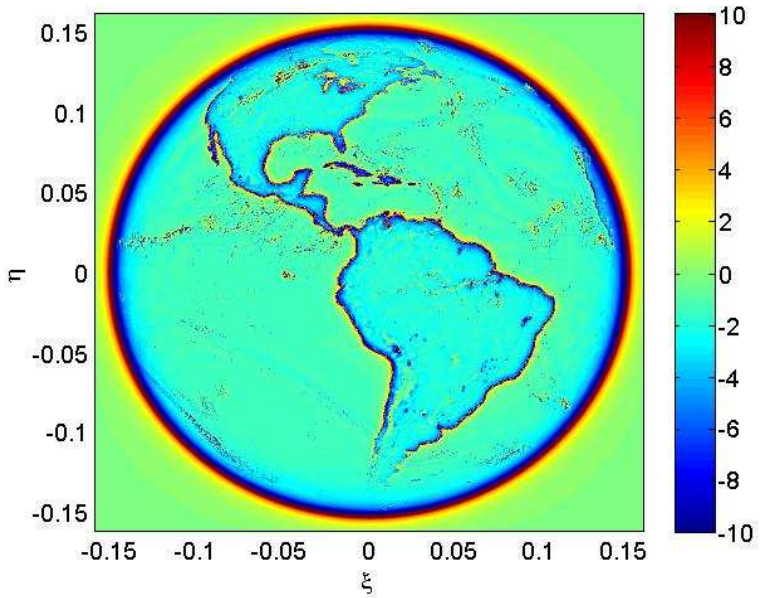

Figure 6.6: ΔT_B Generated with Real Aperture 2, Matched to the Synthetic Aperture β_{3dB} [K]

Figure 6.7 plots a transect of those errors at the Earth disk / cosmic background transition to show the qualitative difference in the types of errors that each aperture system will generate. The step function at this transition is significant and represents the largest image retrieval errors.

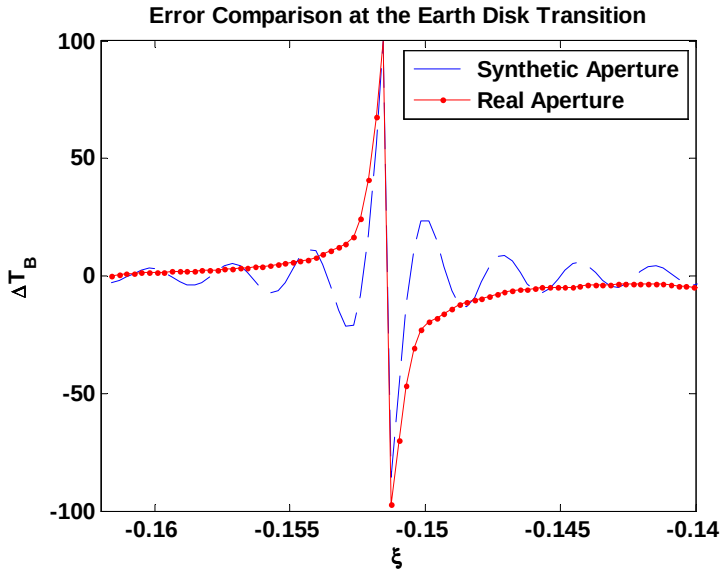

Figure 6.7: ΔT_B Comparison to Between the Synthetic and Real Aperture [K]

6.2.3 REAL APERTURE IN THE SPATIAL FREQUENCY DOMAIN

The discussion so far has taken place in the image domain, comparing the output of the different retrieval methods with the original scene. While this is the typical means of image comparison, a similar comparison can be made in the spatial frequency domain. A synthetic aperture measures the spatial Fourier transform components of a scene. The real aperture equivalent is generated by performing the Fourier transform on the scene convolved with the antenna pattern. The Fourier components generated by the real aperture can then be compared to the straight Fourier components of the high resolution image. Effectively this comparison gives us the antenna apodization function that is performed for a real aperture antenna.

Figure 6.8 shows the apodization when the magnitude of the visibility is compared with the real aperture cases as defined in Table 6.1.

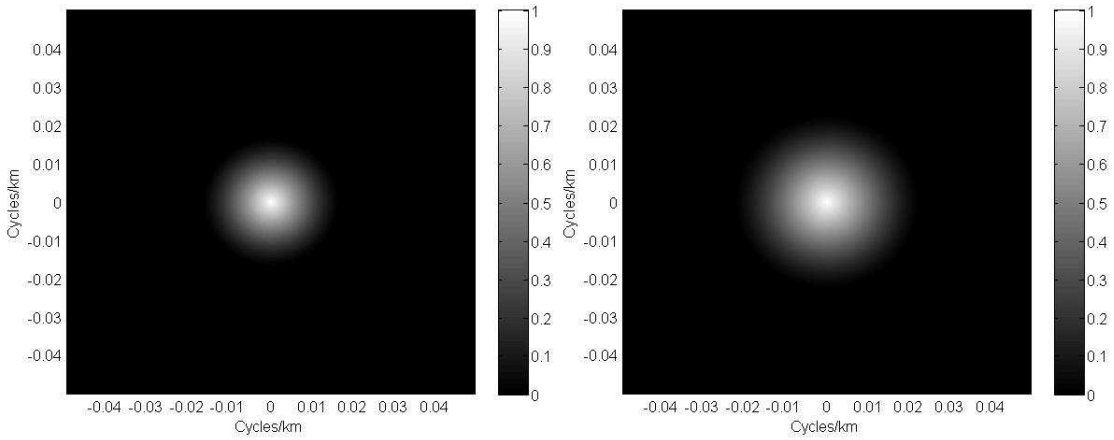

Figure 6.8: (Left) Apodization for Real Aperture 1 (Right) Apodization for Real Aperture 2

The shape of both these functions is cone-like in the visibility domain, with the broader base associated with the narrower 3 dB beam width. Table 6.4 summarizes the differences in the visibility domain.

Table 6.4: Visibility Domain Aperture Comparison

Parameter	Real Aperture 1	Synthetic Aperture	Real Aperture 2	Synthetic Aperture
Apodization	Cone	Cone	Cone	Flat
β_{3dB} [deg]	0.09^0	0.09^0	0.07^0	0.07^0
Cutoff [1/km]	0.018	0.01	0.023	0.01
Cutoff Resolution [km]	29.1	50.0	21.55	50.0

The larger coverage of the real aperture improves the smoothing of the features in the retrieved image. The surprising result here is that even with reduced coverage in the visibility domain for the synthetic aperture, the retrieval errors are still equivalent in magnitude. Figure 6.9 shows the different shapes of the apodization windows for the comparisons presented in Table 6.1, in a single dimension in the spatial frequency space.

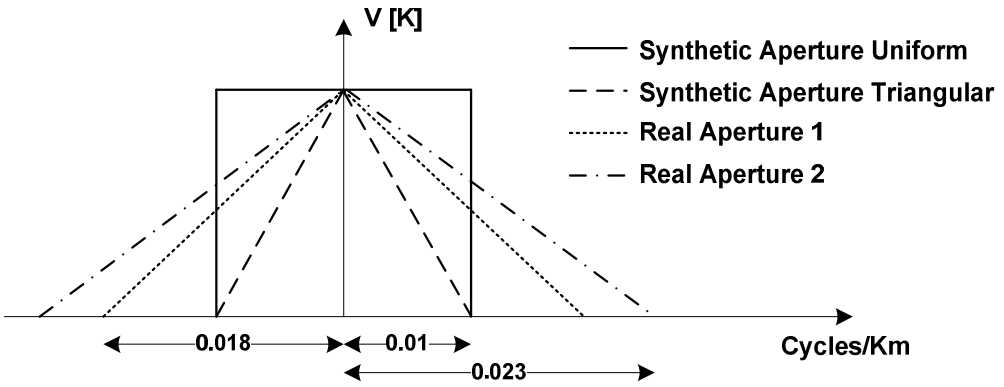

Figure 6.9: Comparison of the Different Apodization Shapes and Dimension

6.2.4 COMPARISON SUMMARY

The preceding analysis shows that with ideal systems, the performance of a synthetic aperture system is comparable to that of a real aperture system with an equally sized beam width. The analysis is performed using complex and realistic scenes typical of the expected measurement from a GOES platform. This result occurs even with the large first side lobe level of the synthetic aperture at 6.7 dB, due to the side lobe cancellation that is inherent in synthetic aperture antenna patterns. The application of a typical apodization function, often used in real aperture systems to improve performance, does not impact the image errors in a significant way for a synthetic aperture. A direct comparison between the physical parameters that define both the synthetic and real aperture shows that the synthetic aperture requires an extent that is 10% less than a real aperture, in addition to the very significant thinning of the array.

6.3 SPATIAL FREQUENCY CONTENT

One of the key products of the full disk high resolution model is a realistic model of the expected spatial frequencies that a GeoSTAR type instrument will measure in

terms of visibilities. Figure 6.10 shows a scatter plot of the typical visibility magnitudes that are expected at 50.3 GHz. The horizontal line shows the current recommended NEΔV level based on the requirements and indicates that as the unit wavelength spacing increases, a larger portion of the visibilities fall below the instrument sensitivity. This is representative of any scene that GeoSTAR expects to measure.

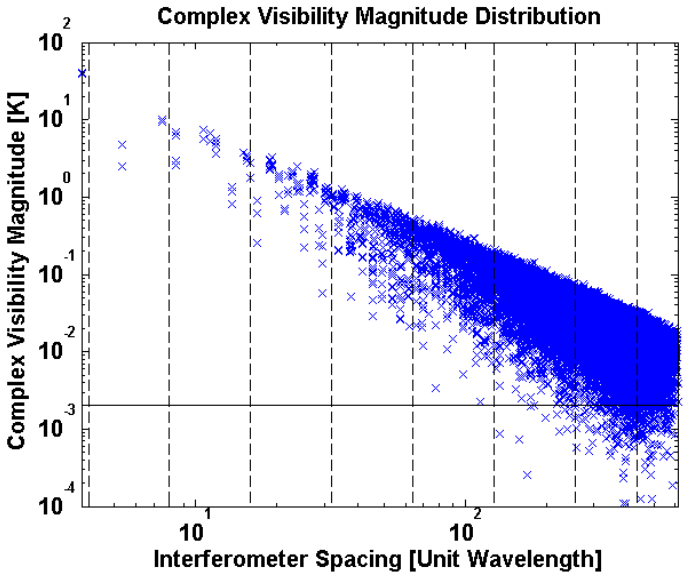

Figure 6.10: Complex Visibility Magnitude vs. Interferometer Spacing in Wavelengths, 50.3 GHz [K]

Figure 6.11 separates the real and imaginary visibilities and plots the histograms of each to show the distribution. The NEΔV level is at approximately -28 dB.

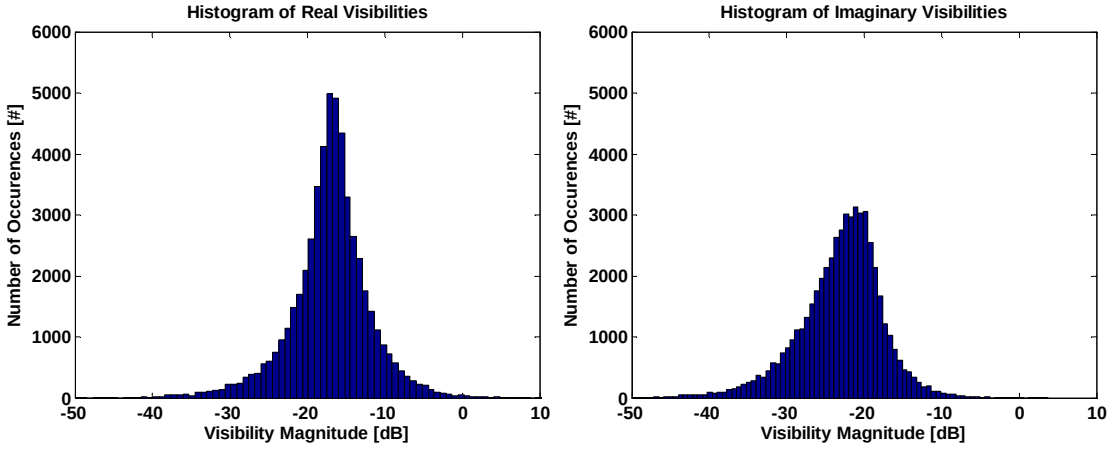

Figure 6.11: Histogram of Visibility Magnitudes at 50.3 GHz (Left) V_{Re} (Right) V_{Im}

For this particular scene, only 3% of the real visibilities are below the instrument sensitivity, while 15% of the imaginary visibilities are below the NEΔV level.

Figure 6.12 shows the histograms generated for the same scene, but at an opaque channel of 55.5 GHz. While the distribution of the real visibilities has not changed significantly, the imaginary visibilities are now skewed to the lower values.

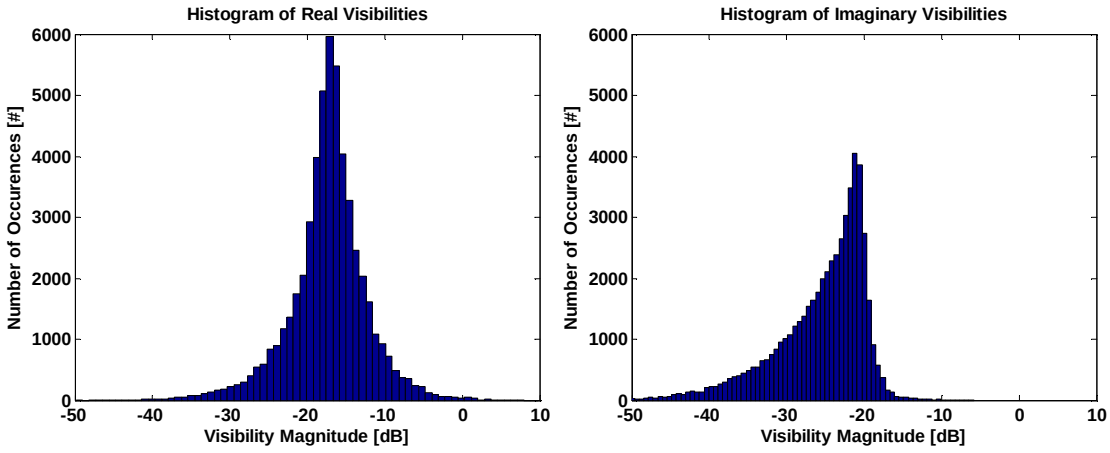

Figure 6.12: Histogram of Visibility Magnitudes at 55.5 GHz (Left) V_{Re} (Right) V_{Im}

At 55.5 GHz, 3% of the real visibilities are below the instrument sensitivity, while now 25% of the imaginary visibilities are below the NEΔV level. The skew in the imaginary components is consistent with the change in opacity as the features on the Earth surface, which are typically asymmetric, are obscured.

The following sections will take a closer look at the distribution of the visibilities in typical images and the information lost due to the measurement system.

6.3.1 EVALUATING 'UNMEASURABLE' VISIBILITIES

Given the current configuration, an evaluation must be made as to the value of these 'unmeasurable' visibilities, i.e. visibilities that have magnitudes lower than the sensitivity of the instrument. A means of performing this evaluation is to determine the error introduced to the retrieved image if these visibilities were simply discarded. In the

software, an ‘unmeasurable’ visibility is simply replaced by a ‘0’ magnitude prior to the image reconstruction. Figure 6.13 depicts the error in the reconstructed image as more visibilities are discarded. At the NEΔV level of -28 dB, only 0.093 K of error contributes to the reconstructed image. For comparison, the 55.5 GHz image has an error contribution of 0.1 K, even though there is a 10% difference in the number of imaginary visibilities below the NEΔV level.

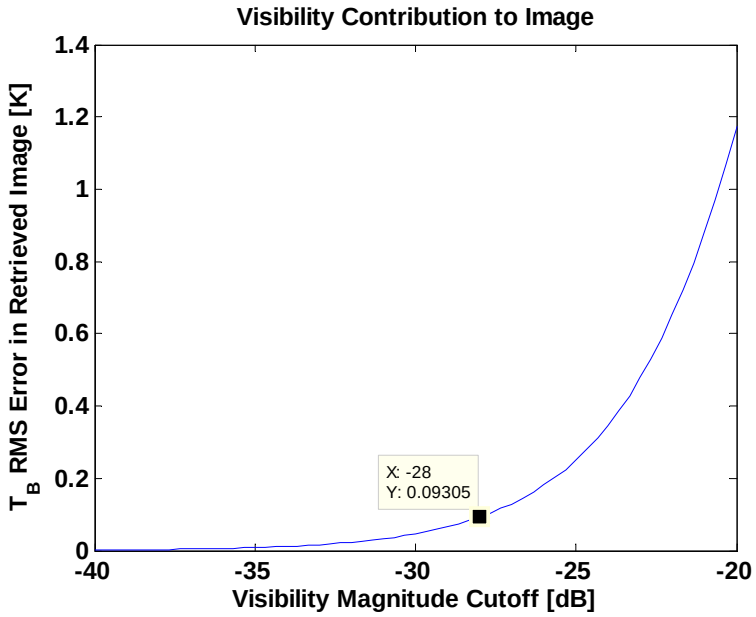

Figure 6.13: Retrieved Image Error Due to Visibilities Below the Instrument Sensitivity, 50.3 GHz

The contribution levels are minimal enough so that these effects may be ignored. Furthermore, since these levels are below the instrument sensitivity, zeroing these values will result in a roughly equivalent reduction in the noise contributions if the magnitudes are equivalent.

6.3.2 VISIBILITY MAGNITUDE VS. BASELINE SEPARATION

For the images that are generated, the magnitudes of the visibilities decrease as the baseline separation increase. Figure 6.10 shows this property clearly for the maximum values. It is difficult to interpret the data in this form, as such a division of the

visibility space is proposed similar to that used in [41] which divided the visibility space into 8 annular rings centered at the origin to evaluate the antenna gain errors. The new modified version divides the space into 10 regions - 1 region for the 'zeroth' visibility, 8 annular regions in the circular band limited area, and 1 region for all values outside of the circular band limited area – as shown in Figure 6.14. The radius of the 8 annular rings are roughly scaled in powers of 2, where each area of coverage is three times the area of the enclosed area, except for the last two regions.

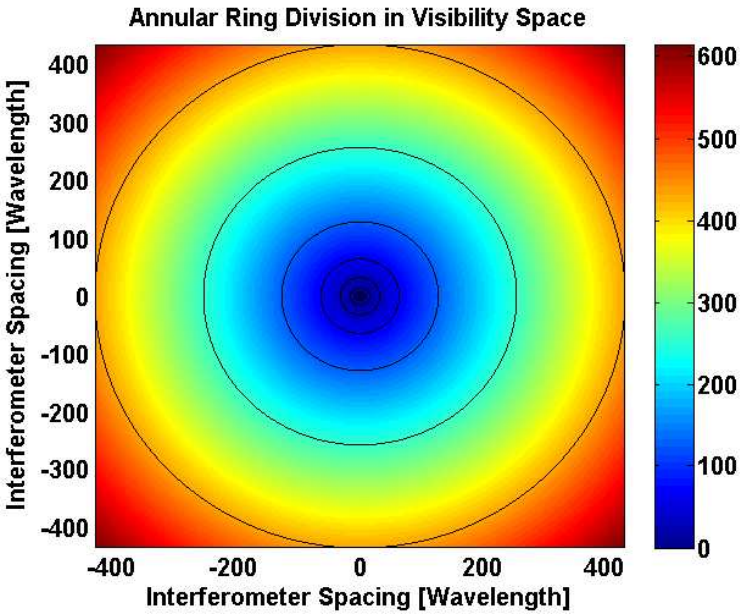

Figure 6.14: Interferometer Baseline Spacing Division into Annular Rings [Unit Wavelengths]

Table 6.5 shows the information obtained utilizing this scheme with the baseline separation bands called out explicitly and the associated number of points with rectangular processing. Two different fields are presented for both the real and imaginary visibilities. The root mean square (RMS) value of these visibilities gives us the quadratic mean of the visibilities and an idea of the received signal strength in these bands. The standard deviation of the absolute value gives an idea of the spread of these values.

Table 6.5: Sample 50.3 GHz Visibilities Divided into the Annular Regions

Baseline Separation (λ)	Count (#)	Fraction (%)	RMS V_{Re} (K)	STD $\|V_{Re}\|$ (K)	RMS V_{Im} (K)	STD $\|V_{Im}\|$ (K)
0	1	0.002	128.7	-	0.00	-
(0,4]	4	0.007	39.9	0.49	1.66	0.87
(4,8]	8	0.01	6.99	3.85	2.10	0.27
(8,16]	48	0.09	4.21	1.97	0.84	0.61
(16,32]	164	0.31	1.55	0.74	0.29	0.20
(32,64]	664	1.2	0.49	0.27	0.105	0.07
(64,128]	2708	5.1	0.18	0.10	0.041	0.027
(128,256]	10864	20.4	0.063	0.034	0.017	0.011
(256,434]	27072	50.7	0.024	0.012	0.008	0.005
(434,Max]	11828	22.2	0.014	0.007	0.006	0.004

Examining the values for the RMS and STD of V_{Im}, the low magnitudes coupled with the large variation values at the larger baseline separation explains the large number of points (15%) reported to be below the NEΔV level.

Table 6.6 is generated for the same scene at 55.5 GHz, representing the scene with significantly less variability. These two cases represent the scenes with the most and least variability for measurements with GeoSTAR.

Table 6.6: Sample 55.5 GHz Visibilities Divided into the Annular Regions

Baseline Separation (λ)	Count (#)	Fraction (%)	RMS V_{Re} (K)	STD $\|V_{Re}\|$ (K)	RMS V_{Im} (K)	STD $\|V_{Im}\|$ (K)
0	1	0.002	118.6	-	0.00	-
(0,4]	4	0.007	36.5	0.32	0.17	0.027
(4,8]	8	0.01	6.88	4.56	0.16	0.079
(8,16]	48	0.09	3.82	1.40	0.12	0.077
(16,32]	164	0.31	1.31	0.59	0.05	0.034
(32,64]	664	1.2	0.43	0.23	0.026	0.017
(64,128]	2708	5.1	0.16	0.08	0.012	0.007
(128,256]	10864	20.4	0.056	0.029	0.007	0.004
(256,434]	27072	50.7	0.022	0.011	0.005	0.003
(434,Max]	11828	22.2	0.013	0.006	0.004	0.003

Figure 6.15 plots the RMS values from Table 6.5 showing the distribution with increasing baseline spacing and the separation between V_{Re} and V_{Im}.

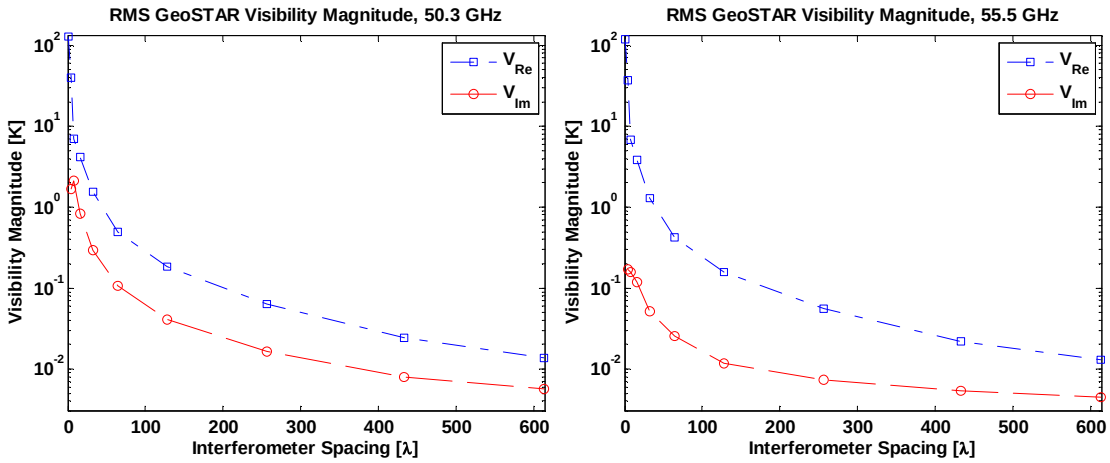

Figure 6.15: Plot of RMS Visibility Magnitude (Left) Table 6.5, 50.3 GHz (Right) Table 6.6, 55.5 GHz

Finally, as a means to evaluate the necessity of performing measurements at these larger baselines, the root sum square (RSS) of the visibility magnitude is calculated ($RSS = RMS * \sqrt{Count}$) to show the contribution from each visibility band to the retrieved image. Table 6.7 summarizes the values at the start of Hurricane season June 2nd 2008, while Table 6.8 summarizes the values for September 1st 2008 when Hurricane Gustav made landfall.

Table 6.7: RSS of Visibilities, Start of Hurricane Season (06/02/2008, 18:00Z)

Baseline Separation (λ)	Count (#)	Fraction (%)	RSS V (K) 50.3 GHz	RSS V (K) 52.8 GHz	RSS V (K) 55.5 GHz
0	1	0.002	128.1	135.9	118.1
(0,4]	4	0.007	79.3	85.3	72.5
(4,8]	8	0.01	20.1	22.2	19.2
(8,16]	48	0.09	29.5	30.2	26.4
(16,32]	164	0.31	20.1	18.6	17.0
(32,64]	664	1.2	12.9	11.8	11.0
(64,128]	2708	5.1	9.8	8.9	8.4
(128,256]	10864	20.4	6.8	6.1	5.9
(256,434]	27072	50.7	4.2	3.9	3.8
(434,Max]	11828	22.2	1.6	1.5	1.5

Table 6.8: RSS of Visibilities, Hurricane Gustav Landfall (09/01/2008, 18:00Z)

Baseline Separation (λ)	Count (#)	Fraction (%)	RSS V (K) 50.3 GHz	RSS V (K) 52.8 GHz	RSS V (K) 55.5 GHz
0	1	0.002	128.7	136.5	118.6
(0,4]	4	0.007	79.8	85.7	73.0
(4,8]	8	0.01	20.6	22.4	19.5
(8,16]	48	0.09	29.7	30.4	26.5
(16,32]	164	0.31	20.3	18.8	16.7
(32,64]	664	1.2	12.9	11.8	11.0
(64,128]	2708	5.1	9.8	8.8	8.3
(128,256]	10864	20.4	6.8	6.1	5.9
(256,434]	27072	50.7	4.2	3.8	3.7
(434,Max]	11828	22.2	1.6	1.5	1.5

The results from Table 6.7 and Table 6.8 indicate that with the current array geometry at the largest baselines, there exists information to be measured in all the regions, with contributions larger than the 1 K level.

6.4 MITIGATION OF GIBBS PHENOMENA

Figure 6.4 demonstrated that the largest errors in a synthetic array are from the known effects of the Gibbs phenomenon, where ringing artifacts occur at areas with sharp transitions. Mitigation of this phenomenon was demonstrated in Chapter 4 (give specific section). The following applies the differential algorithm to the model scenes. The test scene of interest will be from the landfall of Hurricane Gustav on September 1st 2008 at 18:00Z. Figure 6.16 shows the visible image as captured by GOES-East showing various cyclonic formations.

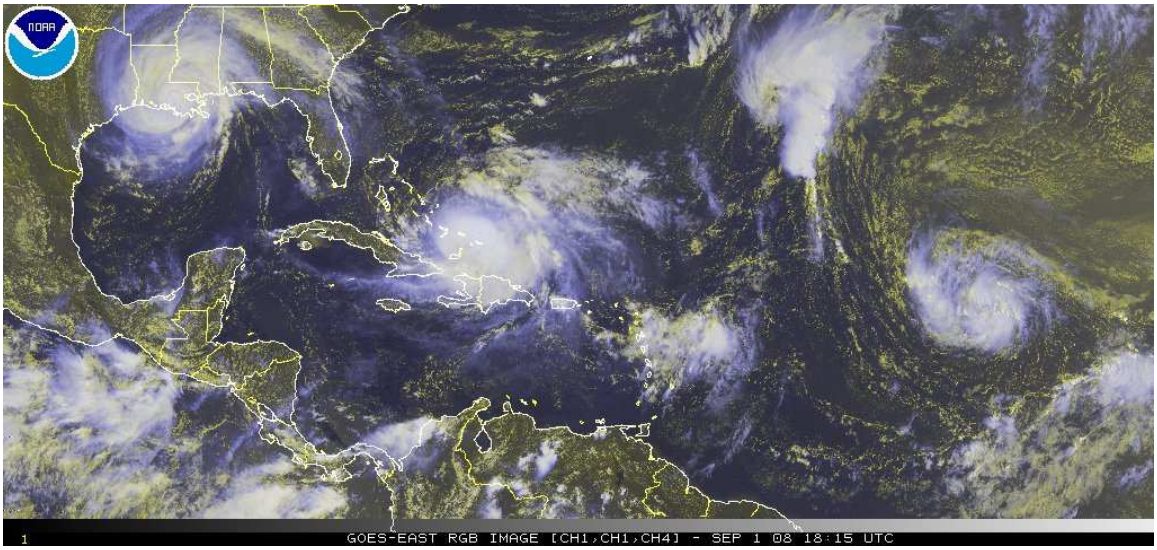

Figure 6.16: Hurricane Gustav Landfall with Hurricane Hanna over Haiti and Tropical Storm Ike in the Atlantic Ocean, GOES-E RGB Image (09/01/2008, 18:00Z)
Courtesy of the NOAA Satellite and Information Services

Figure 6.17 shows the corresponding model output image at 50.3 GHz. The color bar is scaled to accentuate the features over the oceans, especially weather cells in the Atlantic.

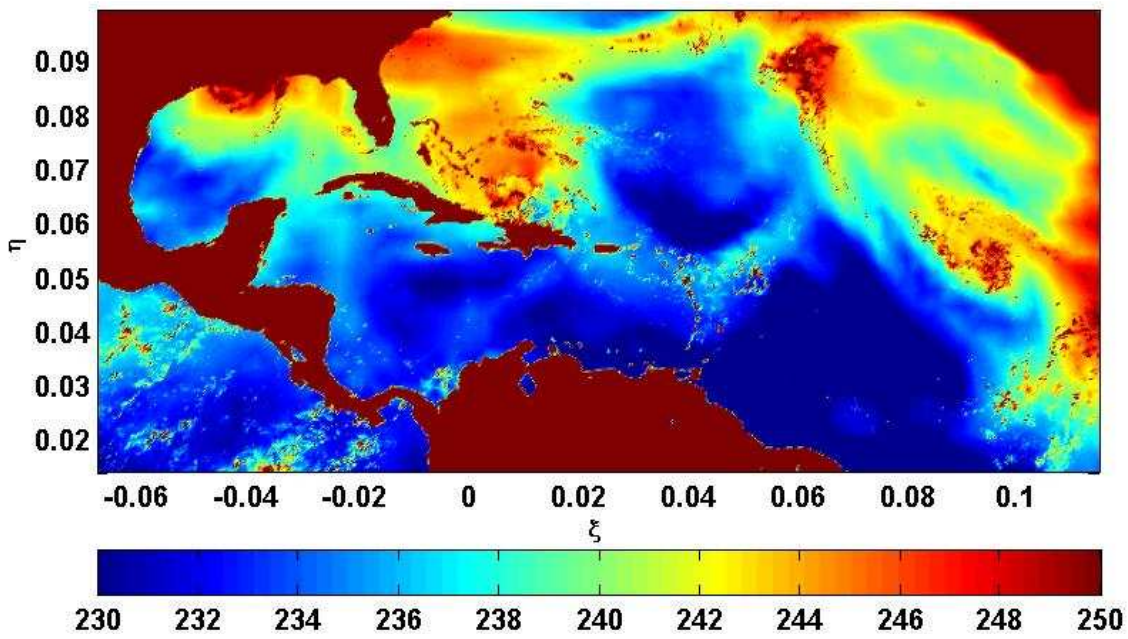

Figure 6.17: High Resolution Model Output at 50.3 GHz [K] (09/01/2008, 18:00Z)

Two differential methods will be presented, the first taking the simplistic case of a mean Earth disk and the second, a more complicated Earth disk initialized with GDAS fields,

but no clouds.

6.4.1 STANDARD PROCESSING

Figure 6.18 shows the output from the standard processing as presented in Section 6.1.3 and Gibbs ripples are evident throughout the image. Note that the differences between the uniform and the triangular apodization are minimal. The Gibbs ripples with the triangular apodization are smaller in magnitude, spread out and difficult to discern in Figure 6.18.

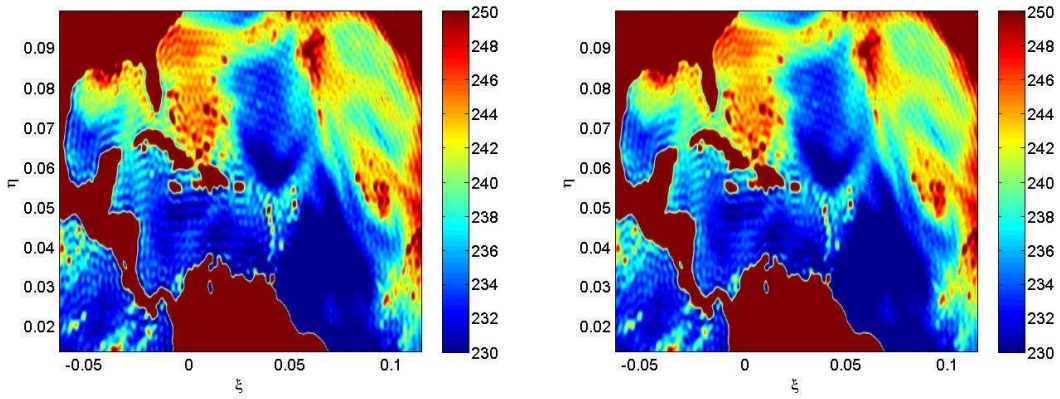

Figure 6.18: Standard Processing, (Left) Uniform and (Right) Triangular Apodization [K]

6.4.2 DIFFERENTIAL PROCESSING – MEAN EARTH DISK

The mean Earth disk temperature is selected as the temperature at the limb to match the magnitude of the transition with the cosmic background. Figure 6.19 shows the results of the differential processing where most of the ripples in the eastern Atlantic Ocean have been removed. While this processing is crude, the impact is still noticeable since the ringing from the Earth disk transition is the most significant error in the image. Ringing artifacts at the coastlines are still prominent with this processing algorithm.

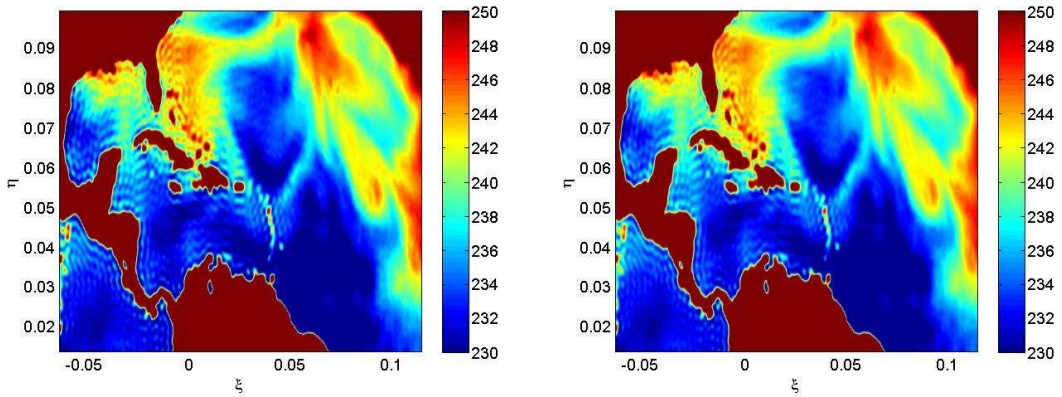

Figure 6.19: Differential Processing – Mean Earth Disk, (Left) Uniform and (Right) Triangular Apodization [K]

6.4.3 DIFFERENTIAL PROCESSING – GDAS ATMOSPHERE

A more complex model that can be applied utilizes the GDAS atmosphere. The a priori atmosphere will account for the impact of the increasing atmospheric path lengths, and the associated masking of the surface features. Figure 6.20 shows that the majority of the ringing artifacts have been removed, even those at the coastlines.

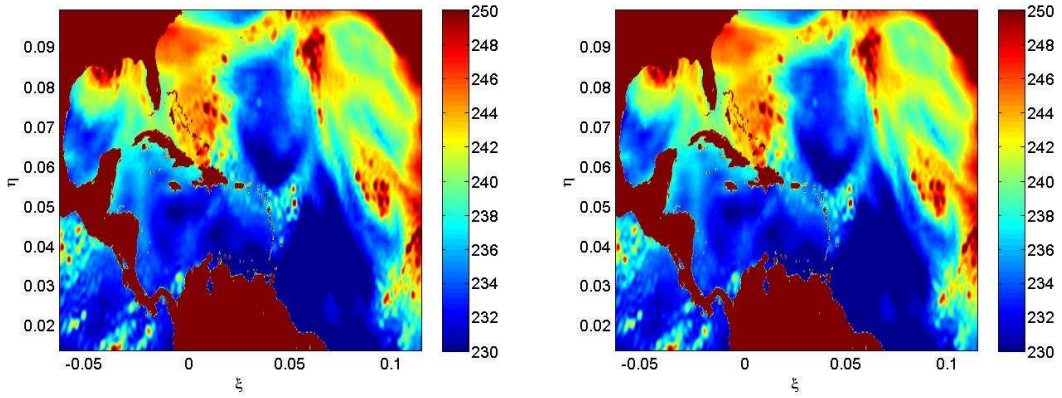

Figure 6.20: Differential Processing – GDAS Atmosphere, (Left) Uniform and (Right) Triangular Apodization [K]

Figure 6.21 shows a small portion of the equatorial transect with a localized land hot spot (the Galapagos Islands). With standard processing, the peak magnitude is not well retrieved, and ringing occurs around this feature. With differential processing, these

features are well retrieved since they occur in the a priori dataset. Image features that are smaller than the resolution of the imager are not retrieved.

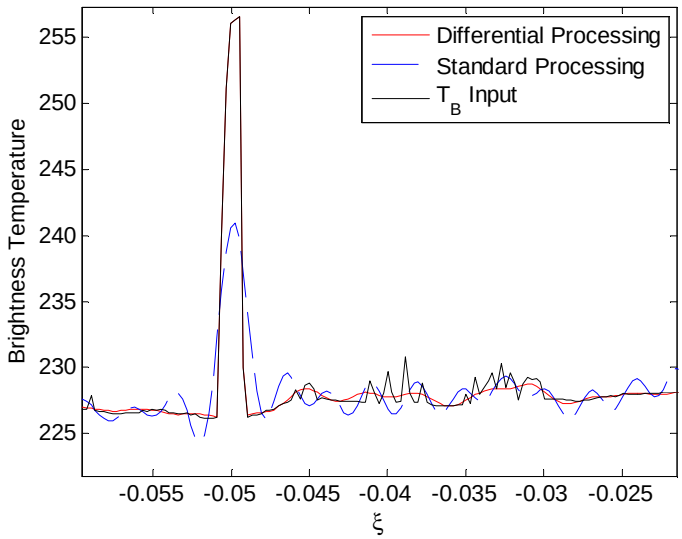

Figure 6.21: Magnified Area of an Equatorial Transect Showing the Reduction in Ringing [K]

6.4.4 IMAGE RETRIEVAL ERROR SUMMARY

Table 6.9 summarizes the image errors with the same pixel ranges as defined in Section 6.2.2. In addition to the three cases already defined, a fourth case is added with non-ideal conditions where the atmospheric model derived from GDAS does not match the day for which retrieval is made. The GDAS fields used in this case were generated three months prior, with the associated surface emissivity parameters. The only condition held the same was the hour of observation.

Table 6.9: Retrieval Errors Comparing Various Methods, 50.3 GHz (09/01/2008 18:00Z)

Processing Method	Uniform Taper [K]			Triangular Taper [K]		
	Full Image	Earth Disk	$< 60^0$	Full Image	Earth Disk	$< 60^0$
Standard	4.62	3.98	1.87	4.72	4.01	1.90
Earth Disk	1.43	1.71	1.83	1.46	1.75	1.87
GDAS Atmosphere	0.83	1.00	0.93	0.83	1.00	0.94
GDAS Mismatch	0.86	1.04	0.98	0.87	1.05	0.98

The quantitative results show that the matched GDAS atmosphere produces the best results, significantly better that that of the simple mean Earth disk. The results from a mismatched atmosphere show that errors are slightly larger, but still significantly smaller than those produced without an a priori atmosphere. The operational mode for GeoSTAR could then use GDAS NWP outputs as the initialization atmosphere since the degradation from the results of a mismatched atmosphere are minimal while reducing the magnitude of the Gibb's ringing significantly. Additional candidates for the model atmosphere include the average monthly atmospheric state and the seasonal atmospheric state.

6.4.5 DIFFERENTIAL PROCESSING – VISIBILITY MAGNITUDE

Differential processing is not without its pitfalls. By differencing the measured scene with a known modeled atmosphere, most of the variability in the image is removed and replaced by deviations from the modeled atmospheric state. Figure 6.22 shows the difference image generated with a matched and a mismatched GDAS atmosphere with no additive noise added. Errors in the matched state show primarily the structure due to the clouds and precipitation, while with the mismatched atmosphere, differences in the surface and atmospheric state are apparent. Both images in Figure 6.22 are generated on the same color scale showing that there is significantly more variation in the mismatched atmosphere as expected.

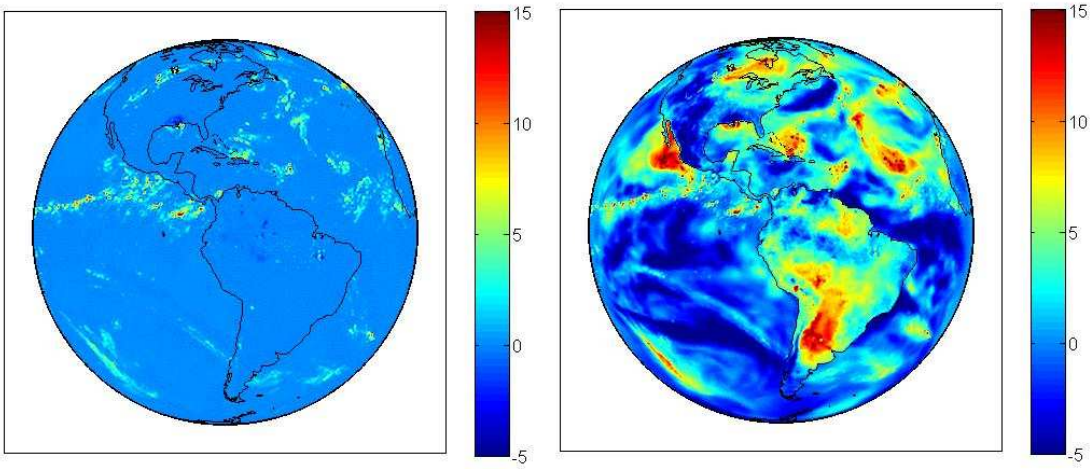

Figure 6.22: ΔT_B Using a GDAS (Left) Matched (Right) Mismatched Atmosphere 50.3 GHz [K] (09/01/2008, 18:00Z)

Comparing the complex visibility magnitude in the regions that were previously defined in Section 6.3.2 and plotting the RMS values of the complex visibility magnitude in Figure 6.23, we can directly see the impact of noise in the differential measurements.

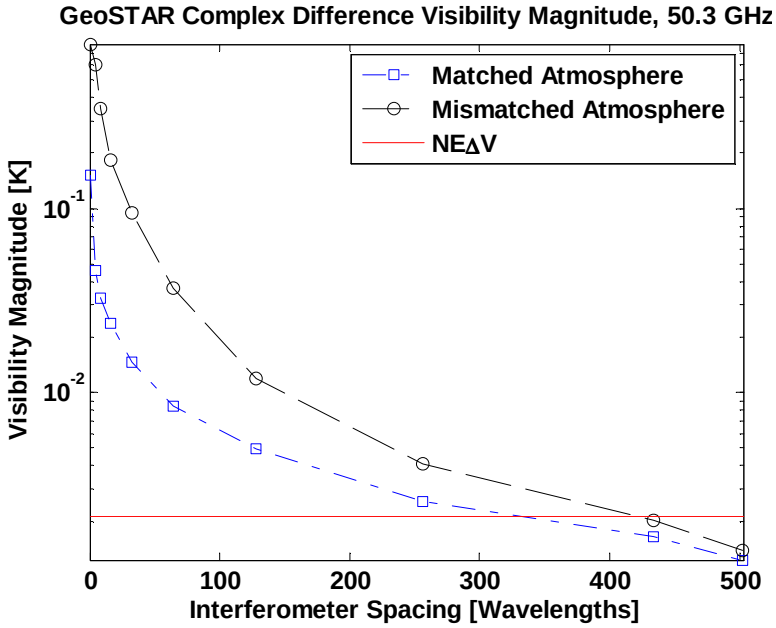

Figure 6.23: RMS of the Complex Visibility Magnitude for Different Modeled Atmospheric States 50.3 GHz [K] (09/01/2008, 18:00Z)

Caution must be taken in the interpretation of the difference images as the noise effects will be clearly visible, compared to that generated in Figure 6.3 which required an order of magnitude larger NEΔV contribution before the speckle became apparent.

6.4.6 A MODIFIED CLEAN ALGORITHM

The removal of residual Gibb's artifacts has been investigated with respect to radio astronomy sources using deconvolution procedures, the most successful of which is called the CLEAN algorithm. Developed by Högbom [89] in the early 1970s, the algorithm is well suited for determining the position and magnitude of point sources in an empty field of view. A discussion on this and other deconvolution algorithms can be found in Thompson [27]. Camps *et al.* [71] investigated the suitability of this algorithm for SMOS retrievals and found that the algorithm extended with differential methods can be used for operation with extended sources. The major difference between radio astronomy scenes and the differential scenes produced in this section is that differential scenes can have a negative magnitude, and the algorithm must be modified to account for this. The following definitions are used in the algorithm:

- The 'dirty map' is the difference image generated from the differential processing algorithm, $\Delta\hat{T}_B$
- The absolute 'dirty map' is a version of the 'dirty map' where the magnitudes are absolute to deal with the negative magnitudes, $\left|\Delta\hat{T}_B\right|$
- The 'dirty beam' is the synthetic aperture pattern (point spread function) of the STAR, A_{PSF}
- The 'clean beam' response is chosen as a Gaussian with a half amplitude width equal to that of the 'dirty beam', A_{CLEAN}
- Intensity steps are defined in units of pixel noise, where the pixel noise is the standard deviation of the nadir pixel due to the additive NEΔV, $\hat{T}_{B,NE\Delta V}$
- $\hat{T}_{B,Max}$ is the maximum deviation in the map and the starting point for the algorithm

The modified algorithm is as follows, where *i* represents the iteration number:

1. Find the points in the absolute 'dirty map' that are within the range $\hat{T}_{B,Max}$ and $\hat{T}_{B,Max} - i.\hat{T}_{B,NE\Delta V}$
2. Find the corresponding location in the 'dirty map' and store the position and magnitude of the points in an array, $\hat{T}_{DF,i}$
3. Generate the residual 'dirty map' by taking the difference of the original dirty map and the convolution of the points with the 'dirty beam', $\Delta\hat{T}_{B,i+1} = \Delta\hat{T}_{B,i} - \hat{T}_{DF,i} \otimes A_{PSF}$
4. Iterate 1 to 3 till the processing range falls below twice the pixel noise level, $\hat{T}_{B,Max} - i.\hat{T}_{B,NE\Delta V} \leq 2.\hat{T}_{B,NE\Delta V}$
5. The delta function map is extracted from $\hat{T}_{DF,i}$ by taking the largest deviation for each pixel (either positive or negative)
6. The final image is generated by convolving the delta function map with the 'clean beam' and adding the final 'dirty map' (known as the residual map), $\hat{T}_{B,CLEAN} = \hat{T}_{DF,Max,i} \otimes A_{CLEAN} + \Delta\hat{T}_{B,i+1}$

The algorithm is first applied to an image with no noise. The differential method chosen utilizes a matched GDAS atmosphere. Matching the atmosphere allows the differential map to closely resemble quasi-point sources in an empty field of view as clearly demonstrated in Figure 6.22. Figure 6.24 shows the comparison of a scene before and after the application of the modified CLEAN algorithm reduced to the area defined in Figure 6.16, with several hurricanes in the image.

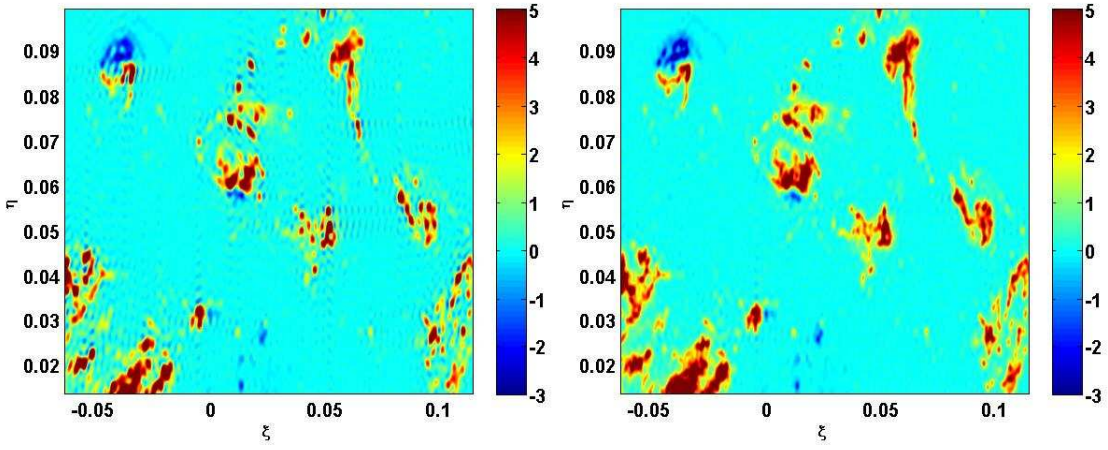

Figure 6.24: GDAS Matched Atmosphere (Left) $\Delta\hat{T}_B$ (Right) $\hat{T}_{B,CLEAN}$ (50.3 GHz, 09/01/2008 18:00Z) [K]

Prior to the application of the deconvolution algorithm, ringing due to the atmospheric transition is still visible. After the modified CLEAN algorithm is applied, most of the ringing artifacts have been removed and visually the map is significantly 'cleaner'.

Figure 6.25 shows the same scene comparison with NEΔV added. Since the magnitude of the Gibb's artifacts due to the atmospheric features are often small and below the pixel level noise, it is difficult to discern the impact visually. Regardless, from Figure 6.24, we do know that the small leveled structured ringing has been removed increasing the accuracy of the measurement.

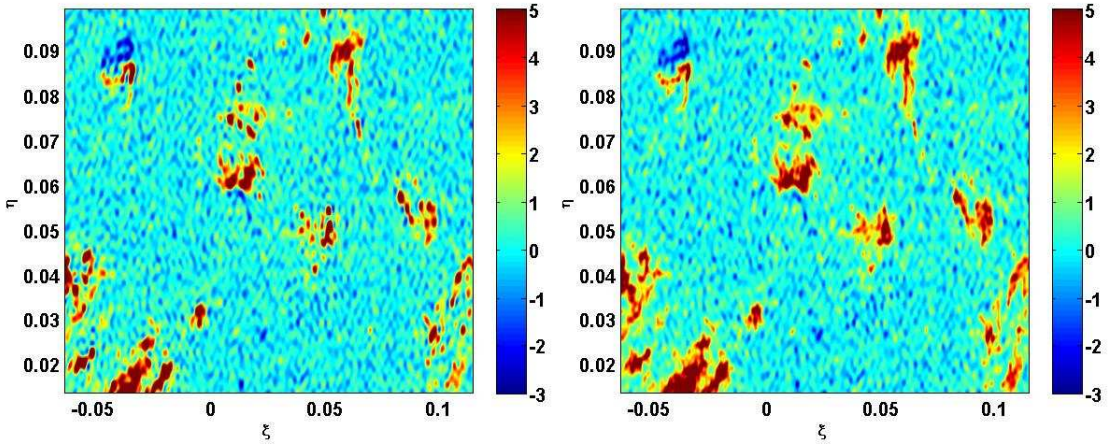

Figure 6.25: GDAS Matched Atmosphere, NEΔV Added (Left) $\Delta\hat{T}_B$ (Right) $\hat{T}_{B,CLEAN}$ (50.3 GHz, 09/01/2008 18:00Z) [K]

The algorithm as defined is not meant to be a rigorous representation of the effectiveness of a CLEAN type algorithm to remove the residual Gibbs artifacts, but meant to demonstrate qualitatively the performance of an equivalent algorithm. The CLEAN tuning parameters (e.g. gain and damping) are not optimized in any manner. However, with simple modifications, it appears that CLEAN can be applied to remove

the finer Gibbs artifacts; it will be difficult to discern the impact in the final instrument due to the noise levels.

6.4.7 REAL APERTURE COROLLARY

The reduction of the Gibbs artifacts improves the performance of the interferometric radiometer by reducing the inherent errors due to the measurement method. For a real aperture system, a similar procedure is performed, often times called the antenna pattern correction (APC) algorithm. This type of algorithm has been applied to reduce the antenna polarization [90] and antenna side lobe [91] contamination since the 1970's. APC algorithms are an integral part of the calibration of any on-orbit radiometer; recent examples include the Ocean Topography Experiment (TOPEX) [92], the Jason Microwave Radiometer (JMR) [93] and the Environmental Satellite (Envisat) [94]. Both measurement types, real and synthetic, have methods available to them to reduce inherent measurement errors.

6.5 SUMMARY

An instrument simulator has been developed to transform T_B images into expected measurements that a GeoSTAR type instrument would measure at the 50 GHz temperature sounding channels. The simulator differs from the actual instrument as sampling is performed in rectangular coordinates to simplify processing; however, this will have little impact on the results for our purposes as statistical averages are used as opposed to specific magnitude results.

The information content of measurements at 50 GHz is evaluated with respect to the expected instrument design. The variation is found to be smaller at the opaque

channels compared to the window channels as expected. Dividing the measurement areas into circular zones, each zone contributes a significant amount of signal to the retrieved image, including the zone outside the circular band limited area. The magnitude of the imaginary part of the visibility is much smaller than the real part.

The standard processing algorithm is defined and the performance compared to a real aperture system. The performance is found to be excellent and the impact of apodization on the synthetic aperture is minimal. Large scale Gibbs Phenomena can be reduced by performing differential measurements utilizing an a priori model. Several simple models are evaluated and the best suited appears to be that of a matched atmosphere, though it is demonstrated that even using a mismatched atmosphere reduces the errors. The residual Gibbs artifacts due to the atmospheric features can be reduced further using a CLEAN type algorithm, and this is demonstrated qualitatively.

CHAPTER 7

CONCLUSIONS

7.1 BRIEF REVIEW

The Precipitation and All-Weather Temperature and Humidity (PATH) mission outlined in the decadal survey for launch in 2016-2020 recommends a microwave array spectrometer as the instrument payload. A design for the Geostationary Synthetic Thinned Aperture Radiometer (GeoSTAR) is presented fulfils all but one of the mission requirements – integration time – and tradeoff options are available to meet this requirement. A technological roadmap is available for the development of the key hardware components, especially with respect to the receiver and digital correlator design.

The fabrication of the demonstrator, GeoSTAR-D, contributed significantly to the hardware development (receivers, antennas, correlators) and provided a test-bed to verify the theoretical understanding of a two-dimensional STAR. Measurements in the anechoic chamber provided a boresight phase calibration and verified that the antenna patterns matched the theoretical model. Deployment of the instrument with an engineered Earth disk model allowed for generation of GEO like measurements and calibration validation. The theoretical based image retrieval algorithm was implemented and combined with models to account for the sky aliases and the target discontinuities.

The images generated after sky alias removal and Gibbs mitigation had residual errors of less than 2%.

A high resolution Earth disk model is generated from existing publically available datasets, the appropriate geophysical parameter models and a full radiative transfer model. The model allows for the generation of un-physically realizable scenes to determine the impact of individual geophysical parameters on the observed brightness temperature. The realistic brightness temperature images are then evaluated with a GeoSTAR-like instrument simulator to investigate the effectiveness of apodization, spatial frequency information content and various processing algorithms. The recommended retrieval algorithm performs well even when based on imperfect input models.

7.2 CONTRIBUTIONS

- The theoretical framework of a two dimensional STAR is presented with specific application to GeoSTAR, with an available trade space to fulfill the requirements for deployment on a GOES platform.
- Boresight phase calibration of GeoSTAR-D is performed in the anechoic chamber, and successfully applied to future measurements in combination with a traditional two point external calibration with ambient and liquid nitrogen targets.
- An addition pointing correction is applied to the calibration by examining the deviations of the measured phase from the theoretical of antenna pairs separated only in ξ or η. The correction results in the removal of a significant temperature gradient in the mesa measurements.

- An Earth disk target parameter extraction algorithm is created that solves for the various physical parameters of the target relative to the instrument.
- An image retrieval algorithm based on the theoretical formulation of the G-Matrix is shown to produce images with the expected contrast. This algorithm, combined with models of the sky background and target temperatures, is capable of generating fully calibrated images with less than 2% error.
- A high resolution full Earth disk model is created that generates realistic brightness temperature images at the temperature sounding frequencies.
- The information content available to a GeoSTAR type instrument at 50 GHz is evaluated and significant signal is available at the high spatial frequencies to merit measurement.
- Retrieved image errors are on par with traditional ideal real aperture systems, even with imperfect inputs to the retrieval algorithms. Further reduction in errors can be obtained by suitable extension of a CLEAN type algorithm.

7.3 FUTURE WORK

The following represents a partial list of topics to be investigated in the future.

7.3.1 REDUCING THE GEOSTAR INTEGRATION TIME

Currently the integration time falls short of the requirements generated from AMSU and even more stringent requirements are proposed for the PATH mission with images generated half hourly. The design trade space should be examined closely to determine how this can be achieved. Increasing the quantization levels decreases

integration times, but not to the required levels. An effective topology that allows for increased antenna gain is promising [40], but other options should be investigated.

7.3.2 Full Inter-Element Correction of the Theoretical G-Matrix

The difference between the theoretical model and experimental measurements made in the anechoic chamber should be examined further to correct for the inter-element variations. This correction must be extracted carefully such that the known range imperfections are accounted for and not embedded in the calibration.

7.3.3 Sun Transit Effects

Sun transit measurements from the mesa show significant image aliasing effects within the field of view. GeoSTAR will be directly affected, and a mitigation algorithm should be developed and implemented to demonstrate that the sun alias can be removed from the Earth disk.

7.3.4 Extension of the Earth Model to 183 GHz

A scattering model should be integrated with the high resolution full Earth disk model so that the results will be valid at 183 GHz. This will allow for realistic images due to ice scattering and even improve the performance at 50 GHz. The information content of the expected images and retrieval strategies can then evaluated in a similar manner to that performed in Chapter 6.

References

[1] R. Newton and J. Rouse, Jr., "Microwave radiometer measurements of soil moisture content," *Antennas and Propagation, IEEE Transactions on*, vol. 28, pp. 680, 1980.

[2] G. C. Thomann, "Experimental Results of the Remote Sensing of Sea-Surface Salinity at 21-cm Wavelength," *Geoscience Electronics, IEEE Transactions on*, vol. 14, pp. 198, 1976.

[3] P. Gloersen and F. Barath, "A scanning multichannel microwave radiometer for Nimbus-G and SeaSat-A," *Oceanic Engineering, IEEE Journal of*, vol. 2, pp. 172, 1977.

[4] V. G. Irisov, A. V. Kuzmin, M. N. Pospelov, J. G. Trokhimovsky, and V. S. Etkin, "The Dependence of Sea Brightness Temperature on Surface Wind Direction and Speed. Theory and Experiment," presented at IGARSS, Helsinki, Finland, 1991.

[5] S. H. Yueh, "Modeling of wind direction signals in polarimetric sea surface brightness temperatures," *Geoscience and Remote Sensing, IEEE Transactions on*, vol. 35, pp. 1400, 1997.

[6] N. C. Grody, "Remote sensing of the atmosphere from satellites using microwave radiometry," in *Atmospheric Remote Sensing by Microwave Radiometry, Wiley series in remote sensing*, M. A. Janssen, Ed. New York: Wiley, 1993, pp. 259-334.

[7] W. P. Menzel and J. F. W. Purdom, "Introducing GOES-I: The First of a New Generation of Geostationary Operational Environmental Satellites," *Bulletin of the American Meteorological Society*, vol. 75, pp. 757-781, 1994.

[8] N. W. Association, "NWA Letter of Support for GOES-MWS," in *National Weather Digest*, 2005.

[9] J. Gurka, "GOES-R Program Requirements Document Version 1," G. O. R. W. Group, Ed.: NOAA/NESDIS, 2004.

[10] National Research Council (U.S.). Committee on Earth Science and Applications from Space., *Earth science and applications from space: national imperatives for the next decade and beyond*. Washington, DC: National Academies Press, 2007.

[11] F. J. Solman, D. H. Staelin, J. P. Kerekes, and M. W. Shields, "A microwave instrument for temperature and humidity sounding from geosynchronous orbit," presented at Geoscience and Remote Sensing Symposium Proceedings, 1998. IGARSS '98. 1998 IEEE International, 1998.

[12] B. H. Lambrigtsen, "GEO/SAMS-the Geostationary Synthetic Aperture Microwave Sounder," presented at IGARSS, Honolulu, Hawaii, 2000.

[13] M. Planck and M. Masius, *The theory of heat radiation*. Philadelphia: P. Blakiston's Son & Co., 1914.

[14] F. T. Ulaby, R. K. Moore, and A. K. Fung, *Microwave remote sensing: active and passive*. Reading, Mass.: Addison-Wesley Pub. Co. Advanced Book Program/World Science Division, 1981.
[15] J. D. Kraus, M. E. Tiuri, and A. V. Raisanen, *Radio astronomy*. Powell, Ohio: Cygnus-Quasar Books, 1986.
[16] J. B. Johnson, "Thermal Agitation of Electricity in Conductors," *Physical Review*, vol. 32, pp. 97, 1928.
[17] H. Nyquist, "Thermal Agitation of Electric Charge in Conductors," *Physical Review*, vol. 32, pp. 110, 1928.
[18] M. Tiuri, "Radio astronomy receivers," *Antennas and Propagation, IEEE Transactions on [legacy, pre - 1988]*, vol. 12, pp. 930, 1964.
[19] G. Evans and C. W. McLeish, *RF radiometer handbook*. Dedham, Mass.: Artech House, 1977.
[20] H. H. Aumann, M. T. Chahine, C. Gautier, M. D. Goldberg, E. Kalnay, L. M. McMillin, H. Revercomb, P. W. Rosenkranz, W. L. Smith, D. H. Staelin, L. L. Strow, and J. Susskind, "AIRS/AMSU/HSB on the Aqua mission: design, science objectives, data products, and processing systems," *Geoscience and Remote Sensing, IEEE Transactions on*, vol. 41, pp. 253, 2003.
[21] N. C. Grody, "Temperature Soundings from the DMSP Microwave Sounder," in *Advances in Remote Sensing Retrieval Methods*. Hampton, VA, 1985, pp. 249-265.
[22] P. W. Rosenkranz, K. D. Hutchison, K. R. Hardy, and M. S. Davis, "An Assessment of the Impact of Satellite Microwave Sounder Incidence Angle and Scan Geometry on the Accuracy of Atmospheric Temperature Profile Retrievals," *Journal of Atmospheric and Oceanic Technology*, vol. 14, pp. 488-494, 1997.
[23] A. J. Gasiewski, A. Voronovich, B. L. Weber, B. Stankov, M. Klein, R. J. Hill, and J. W. Bao, "Geosynchronous microwave (GEM) sounder/imager observation system simulation," presented at IGARSS, Toulouse, France, 2003.
[24] D. H. Staelin and C. Surussavadee, "Precipitation Retrieval Accuracies for Geo-Microwave Sounders," *Geoscience and Remote Sensing, IEEE Transactions on*, vol. 45, pp. 3150, 2007.
[25] A. J. Gasiewski, D. H. Staelin, and B. Bizzarri, "The Geosynchronous Microwave (GEM) Sounder/Imager," presented at International TOVS Study Conferences, Lorne, Australia, 2002.
[26] R. N. Bracewell, "Radio Interferometry of Discrete Sources," *Proceedings of the IRE*, vol. 46, pp. 97, 1958.
[27] A. R. Thompson, J. M. Moran, and G. W. Swenson, *Interferometry and synthesis in radio astronomy*. New York: Wiley, 2001.
[28] I. Corbella, N. Duffo, M. Vall-llossera, A. Camps, and F. Torres, "The visibility function in interferometric aperture synthesis radiometry," *Geoscience and Remote Sensing, IEEE Transactions on*, vol. 42, pp. 1677, 2004.
[29] C. S. Ruf, C. T. Swift, A. B. Tanner, and D. M. Le Vine, "Interferometric synthetic aperture microwave radiometry for the remote sensing of the Earth," *Geoscience and Remote Sensing, IEEE Transactions on*, vol. 26, pp. 597, 1988.

[30] D. M. Le Vine, M. Kao, C. T. Swift, A. Griffis, and A. B. Tanner, "Initial Results In The Development Of A Synthetic Aperture Microwave Radiometer," *Geoscience and Remote Sensing, IEEE Transactions on*, vol. 28, pp. 614, 1990.
[31] D. M. Le Vine, A. J. Griffis, C. T. Swift, and T. J. Jackson, "ESTAR: a synthetic aperture microwave radiometer for remote sensing applications," *Proceedings of the IEEE*, vol. 82, pp. 1787, 1994.
[32] A. B. Tanner and C. T. Swift, "Calibration of a synthetic aperture radiometer," *Geoscience and Remote Sensing, IEEE Transactions on*, vol. 31, pp. 257, 1993.
[33] C. Ruf, C. Principe, T. Dod, B. Gosselin, B. Monosmith, S. Musko, S. Rogacki, A. Stewart, and Z. Zhaonan, "Lightweight rainfall radiometer STAR aircraft sensor," 2002.
[34] W. L. Jones, P. Jun-Dung, J. Zec, C. S. Ruf, M. C. Bailey, and J. W. Johnson, "A feasibility study for a wide-swath, airborne, hurricane imaging microwave radiometer for operational hurricane measurements," 2002.
[35] A. Camps, J. Font, M. Vall-llossera, R. Villarino, C. Gabarro, L. Enrique, J. Miranda, I. Corbella, N. Duffo, F. Torres, S. Blanch, A. Aguasca, and R. Sabia, "From the Determination of Sea Emissivity to the Retrieval of Salinity: Recent Contributions to the SMOS Mission from the UPC and ICM," presented at IGARSS, Denver, Colorado, 2006.
[36] K. Rautiainen, J. Kainulainen, T. Auer, S. Tauriainen, and M. Hallikainen, "Helsinki University of Technology Synthetic Aperture Radiometer -HUT-2D," presented at IGARSS, Barcelona, Spain, 2007.
[37] M. Martin-Neira, I. Cabeza, C. Perez, M. A. Palacios, M. A. Guijarro, S. Ribo, I. Corbella, S. Blanch, F. Torres, N. Duffo, V. Gonzalez, S. Beraza, A. Camps, M. Vall-llossera, S. Tauriainen, J. Pihlflyckt, J. P. Gonzalez, and F. Martin-Porqueras, "AMIRAS: An Airborne MIRAS Demonstrator," *Geoscience and Remote Sensing, IEEE Transactions on*, vol. 46, pp. 705, 2008.
[38] AOES Medialab, "ESA's water mission SMOS," SMOS_ZoomOut.mpg, Ed., 2008.
[39] B. Lambrigtsen, W. Wilson, A. Tanner, T. Gaier, C. Ruf, and J. Piepmeier, "GeoSTAR - a microwave sounder for geostationary satellites," presented at IGARSS, Anchorage, Alaska, 2004.
[40] A. B. Tanner, B. H. Lambrigtsen, and T. C. Gaier, "A dual-gain antenna option for GeoSTAR," presented at IGARSS, Barcelona, Spain, 2007.
[41] A. B. Tanner, W. J. Wilson, B. H. Lambrigtsen, S. J. Dinardo, S. T. Brown, P. P. Kangaslahti, T. C. Gaier, C. S. Ruf, S. M. Gross, B. H. Lim, S. Musko, S. Rogacki, and J. R. Piepmeier, "Initial Results of the Geostationary Synthetic Thinned Array Radiometer (GeoSTAR) Demonstrator Instrument," *Geoscience and Remote Sensing, IEEE Transactions on*, vol. 45, pp. 1947, 2007.
[42] A. Camps, A. Camps, M. Vall-llossera, I. Corbella, N. A. D. N. Duffo, and F. A. T. F. Torres, "Improved Image Reconstruction Algorithms for Aperture Synthesis Radiometers," *Geoscience and Remote Sensing, IEEE Transactions on*, vol. 46, pp. 146, 2008.
[43] A. Camps, J. Bara, I. C. Sanahuja, and F. Torres, "The processing of hexagonally sampled signals with standard rectangular techniques: application to 2-D large

aperture synthesis interferometric radiometers," *Geoscience and Remote Sensing, IEEE Transactions on*, vol. 35, pp. 183, 1997.
[44] R. N. Bracewell and J. A. Roberts, "Aerial Smoothing in Radio Astronomy," *Australian Journal of Physics*, vol. 7, pp. 615, 1954.
[45] A. Moffet, "Minimum-redundancy linear arrays," *Antennas and Propagation, IEEE Transactions on [legacy, pre - 1988]*, vol. 16, pp. 172, 1968.
[46] J. Leech, "On the Representation of 1, 2., n by Differences," *J. London Math. Soc.*, vol. s1-31, pp. 160-169, 1956.
[47] E. Sharp, "A triangular arrangement of planar-array elements that reduces the number needed," *Antennas and Propagation, IEEE Transactions on [legacy, pre - 1988]*, vol. 9, pp. 126, 1961.
[48] R. M. Mersereau, "The processing of hexagonally sampled two-dimensional signals," *Proceedings of the IEEE*, vol. 67, pp. 930, 1979.
[49] J. Bara, A. Camps, F. Torres, and I. Corbella, "Angular resolution of two-dimensional, hexagonally sampled interferometric radiometers," *Radio Science*, vol. 33, pp. 1459, 1998.
[50] Y. H. Kerr, P. Waldteufel, J. P. Wigneron, and J. Font, "The Soil Moisture and Ocean Salinity mission: the science objectives of an L band 2-D interferometer," presented at IGARSS, Honolulu, Hawaii, 2000.
[51] H. Nyquist, "Certain topics in telegraph transmission theory," *Transactions of the AIEE*, pp. 617-644, 1928.
[52] C. E. Shannon, "Communication in the Presence of Noise," *Proceedings of the IRE*, vol. 37, pp. 10, 1949.
[53] U. R. Kraft, "Pattern characteristics and beamforming for synthetic aperture interferometric radiometer antennas," 1991.
[54] I. Corbella, F. Torres, A. Camps, A. Colliander, M. Martin-Neira, S. Ribo, K. Rautiainen, N. Duffo, and M. Vall-llossera, "MIRAS end-to-end calibration: application to SMOS L1 processor," *Geoscience and Remote Sensing, IEEE Transactions on*, vol. 43, pp. 1126, 2005.
[55] M. Tiuri, "Radio-Telescope Receivers," in *Radio Astronomy*. Powell, Ohio: Cygnus-Quasar Books, 1986, pp. 236-293.
[56] J. Robel, "NOAA KLM USER'S GUIDE," NOAA Satellite and Information Service, 2006.
[57] E. J. Miller, M. Madden, R. Reining, J. A. L. J. Linn, and L. A. O. C. L. O'Connor, "NOAA's GOES R - next generation satellite," presented at OCEANS 2003. Proceedings, 2003.
[58] A. B. Tanner, T. C. Gaier, and B. H. Lambrigtsen, "GeoSTAR Performance Demonstration," presented at Aerospace Conference, 2008 IEEE, 2008.
[59] A. B. Tanner, S. T. Brown, S. J. Dinardo, T. M. Gaier, P. P. Kangaslahti, B. H. Lambrigtsen, W. J. Wilson, J. R. Piepmeier, C. S. Ruf, S. M. Gross, B. H. Lim, S. Musko, and S. Rogacki, "Initial results of the GeoSTAR prototype (Geosynchronous Synthetic Thinned Array Radiometer)," presented at Aerospace Conference, 2006.
[60] A. Tanner, "Antenna range test results," Jet Propulsion Laboratory, Internal Memo 2003.

[61] P. Kangaslahti, A. Tanner, W. Wilson, S. Dinardo, and B. Lambrigsten, "Prototype development of a geo stationary synthetic thinned aperture radiometer (GeoSTAR)," presented at Microwave Symposium Digest, 2005 IEEE MTT-S International, 2005.
[62] I. Corbella, F. Torres, S. Blanch, S. Ribo, S. Beraza, N. Duffo, A. Camps, M. Vall-llossera, and M. Martin-Neira, "Inter-Element Phase Calibration in Interferometric Radiometers," presented at International Geoscience and Remote Sensing Symposium, 2006.
[63] M. A. Goodberlet, "Improved image reconstruction techniques for synthetic aperture radiometers," *Geoscience and Remote Sensing, IEEE Transactions on*, vol. 38, pp. 1362, 2000.
[64] A. Tanner, "GeoSTAR Antenna Alignment," Jet Propulsion Laboratory 01/19 2007.
[65] A. B. Tanner, S. T. Brown, T. C. Gaier, B. H. Lambrigsten, B. H. Lim, C. S. Ruf, and F. Torres, "Field tests of the GeoSTAR demonstrator instrument," presented at IGARSS, Barcelona, Spain, 2007.
[66] A. Tanner, B. Lambrigtsen, T. Gaier, and F. Torres, "Near Field Characterization of the GeoSTAR Demonstrator," presented at International Geoscience and Remote Sensing Symposium, 2006.
[67] F. Torres, "GeoSTAR near-field imaging test set-up," Jet Propulsion Laboratory 2005.
[68] N. Duffo, I. Corbella, F. Torres, A. Camps, and M. Vall-llosera, "Advantages and drawbacks of near-field characterization of large aperture radiometers," presented at Microrad, Rome, Italy, 2004.
[69] J. W. Gibbs, "Fourier Series," *Nature*, vol. 200, 1898.
[70] J. W. Gibbs, "Fourier Series," *Nature*, vol. 606, 1899.
[71] A. Camps, "Extension of the Clean Technique To the Microwave Imaging of Continuous Thermal Sources By Means of Aperture Synthesis Radiometers-Abstract," *Journal of electromagnetic waves and applications*, vol. 12, pp. 311, 1998.
[72] F. Torres, A. B. Tanner, S. T. Brown, and B. H. Lambrigsten, "Analysis of Array Distortion in a Microwave Interferometric Radiometer: Application to the GeoSTAR Project," *Geoscience and Remote Sensing, IEEE Transactions on*, vol. 45, pp. 1958, 2007.
[73] M. A. Janssen, *Atmospheric Remote Sensing by Microwave Radiometry*. New York: Wiley, 1993.
[74] B. Lin and P. Minnis, "Temporal Variations of Land Surface Microwave Emissivities over the Atmospheric Radiation Measurement Program Southern Great Plains Site," *Journal of Applied Meteorology*, vol. 39, pp. 1103-1116, 2000.
[75] F. Karbou, C. Prigent, L. Eymard, and J. R. Pardo, "Microwave land emissivity calculations using AMSU measurements," *Geoscience and Remote Sensing, IEEE Transactions on*, vol. 43, pp. 948, 2005.
[76] F. Karbou, L. Eymard, C. Prigent, and J. R. Pardo, "Microwave land surface emissivity assessment using AMSU-B and AMSU-A measurements," presented at IGARSS, Toulouse, France, 2003.

[77] F. Karbou, É. Gérard, and F. Rabier, "Microwave land emissivity and skin temperature for AMSU-A and -B assimilation over land," *Quarterly Journal of the Royal Meteorological Society*, vol. 132, pp. 2333-2355, 2006.
[78] J. I. Antonov, R. A. Locarnini, T. P. Boyer, A. V. Mishonov, and H. E. Garcia, "World Ocean Atlas 2005," in *World Ocean Atlas 2005*, vol. 2: Salinity, S. Levitus, Ed.: U.S. Government Printing Office, Washington, D.C., 2006, pp. 182 pp.
[79] P. Minnis, L. Nguyen, D. R. Doelling, D. F. Young, W. F. Miller, and D. P. Kratz, "Rapid Calibration of Operational and Research Meteorological Satellite Imagers. Part I: Evaluation of Research Satellite Visible Channels as References," *Journal of Atmospheric and Oceanic Technology*, vol. 19, pp. 1233-1249, 2002.
[80] P. Rabindra, P. Minnis, D. A. Spangenberg, M. M. Khaiyer, M. L. Nordeen, J. K. Ayers, L. Nguyen, Y. Yi, P. K. Chan, Q. Z. Trepte, F. L. Chang, and W. L. Smith, Jr., "NASA-Langley web-based operational real-time cloud retrieval products from geostationary satellites," presented at Remote Sensing of the Atmosphere and Clouds, SPIE, 2006.
[81] "Land/Sea/Lake Definition," GODAE High Resolution Sea Surface Temperature Pilot Project, 2002.
[82] N. O. A. A. U.S. Department of Commerce, National Geophysical Data Center, "2-minute Gridded Global Relief Data (ETOPO2v2)," 2006.
[83] L. Klein and C. Swift, "An improved model for the dielectric constant of sea water at microwave frequencies," *Antennas and Propagation, IEEE Transactions on [legacy, pre - 1988]*, vol. 25, pp. 104, 1977.
[84] P. Rosenkranz, "Water vapor microwave continuum absorption: A comparison of measurements and models," *Radio Sci.*, vol. 33, pp. 919-928, 1998.
[85] D. Staelin, "Measurements and Interpretation of the Microwave Spectrum of the Terrestrial Atmosphere near 1-Centimeter Wavelength," *J. Geophys. Res.*, vol. 71, pp. 2875-2881, 1966.
[86] E. M. Feæigel§son, *Light and heat radiation in stratus clouds: (Radiatsionnye protsessy v sloistoobraznykh oblakakh*. Jerusalem: Israel Program for Scientific Translations; [available from the U.S. Dept. of Commerce, Clearinghouse for Federal Scientific, and Technical Information, Springfield, Va.], 1966.
[87] J. P. Snyder, *Map Projections: A Working Manual*. Washington, D.C.: United States Government Printing Office, 1987.
[88] J. C. Ehrhardt, "Hexagonal fast Fourier transform with rectangular output," *Signal Processing, IEEE Transactions on*, vol. 41, pp. 1469, 1993.
[89] J. A. Högbom, "Aperture Synthesis with a Non-Regular Distribution of Interferometer Baselines," *Astronomy and Astrophysics Supplement*, vol. 15, pp. 417, 1974.
[90] W. H. Peake, "Radar return and radiometer emission from the sea," NASA Langley Research Center, Hampton, VA, NASA grant NGR-36-008-169 Tech. Rep. 3266-1, 1972.
[91] F. Beck, "Antenna pattern corrections to microwave radiometer temperature calculations," *Radio Sci.*, vol. 10, pp. 839-845, 1975.
[92] M. A. Janssen, C. S. Ruf, and S. J. Keihm, "TOPEX/Poseidon Microwave Radiometer (TMR). II. Antenna pattern correction and brightness temperature

algorithm," *Geoscience and Remote Sensing, IEEE Transactions on*, vol. 33, pp. 138, 1995.

[93] S. Brown, C. Ruf, S. Keihm, and A. Kitiyakara, "Jason Microwave Radiometer Performance and On-Orbit Calibration," *Marine Geodesy*, vol. 27, pp. 199, 2004.

[94] E. Obligis, L. Eymard, and N. Tran, "A New Sidelobe Correction Algorithm for Microwave Radiometers: Application to the Envisat Instrument," *Geoscience and Remote Sensing, IEEE Transactions on*, vol. 45, pp. 602, 2007.